Mathematical and Experimental Investigation of Multi-component Gas/Oil Displacements with Constant Pressure Boundaries

by

© *Hashem Nekouie*

A thesis submitted to the

School of Graduate Studies

in partial fulfilment of the

requirements for the degree of

Doctor of Philosophy

Department of *Process Engineering*

Memorial University of Newfoundland

May 2019

St. John's Newfoundland

Abstract

In this research, for the first time, multi-component gas/oil displacements with constant pressure boundaries are investigated mathematically and experimentally. Mathematically, the minimum miscibility pressure (MMP) is first calculated through an analytical method. Then, a novel extension of the classic Buckley-Leverett theory is applied to solve gas/oil displacement problems under constant pressure boundaries in a one-dimensional, dispersion-free medium. The developed analytical technique is applied to four and five-component systems, where the four-component system is a hypothetical case and the five-component system is a realistic and practical case. Experimentally, the five-component, $N_2/CO_2/C_6/C_{10}/C_{16}$, gas/oil displacement tests are designed and conducted in a slim tube set up. The MMP is first determined through common constant flux slim tube tests. Then, the analytical solution of systems with constant pressure boundaries is confirmed through corresponding slim tube experiments. However, unlike gas/oil displacements with constant flux boundaries in which the total flux is fixed both in space and time, the total flux varies with time in problems with constant pressure boundaries. Using the analytical technique, the breakthrough time of different waves are determined and the total flux is obtained as a function of time. The results indicate that the analytical solution matches with the experimental results if an appropriate relative permeability model is selected for the gas/oil flow in the slim tube. Finally, a new interpretation method, based on the constant pressure boundary experiments, is applied to obtain the gas/oil relative permeability curves. These independently obtained relative permeabilities are then employed in the analytical simulation and acceptable solutions are achieved.

Acknowledgements

I would like to thank my great supervisors, Dr. Lesley James and Dr. Thormod Johansen, whom without their help and guidance it was not possible for me to complete this research. I had a great and joyful time in all the chats and the discussions we had together as in all of them there was a great idea of yours and a solution for one of my problems. I owe this research all to you.

I also thank Edison Sripal, Shervin Ayazi, and Kim Power for all their help and support in my experimental work, those who prepared everything I needed in the lab and helped me to complete this journey.

My special thanks and love goes to my family who supported me in my every step in the life and were there for me in all the times. Thank you for being there.

Contents

List of Tables

List of Figures

Nomenclature

$\mathbb{R}^n$	Real numbers
α_{inj}	Constant value equal to 18.9 psia/K
β	Constant value equal to 0.285
μ_g	Viscosity of gas phase in cp
μ_o	Viscosity of oil phase in cp
ϕ	Porosity
ψ	Self-similar solution
ρ_{ci}	Molar density of component i
ρ_g	Molar density of vapor phase
ρ_{jD}	Dimensionless density
ρ_j	Molar density of injection fluid in $gmole/m^3$
ρ_j	Molar density of phase j in $gmole/m^3$
ρ_L	Molar density of fluid at the left side of the membrane in $gmole/m^3$

ρ_l Molar density of liquid phase

ρ_R Molar density of fluid at the right side of the membrane in $gmole/m^3$

τ Dimensionless time

ξ Dimensionless distance

A Cross sectional area in m^2

c_{ig} Volume fraction of component i in the vapor phase

c_{il} Volume fraction of component i in the liquid phase

C_i Overall volume fraction of component i

C_i^{init} Initial overall volume fraction of component i in porous media

C_i^{inj} Overall volume fraction of component i at the injection point

f Fractional flow of the vapor phase

$F(U)$ Flux of conserved quantity U

f_j Fractional flow of phase j

f_w Fractional flow of water

G_i Overall molar concentration of component i

G_i The number of angels per unit area

G_i^{init} Initial overall molar concentration of component i in the porous media

G_i^{inj} Overall molar concentration of component i at the injection point

H_i Overall molar flux of component i

I Identity matrix

I_o Oil characterization index

K Absolute permeability in Darcy

K_{rg} Relative permeability of gas phase

K_{ro} Relative permeability of oil phase

L Length of the porous media in m

M Viscosity ratio

M_{inj} Molecular weight of the injection gas

n Number of cells in multiple mixing cell simulation

n_c Number of components in the system

N_M Number average molecular weight of the oil

P Pressure in psia

$P_{c,inj}$ Injection gas critical pressure in psia

$P_{MMP,impure}$ Minimum miscibility pressure of impure CO_2 stream in psia

$P_{MMP,impure}$ Minimum miscibility pressure of pure CO_2 injection in psia

P_{MMP} CO_2 minimum miscibility pressure in psia

q_{Gas} Gas flow rate

q_{Oil} Oil flow rate

q_{Total} Total flow rate

S Vapor phase saturation

S_{gc} Critical gas saturation

S_j Saturation of phase j

S_{or} Residual oil saturation

S_w Water saturation fraction

t Time in seconds

$T_{c,g}$ Injection gas critical temprature in K

$T_{c,inj}$ Injection gas critical temprature in K

T_{res} Reservoir temprature in K

U Conserved quantity

u_D Dimensionless flow velocity

u_{inj} Total velocity at the injection point in m/s

U_L Conserved quantity in the left side of membrane

U_R Conserved quantity in the right side of membrane

u_T Total velocity in m/s

x Distance in the flow direction in m

x_{ij} Mole fraction of component i in phase j

x_i Volume fraction of component i in the liquid phase

y_i Volume fraction of component i in the vapor phase

Chapter 1

Introduction

1.1 Minimum Miscibility Pressure

Minimum Miscibility Pressure (MMP) is important in the oil and gas industry because it is the pressure at which gas and oil are miscible and oil recovery can be substantially enhanced. Miscibility helps increase incremental oil recovery by theoretically reducing interfacial tension to zero, reducing the capillary pressure to zero, and enabling the possibility of recovering oil from all pores. Numerous definitions are presented for the MMP. Theoretically speaking, the MMP is the lowest pressure at which on of the key tie-lines becomes the critical tie-line, i.e. it has zero length [45]. At this pressure, a miscible zone is created between the injection gas and the initial oil, and the interfacial tension in this region, where the composition path approaches the critical tie-line when miscibility develops, goes to zero. However, practically speaking, the MMP is the lowest pressure at which oil recovery does not increase substantially by increasing pressure further, i.e. Figure 1.1.

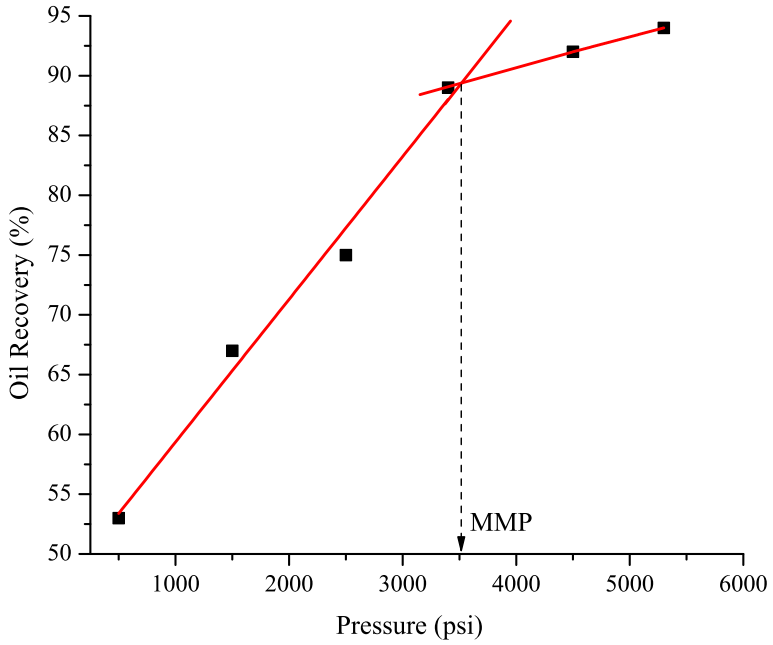

Figure 1.1: Typical recovery vs. pressure plot for determination of the MMP

Numerous experimental and mathematical methods are suggested in the literature to determine the MMP. The industry best practice is to determine the MMP through slim tube experiments. Figure 1.1 shows the results from a typical slim tube test where the recovery is plotted against pressure for a series of experiments. A recovery factor of 90% is normally chosen as the miscibility criteria. Miscibility is a thermodynamic process governed by the pressure, temperature and composition of the hydrocarbon phases creating one single phase. In gas injection, miscibility occurs in a transition zone developed between the injection gas and the initial oil, i.e. Figure 1.2.

This single phase transition zone (without interface), which is a result of complicated interactions between the injection gas and initial oil, creates a piston like displacement and enables all components to be produced in the production well. As a consequence of phases' interactions, a chromatographic separation of components occurs, as the

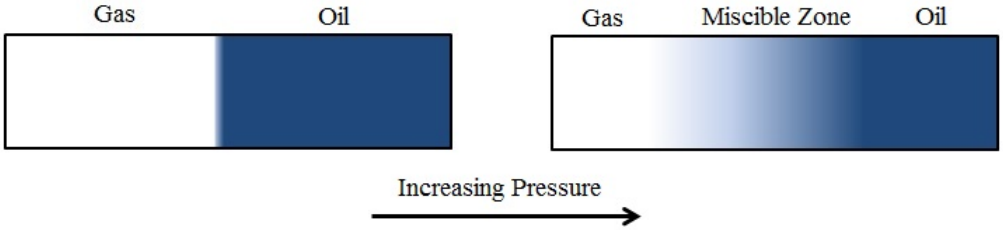

Figure 1.2: Development of miscibility by increasing the pressure

components partition between the oil and gas phases to establish a chemical equilibrium. A schematic view of this chromatographic separation is shown in Figure 1.3.

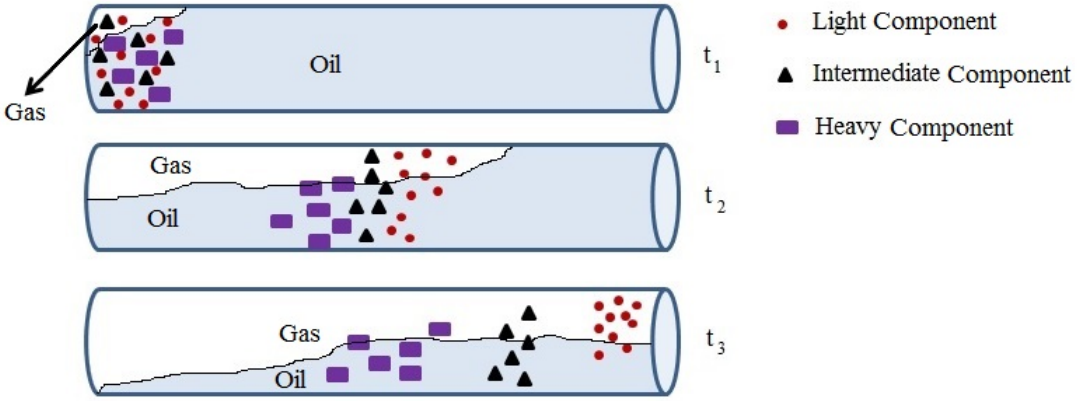

Figure 1.3: Chromatographic separation of components in gas/oil displacements

Different components are then transported by the two phases with different velocities. The lighter components, shown by circles in Figure 1.3, with higher volatility have more preference to show up in the vapor phase and move faster than the heavy components, shown by rectangles in Figure 1.3, with more preference to the liquid phase. These velocities are functions of imposed pressure, phase saturations, the physical properties of the phases and their interactions with the rock. However,

the components are transferred in the two phases by convection, and diffusion to establish a thermodynamic equilibrium. At high enough pressures, after multiple contacts between the initial oil and the injection gas, the single phase miscible zone, is created between the two phases and the sharp interface between the gas and the oil disappears, i.e. Figure 1.2. However, completion of this phenomenon requires enough time to establish thermodynamic equilibrium and several contacts to develop miscible gas and oil phases in the medium. Therefore, a long porous medium and low gas injection rate are necessary parameters to achieve miscibility in gas injection scenarios. Yet, the exact length and injection rate depend on the oil and gas compositions as well as temperature and porous media properties such as porosity and permeability. The complexity of the miscibility phenomenon mentioned above, makes understanding the transport mechanisms and thermodynamics of gas/oil displacements an inevitable part of any successful gas flooding design.

1.2 Gas/Oil Displacements

Although numerical approaches are often used to quantify multi-component gas injection problems, an analytical solution is preferred as results are more accurate and faster to obtain, if an analytical solution exist. Like other theoretical approaches to modeling transport phenomena, the analytical description of gas/oil displacements starts with the fundamental conservation laws for the individual components present in the system.

$$\Delta \dot{C}_i = \dot{C}_{i,convection} + \dot{C}_{i,dispersion} \tag{1.1}$$

where $\Delta\dot{C}_i$ is the rate of change of amount of component i in an arbitrary volume $V(t)$, $\dot{C}_{i,convection}$ is the net rate of inflow of component i into $V(t)$ due to the convection, and $\dot{C}_{i,dispersion}$ is the net rate of inflow of component i into $V(t)$ due to the dispersion. Writing Equation 1.1 for all components present in the system leads to a set of Partial Differential Equations (PDEs), which along with initial and boundary conditions constitute an initial value problem. The solutions of such systems, known as Riemann problems, have been studied in detail for two- and three-phase displacements. Buckley and Leverett [4] derived the analytical solution for a water/oil displacement with constant flux boundary systems for the first time. They used the fractional flow theory to obtain the water saturation profile in a one-dimensional dispersion-free porous medium. Buckley Leverett equation and its solution are given by Equation 1.2 and Figure 1.4, respectively.

$$\frac{\partial S_w}{\partial t} + \frac{u_T}{\phi}\frac{\partial f_w(S_w)}{\partial x} = 0 \tag{1.2}$$

In Equation 1.2, S_w is the water saturation, t is the time, ϕ is the porosity, x is the distance from the inlet, f_w is the fractional flow of water and u_T is the total velocity where $u_T = constant$. A detailed mathematical description of Riemann problems, including the Buckley Leverett equation, is presented in Chapter 2.

Different types of problems such as water flooding, polymer flooding, alcohol injection, surfactant injection, foam injection and gas injection are very well understood in two-phase systems. All of these systems assume a constant volumetric flux inside the porous medium. However, in practice, it is difficult to keep the total flux constant and there will always be some fluctuation in the flow rate. Indeed, flow rate is never

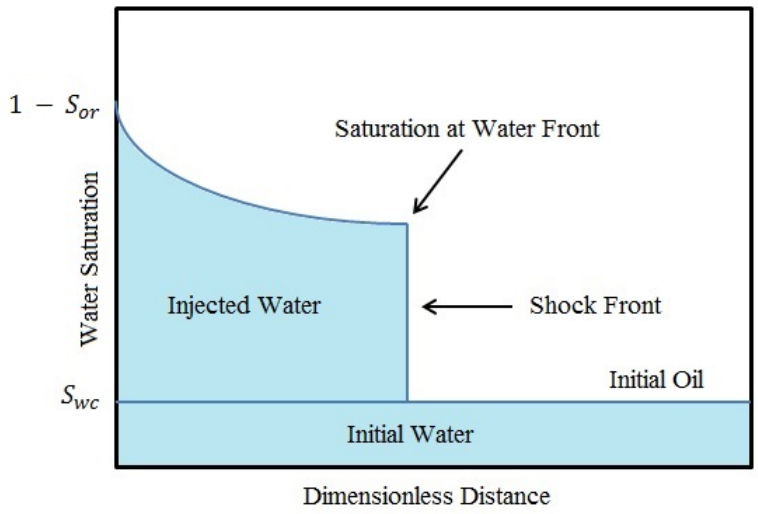

Figure 1.4: Water saturation distribution as a function of distance in Buckley-Leverett solution

constant if the wells are operated at a constant bottom hole pressure when gas is injected. Sometimes, it is more practical to perform injection projects using constant injection and production pressures. Johansen and James [32] extended the Buckley-Leverett classic fractional flow theory to problems with constant pressure boundaries. They found that unlike problems with constant flux boundaries, where the total flux is constant both in time and space, the total flux is a function of time in the systems with constant pressure boundaries. In their work, it is shown that the procedure works very well for water and polymer injection systems and the results are compared with numerical simulations. In this research, their technique is applied to multi-component systems and the results are also compared with experimental results. In this work, slim tube experiments are conducted to verify that these solutions are capable of capturing the main mechanisms occuring in real displacements, and therefore, that the real process is well understood. In the other words, we examine the truth of the assumptions made in the mathematical developments.

1.3 Novelty, Motivation, and Objectives

To date, the study of two and three-phase systems and developing miscibility is virtually completed. Yet, the boundary condition by which governing equations are solved is a restricting aspect. All the documented research in the literature has been conducted under the main assumption of the constant flux boundary condition. Realistically, it is difficult to keep the flow rate constant and there will be fluctuations in the flow rate. Sometimes, it is more practical to perform gas flooding or chemical EOR at constant injection and constant production pressures. Johansen and James [32] found the solution for Riemann problems with constant pressure boundary conditions. In this work, their technique is applied for multi-component gas injection problems. Developed analytical solutions are fast and can predict the breakthrough time and the total velocity accurately. These fast and accurate analytical solutions are confirmed with experimental results for the first time, and can also be coupled with streamlines and stream tubes to simulate two and three-dimensional reservoirs, where it can be used to determine the optimal well locations. Using the constant pressure boundary solution, for the first time, the effect of increasing average pressure on phase behavior of displacing and displaced fluids is investigated both analytically and experimentally in this research. The analytical technique to calculate the MMP developed by Jessen et al. [26] is also analyzed in this work due to importance of this parameter in gas flooding projects. MMP is analytically determined for a synthetic oil and is compared with slim tube results. Finally, a new interpretation method is introduced to obtain the relative permeability curves from unsteady-state experiments.

1.4 Thesis Structure

In Chapter 2, a review of two- and three-phase displacements is first presented. It describes how the analytical methods for solving displacement problems have been improved over the years by the hard work of many mathematicians and engineers. Then, different methods to estimate MMP are reviewed. The main experimental techniques as well as mathematical techniques are covered in this section.

Chapter 3 presents the general methodology of the research. In this chapter, the approach to mathematical modeling of gas/oil displacements is first illustrated. Then, it is stated how the solution of problems with constant flux boundaries can be used to obtain the solution of corresponding problems with constant pressure boundaries. Three case studies are presented to demonstrate the idea. In the last section of this chapter, the analytical method developed by Jessen et al. [26] to estimate MMP is applied for a synthetic oil.

In Chapter 4, the experimental methodology used to conduct slim tube experiments and calculate the MMP of the synthetic oil studied in Chapter 3 are described.

In Chapter 5, the results of slim tube experiments with constant pressure boundaries are demonstrated. In this chapter, the experimental results are compared to the analytical results obtained in Chapter 3. Also, a new interpretation method is presented to determine the gas/oil relative permeability data based on the unsteady-state constant pressure boundaries experiments.

Finally, a summary of the research, conclusions, and future work are provided in Chapter 6.

Chapter 2

Literature Review

Understanding transport phenomena in porous media and the logic behind the mathematical modelings are essential for any EOR process. An analytical solution to displacement problems is an effective tool to precisely investigate the physical transport mechanism occurring in the porous media, assuming analytical solutions exist. Analytical solutions have been developed by numerious mathematicians to examine flow in porous media over the past century. The development of analytical methods in EOR processes, gas injection projects in particular, is reviewed in this chapter.

2.1 Introduction to the Enhanced Oil Recovery, Phase Behaviour, Reservoir Engineering, and Mathematical Concepts

Before starting the literature review, basic terms of Enhanced Oil Recovery (EOR), phase behaviour, reservoir engineering, and a few mathematical concepts required to

understand this research are briefly reviewed in this section.

2.1.1 Enhanced Oil Recovery (EOR)

Oil production from a reservoir can be divided into three periods: primary recovery, secondary recovery, and tertiary recovery. During primary recovery, expansion of the oil and rock is the driving mechanism for oil production. Over time, the reservoir pressure drops due to the oil being produced. In order to maintain the pressure and keep production at a constant level, water or gas is injected in the reservoir during secondary recovery. Secondary recovery continues until the reservoir pressure can not be maintained, or the water or gas produced becomes too high to economically produce any further oil. Tertiary recovery or Enhanced Oil Recovery (EOR) commences at this point, if it is to be applied. The EOR process involves numerous methods such as miscible/immiscible gas injection, thermal methods, chemical flooding, and microbial methods.

2.1.2 Phase Behaviour of Oil Reservoirs

Hydrocarbon fluids in oil reservoirs are a complex mixture of many organic components, and some inorganic components. These fluids attain divergent properties and show different behaviour over a wide range of reservoir pressure and temperature. At reservoir conditions, where the pressure changes dramatically over the life of the producing field and the temperature is relatively constant, hydrocarbon fluids mainly exist in gas and liquid phases. Simulation of EOR scenarios requires precise modeling of the gas and liquid behaviour in order to predict incremental oil recovery. Equation

of State (EOS) modeling is used to capture the thermodynamic phase behaviour of the oil and gas. In this research, Peng-Robinson EOS has been employed for phase behaviour calculations.

2.1.2.1 Peng-Robinson EOS

Peng-Robinson EOS relates the pressure, volume, and temperature through the following equation [49].

$$P = \frac{RT}{\tilde{v} - b} - \frac{\alpha a}{\tilde{v}^2 + 2b\tilde{v} - b^2} \tag{2.1}$$

In Equation 2.1, P is the pressure, R is the gas constants, T, is the temperature, $\tilde{v}$ is the molar volume. α, a, and b are the correction terms for repulsion and attraction inter-molecular forces. α is a temperature dependent parameter to correct for the non-spherical molecular shape and interactions through the acentric factor, ω.

$$\alpha = \left[1 + (0.37464 + 1.54226\omega - 0.26992\omega^2)(1 - \sqrt{T_r})\right]^2 \tag{2.2}$$

In Equation 2.2, T_r is the reduced temperature defined as,

$$T_r = \frac{T}{T_c} \tag{2.3}$$

where T_c is the critical temperature. a and b are functions of critical properties and are given by below equations.

$$a = 0.45724 \frac{R^2 T_c^2}{P_c} \tag{2.4}$$

$$b = 0.07780 \frac{R T_c}{P_c} \tag{2.5}$$

In Equations 2.4 and 2.5, P_c is the critical pressure.

2.1.2.2 Equilibrium Ratio (K-value)

In a gas/liquid system in thermodynamic equilibrium, equilibrium ration (K-value) of component i, K_i, is defined as the mole fraction of component i in the gas phase, y_i, divided by its mole fraction in the liquid phase, x_i.

$$K_i = \frac{y_i}{x_i} \tag{2.6}$$

K-values depend on the pressure, temperature, and the overall composition of the system. Yet, the common sense is that $K_i \gg 1$ for light components such as CH_4, $K_i \ll 1$ for heavy components such as C_7, and it is close to 1 for intermediate components such as C_4. K-values can be estimated using an EOS.

2.1.2.3 Phase Diagrams

In many reservoir engineering problems, the phase behaviour of the system is represented by a collection of compositions in a phase diagram [45]. For three and four component systems, it is more convenient to show the composition points in a com-

positional space. Figures 2.1 and 2.2 show typical phase diagrams for three and four component systems, respectively.

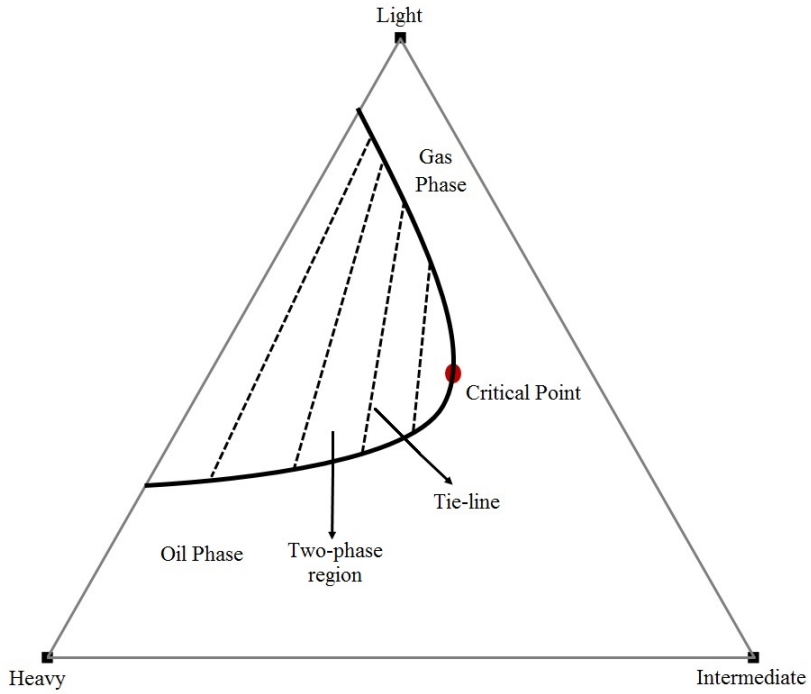

Figure 2.1: Schematic phase diagram for a three-component system

Since the sum of mole fractions at any composition point is always one, it is convenient to show the phase diagrams of three and four component systems in ternary and quaternary diagrams. Ternary and quaternary diagrams are plotted at fixed pressure and temperature. As shown in Figure 2.2, a quaternary phase diagram consists of four faces, each representing a ternary phase diagram of three components.

2.1.2.4 Tie-line

Tie-lines are mainly defined for the two-phase region, even though, they can be extended to the single phase regions. Tie-lines are imaginary lines in two-phase region,

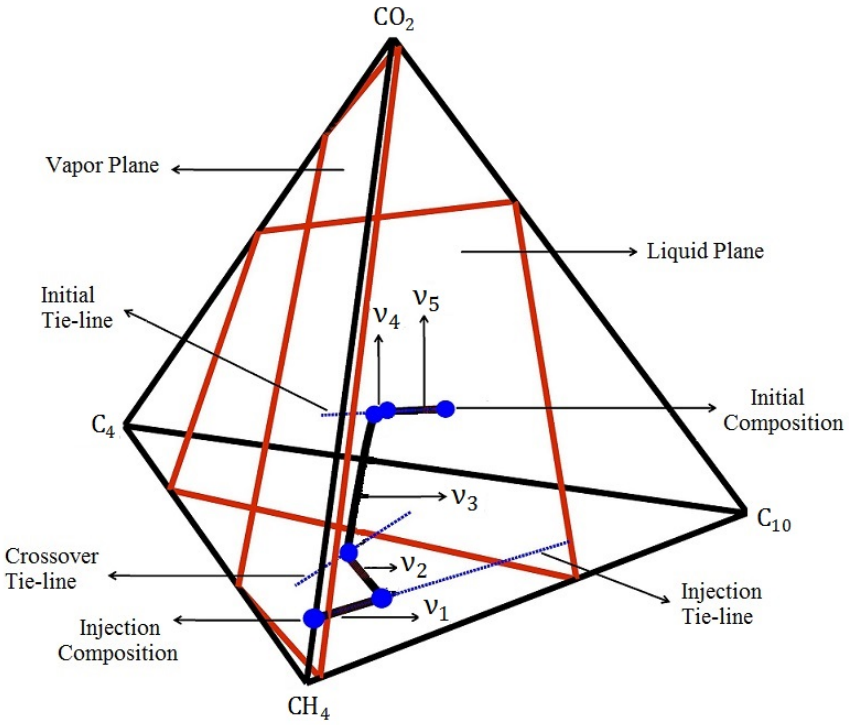

Figure 2.2: Schematic phase diagram for a four-component system

on which all overall compositions have the same equilibrium liquid and gas compositions. Dash lines in Figure 2.1 are some of tie-lines in a ternary diagram. The two-phase region in Figure 2.1 is filled with infinite number of tie-lines. However, only a few of them are shown here for the clarification. The geometry of tie-lines, whether they are converging in the gas phase or liquid phase, depends on the components present in the light, intermediate, and heavy groups. The analytical solution in gas/oil displacements depends on the geometry of tie-lines. This is discussed in more detail later in Section 2.3 and in Chapter 3.

2.1.3 Reservoir Engineering

Analytical and numerical simulation of gas/oil displacement problems requires the fundamental knowledge of fluid flow through porous media. In this section, reservoir engineering concepts applied in research, are briefly reviewed.

2.1.3.1 Darcy's Law

In any arbitrary flow direction, the flow rate of a single phase fluid can be calculated from Darcy's law [21],

$$Q = -\frac{KA}{\mu}(\frac{\partial p}{\partial s} + \rho g sin\theta) \tag{2.7}$$

where Q is the flow rate in $\frac{cm^3}{s}$, K is the absolute permeability in Darcy (D), A is the cross section area in cm^2, p is the pressure in atm, s is the positive flow direction in cm, ρ is the fluid density in $\frac{g}{cm^3}$, g is the acceleration of gravity, and θ is the angle between positive x-axis and positive flow direction.

2.1.3.2 Relative Permeability

Relative permeability is a concept used to extend the Darcy's law to represent the relative flow of each phase, if two or more phases are flowing simultaneously in porous media. The new form of the Darcy's law for multi-phase flow is

$$Q_j = -\frac{K_{rj}A}{\mu_j}(\frac{\partial p_j}{\partial s} + \rho_j g sin\theta) \tag{2.8}$$

where subscript j refers to the phase j in the system and K_{rj} is the relative permeability of phase j defined as

$$K_{rj} = \frac{K_j}{K} \tag{2.9}$$

In Equation 2.9 K_j is the effective permeability of phase j. Relative permeabilities are functions of phase saturations and can be calculated using steady state and unsteady state experiments. This is an experimental fact that effective phase permeabilities,K_j, can not exceed the absolute permeability, K. Therefore, $0 \leq K_{rj} \leq 1$. Corey-type relative permeability models are well known alternatives if experimental data are not available [8]. Corey-type relative permeabilies are defined by the following equations for gas/oil systems.

$$
\begin{aligned}
K_{rg}(S_g) &= a_g(\frac{S_g - S_{gc}}{1 - S_{gc} - S_{or}})^{n_g}, && S_{gc} \leq S \leq 1 - S_{or}, \\
K_{rg} &= 0, && S < S_{gc}, \\
K_{rg} &= 1, && S > 1 - S_{or}, \\
K_{ro}(S_g) &= a_o(\frac{1 - S_g - S_{or}}{1 - S_{gc} - S_{or}})^{n_o}, && S_{gc} \leq S \leq 1 - S_{or}, \\
K_{ro} &= 0, && 1 - S < S_{or}, \\
K_{ro} &= 1, && 1 - S > 1 - S_{gc}.
\end{aligned}
\tag{2.10}
$$

In Equation 2.10, a_g and a_o are constants that represent the end point values on the gas and oil relative permeability curves, respectively. They can take values between 0 and 1 are calculated from experiments. The constants n_g and n_o are called Corey indexes and can take values between 1 to 6. Corey indexes depend on the pore size distribution and can be calculated from experimental data [2]. In Equation 2.10, S_{gc} and S_{or} represent the critical gas saturation and residual oil saturation, respectively. A schematic of Corey-type relative permeabilities is shown in Figure 2.3.

Brooks-Corey [2], Corey-Rathjens [9], Chierici [6], and Alpak et al. [1] also proposed various relative permeability models for two-phase of fluids in porous media. In this research, the Corey-type relative permeability model is chosen as it has a simple form and it can be easily applied in the analytical simulation.

2.1.3.3 Fractional Flow

Fractional flow is an important concept when two or more phases are flowing simultaneously in the system. By definition, the fractional flow of phase j, f_j, is the flow rate of phase j divided by the total flow rate in the system.

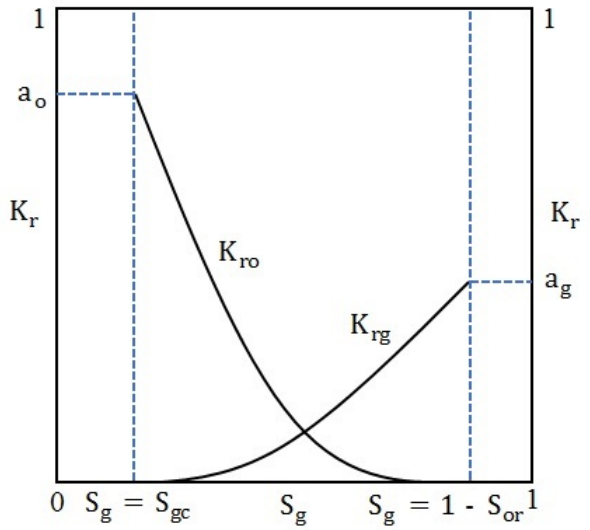

Figure 2.3: A typical Corey-type relative permeability for a two-phase gas/oil system

$$f_j = \frac{q_j}{q_{Total}} = \frac{q_j}{\sum_{i=1}^{j=n_p} q_i} \tag{2.11}$$

where f_j represents the fractional flow of phase j, q_j is the flow rate of phase j, and q_{Total} is the total flow rate in porous media. For a two-phase gas/oil displacement, Equation 2.11 reduces to

$$f_g = \frac{q_{Gas}}{q_{Total}} = \frac{q_{Gas}}{q_{Gas} + q_{Oil}} \tag{2.12}$$

In Equation 2.12, q_{Gas} , q_{Oil}, and q_{Total} are the gas, oil and the total flow rates, respectively. Both q_{Gas} and q_{Oil} are calculated through Darcy's law. Assuming that the displacement happens in a horizontal porous medium and the capillary forces are negligible,

$$q_{Gas} = -\frac{KK_{rg}A}{\mu_g}\frac{dP}{dx}, \qquad q_{Oil} = -\frac{KK_{ro}A}{\mu_o}\frac{dP}{dx} \tag{2.13}$$

hence,

$$f = \frac{q_{Gas}}{q_{Total}} = \frac{q_{Gas}}{q_{Gas} + q_{Oil}} = \frac{-\frac{KK_{rg}A}{\mu_g}\frac{dP}{dx}}{-\frac{KK_{rg}A}{\mu_g}\frac{dP}{dx} - \frac{KK_{ro}A}{\mu_o}\frac{dP}{dx}} = \frac{\frac{K_{rg}}{\mu_g}}{\frac{K_{rg}}{\mu_g} + \frac{K_{ro}}{\mu_o}} \tag{2.14}$$

Also, assuming that the relative permeabilities of the gas and oil phases are given by the Corey-type models with $a_g = 1$, $a_o = 1$, $n_g = 2$, and $n_o = 2$, substitution of corresponding terms in Equations 2.14 and using normalized gas saturation gives

$$\begin{aligned} f_g &= 0, && S < S_{gc}, \\ f_g &= \frac{S^2}{S^2 + \frac{(1-S)^2}{M}}, && S_{gc} \leq S \leq 1 - S_{or}, \\ f_g &= 1, && S > 1 - S_{or}, \end{aligned} \tag{2.15}$$

where,

$$M = \frac{\mu_o}{\mu_g}. \tag{2.16}$$

In Equation 2.16 M is the viscosity ratio, S is the normalized gas saturation, and μ_o and μ_g represent the oil and gas viscosities, respectively.

2.2 Mathematical Concepts

In this section general procedure for analytically solving gas/oil displacements is presented. Riemann problems are first defined. Mass conservation is then provided and then it is described how the Method of Characteristics (MOC) is used to solve Riemann problems generated in gas/oil displacements.

2.2.1 Riemann Problems

Conservation of mass in porous media leads to a set of partial differential equations. The number of equations depends on the number of components present in the system and the condition under which the displacement happens. These equations along with initial conditions constitute a Riemann problem. In mathematics, a Riemann problem is an initial value problem in an infinity long one-dimensional medium where the initial data are separated by a sharp discontinuity at $x = 0$. Mathematical formulation of a Riemann problem is:

$$\frac{\partial U}{\partial t} + \frac{\partial F(U)}{\partial x} = 0, \qquad U(x,t) = \begin{cases} U_L & x \leq 0 \\ \\ U_R & x > 0 \end{cases}, \qquad F \in \mathbb{R}^n, \qquad U \in \mathbb{R}^n \tag{2.17}$$

In Equation 2.17, $U = U(U_1, ..., U_n)$, where components U_i of vector U are called conserved quantities and $F(U) = (F_1(U), ..., F_n(U))$, where components $F_i(U)$ of vector $F(U)$ are called fluxes. This problem was named in honor of Bernhard Riemann who solved it for the first time [53]. In reality, this can be thought of as two fluids with different densities, separated by a membrane as displayed in Figure 2.4. By elimination of the membrane, the fluids will mix and the distribution of the fluids along the medium will be the solution of the corresponding Riemann problem. Figure 2.5 shows the schematic solution of the Riemann problem illustrated in Figure 2.4. As shown in Figure 2.5 removing the membrane, creates shock waves and rarefaction waves propagating in the medium. Shock waves are abrupt change or discontinuous variation of the conserved quantity and rarefaction waves are known with continuous and gradual change.

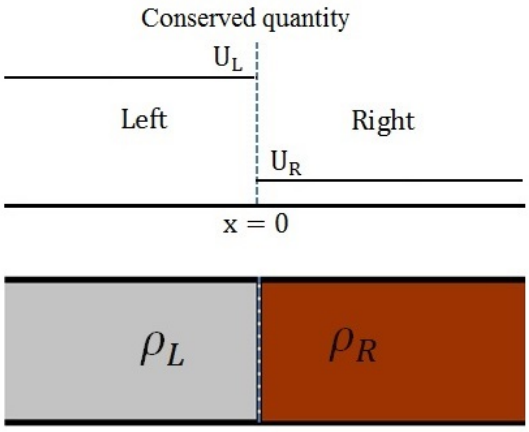

Figure 2.4: Schematic of a Riemann problem

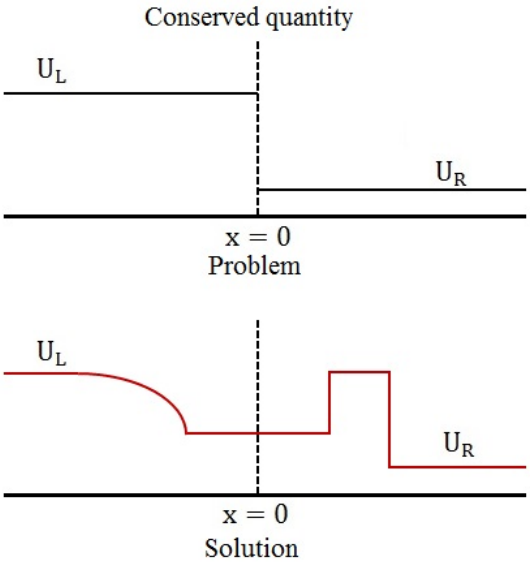

Figure 2.5: Solution of a Riemann problem

Now, suppose that an injection fluid is going to be injected into a one-dimensional reservoir initially saturated with oil. Assuming adequate injection fluid is available, this system can be compared with Figure 2.4, where the injection fluid and the initial oil are separated by a hypothetical membrane prior to the injection. Injection of displacing fluid into the reservoir corresponds to the elimination of membrane. By starting the injection, or removing the membrane, the injection fluid will displace the initial oil from the reservoir and a distribution of the fluids in the reservoir will be established. This is schematically shown in Figure 2.5. Though, in this case only the right side of the solution, $x \geqslant 0$, is considered. Hence, the saturation distribution of the fluids in the porous medium is the solution of the Riemann problem 2.17. In the following sections, it is demonstrated how the solution can be constructed when a multi-component gas is injected into a one-dimensional undersaturated reservoir.

2.2.2 Conservation of Mass

Fundamental conservation laws for a system containing n-components in a one-dimensional dispersion-free porous medium, where a gas with constant composition is being injected into the porous medium saturated with an initial oil, results in the following initial value problem:

$$
\begin{aligned}
&\frac{\partial}{\partial t}\phi \sum_{j=1}^{2} x_{ij}\rho_j S_j + \frac{\partial}{\partial x} u_T \sum_{j=1}^{2} x_{ij}\rho_j f_j = 0, \quad ; && && i = 1, ..., n_c \\
&C_i(x,t) = C_i^{inj} && ; \quad x = 0 \quad ; && i = 1, ..., n_c, \\
&C_i(x,0) = C_i^{init} && ; \quad x \geqslant 0 \quad ; && i = 1, ..., n_c.
\end{aligned}
\tag{2.18}
$$

where, t is the time, ϕ is the porosity, x_{ij} is the mole fraction of component i in the phase j, ρ_j is the molar density of the phase j, S_j is the saturation of the phase j, x is the distance from the inlet, u_T is the total velocity in the porous medium, f_j is the fractional flow of phase j, and n_c is the total number of components in the system. Furthermore, C_i represents the overall composition of component i as C_i^{inj} is the overall composition of the injection gas and C_i^{init} is the overall composition of the initial oil. By introducing the dimensionless variables $\tau = \dfrac{u_{inj}t}{\phi L}$ as the dimensionless time, $\xi = \dfrac{x}{L}$ as the dimensionless length, $u_D = \dfrac{u_T}{u_{inj}}$ as the dimensionless velocity, and $\rho_{jD} = \dfrac{\rho_j}{\rho_{inj}}$ as the dimensionless density, Equation 2.18 is simplified to

$$\begin{aligned}
&\frac{\partial}{\partial\tau}\phi\sum_{j=1}^{2}x_{ij}\rho_{jD}S_j + \frac{\partial}{\partial\xi}u_D\sum_{j=1}^{2}x_{ij}\rho_{jD}f_j = 0, \quad ; && && i = 1, ..., n_c \\
&C_i(\xi,\tau) = C_i^{inj} && ; \quad \xi = 0 \quad ; && i = 1, ..., n_c, \\
&C_i(\xi,0) = C_i^{init} && ; \quad \xi \geqslant 0 \quad ; && i = 1, ..., n_c.
\end{aligned} \tag{2.19}$$

Equation 2.19 can be further simplified to

$$\begin{aligned}
&\frac{\partial G_i}{\partial\tau} + \frac{\partial H_i}{\partial\xi} = 0 \quad ; && && i = 1, ..., n_c, \\
&G_i(\xi,\tau) = G_i^{inj} \quad ; && \xi = 0 \quad ; && i = 1, ..., n_c, \\
&G_i(\xi,0) = G_i^{init} \quad ; && \xi \geqslant 0 \quad ; && i = 1, ..., n_c.
\end{aligned} \tag{2.20}$$

by using the notation $G_i = \sum_{j=1}^{2} x_{ij}\rho_{jD}S_j$ and $H_i = u_D\sum_{j=1}^{2} x_{ij}\rho_{jD}f_j$, where G_i and H_i are the overall concentration and the overall molar flow of component i, respectively. Furthermore, τ is the dimensionless time and is calculated in terms of the

number of pore volumes of gas injected into the porous medium, ξ is the dimensionless length and is calculated as a fraction of the medium length, i.e. $\xi \in [0,1]$, and finally, the injection state represents the left state. Model 2.20 is a system of partial differential equations with n_c equations and n_c unknowns. $G_1, ..., G_{n_c-1}$ and u_D are the unknowns to be determined. The model in Equation 2.20 can be further simplified if we assume that components do not change volume as they transfer between the phases. This is a reasonable assumption when the average displacement pressure is high [25]. An important result of no volume change upon mixing is that the total flux is constant along the media, i. e. $u_T = u_{inj}$ and hence $u_D = 1$. Now, model 2.20 becomes

$$\begin{aligned}
&\frac{\partial C_i}{\partial \tau} + \frac{\partial F_i}{\partial \xi} = 0 \quad ; && && i = 1, ..., n_c - 1, \\
&C_i(\xi, \tau) = C_i^{inj} \quad ; && \xi = 0 \quad ; && i = 1, ..., n_c, \\
&C_i(\xi, 0) = C_i^{init} \quad ; && \xi \geqslant 0 \quad ; && i = 1, ..., n_c.
\end{aligned} \tag{2.21}$$

In set of Equations 2.21, C_i and F_i are the overall volume fraction and the overall fractional volumetric flow of component i, respectively. C_i and F_i are calculated from

$$C_i = c_{ig} S + c_{il}(1 - S), \qquad F_i = c_{ig} f + c_{il}(1 - f), \qquad i = 1, ..., n_c \tag{2.22}$$

where c_{ig} and c_{il} are the volume fraction of component i in the vapor and liquid phases, respectively. The normalized vapor phase saturation is denoted S and f is the fractional flow of the vapor phase. Parameters c_{ig} and c_{il} are related to the mole

fraction of individual components by

$$c_{ig}\rho_{ci} = \rho_g y_i, \qquad c_{il}\rho_{ci} = \rho_l x_i, \qquad i = 1, ..., n_c \tag{2.23}$$

where ρ_{ci} is the molar density of component i and is constant for systems with no volume change upon mixing.

Examining Equation 2.22 indicates that $C_i = C_i(S)$ and also $F_i = F_i(S)$, therefore, $F_i = F_i(C_1, ..., C_{n_c-1})$. Thus, Equation 2.21 is a Riemann problem where, the overall volume of components, C_i, are the conserved quantities and overall fractional volumetric flow of components, F_i, are the fluxes. Furthermore, it is observed that in Equation 2.21 the number of equations is reduced by one, because $\sum_{i=1}^{n_c} C_i = 1$.

However, certain assumptions are made in the derivation of the model in Equation 2.21. The assumptions include that: (1) the flow is one-dimensional, (2) the effects of dispersion and diffusion are negligible, (3) in particular capillary forces and mechanical dispersion are zero, (4) there is no volume change upon mixing, (5) fluids are incompressible; and (6) phases present at any location are in instantaneous chemical equilibrium. To solve the initial value problem 2.21 it is converted to an eigenvalue problem and is solved using Method of Characteristics (MOC), as described by Orr [45]. The MOC is described in detail in the next section. However, the resulting eigenvalue problem leads to a number of eigenvalues and eigenvectors where the number of eigenvalues depend on the number of components present in the system. The eigenvalues are the wave velocities that overall compositions propagate with and the associated right eigenvectors are the directions in the compositional space along which composition variations satisfy the mass conservation equation. Using the eigenvalues

and the eigenvectors, the solution is constructed in compositional space.

2.2.3 Method of Characteristics (MOC)

The solution construction for Equation 2.21 is based on the Method of Characteristics (MOC). In this method, parameter γ is defined such that along γ the partial differential equations (PDEs) become Ordinary Differential Equations (ODEs). The procedure is briefly reviewed here for a two-component system [57, 15]. Since the overall volumetric flux, F, is a function of overall volume fraction, C, Equation 2.21 can be reformulated as,

$$\frac{\partial C_1}{\partial \tau} + \frac{dF_1}{dC_1}\frac{\partial C_1}{\partial \xi} = 0 \tag{2.24}$$

Assuming that $C(\tau, \xi)$ is a solution of 2.24 and the graph of this function is given by surface Γ

$$\Gamma \equiv \{(\tau, \xi, C(\tau, \xi))\} \tag{2.25}$$

If $C(\tau, \xi)$ is a solution of Equation 2.24, then at any point

$$(1, \frac{dF_1}{dC_1}, 0).(\frac{\partial C_1}{\partial \tau}, \frac{\partial C_1}{\partial \xi}, -1) = 0 \tag{2.26}$$

Equation 2.26 illustrates that the vector $(1, \frac{dF_1}{dC_1}, 0)$ is perpendicular to the vector $(\frac{\partial C_1}{\partial \tau}, \frac{\partial C_1}{\partial \xi}, -1)$. We know that at any point on Γ, the normal vector is given by $(\frac{\partial C_1}{\partial \tau}, \frac{\partial C_1}{\partial \xi}, -1)$. Thus, Equation 2.26 states that the vector $(1, \frac{dF_1}{dC_1}, 0)$ must lie in a tangent plane to Γ. This is shown in Figure 2.6.

Then, the curve ν is constructed on Γ in such a way that at each point on the curve ν the vector $(1, \frac{dF_1}{dC_1}, 0)$ is tangent to the curve, As shown in Figure 2.7.

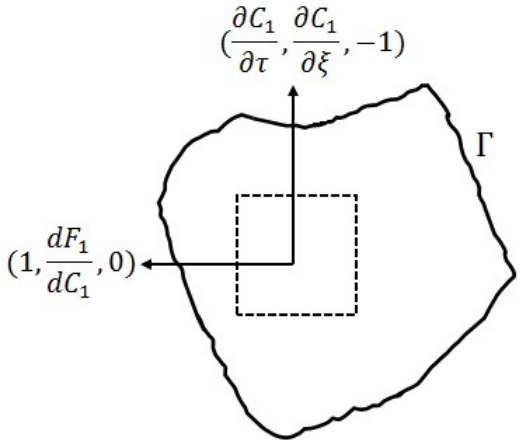

Figure 2.6: Construction of solution using MOC for a two-component gas/oil displacement system

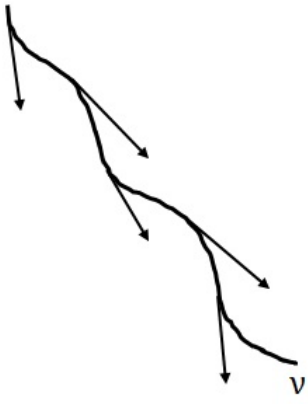

Figure 2.7: Schematic of integral curve ν

The curve ν is written in the parametric form as

$$\nu = \{\tau(\gamma), \xi(\gamma), C_1(\gamma), \gamma \in \mathbb{R}\} \tag{2.27}$$

since curve ν is on the surface Γ it must satisfy

$$\frac{d\tau}{d\gamma} = 1 \tag{2.28}$$

$$\frac{d\xi}{d\gamma} = \frac{dF_1}{dC_1} \tag{2.29}$$

$$\frac{dC_1}{d\gamma} = 0 \tag{2.30}$$

The curve ν is called the integral curve and Equations 2.28 - 2.30 are called characteristic equations. Equation 2.30 illustrates that along curve ν the composition C_1 is constant. Combining Equations 2.28 and 2.29 and upon integration gives an expression for constant values of C_1 is ξ and τ space,

$$\xi = \frac{dF_1}{dC_1}\tau + \xi_0 \tag{2.31}$$

where ξ_0 is the dimensionless location of composition C_1 when no gas is injected into the porous media. Equation 2.31 states that the characteristic curves are straight lines and the propagation velocity of composition C_1 is [45],

$$\frac{d\xi}{d\tau} = \frac{dF_1}{dC_1} \tag{2.32}$$

The velocity at which a given composition propagates is called the wave velocity of

that composition [45]. According to Equation 2.32 to find the solution for a two-component system, $\frac{dF_1}{dC_1}$ should be evaluated for different values of C_1. Multiple solutions might exist that satisfy Equation 2.21 but there is only one solution which is compatible with the physics. The unique solution can be determined based on two facts: the velocity constraint and the entropy condition. The velocity constraint states that, if a wave exists in the solution, the wave velocity must increase monotonically when the path is traced from the upstream side of the wave to the downstream side. The velocity constraint makes the solution single valued. Figure 2.8 displays a situation where the velocity constraint is violated.

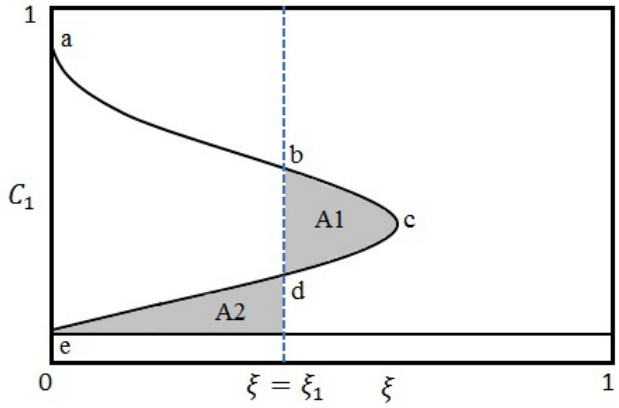

Figure 2.8: Violation of velocity constraint in a typical MOC solution for a two-component gas/oil displacement

As shown in Figure 2.8, tracing the composition C_1 from point "a" at the upstream side, the velocity is monotonically increasing until it reaches a maximum value at point "c", and then starts deceasing to point "e". This causes to have multiple concentration of C_1 at some locations like $\xi = \xi_1$.

The entropy condition comes to play when a shock exists in the solution. It illustrates

that if a shock exists in the solution it must be a stable shock, and to have a stable shock, wave velocities on the upstream side of the shock must be greater than or equal to the shock velocity and wave velocities on the downstream side must be less than or equal to the shock velocity [45]. An example of violation of entropy condition is shown in Figure 2.9.

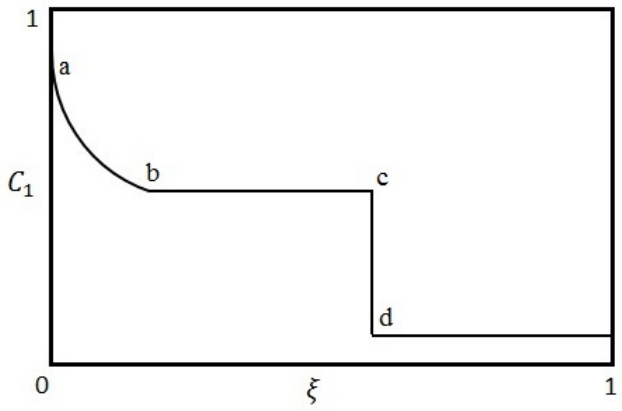

Figure 2.9: Violation of entropy constraint in a typical MOC solution for a two-component gas/oil displacement

Figure 2.9 shows that the velocity on the upstream side of the shock, point "b", is less than the shock velocity, therefore, the shock is not stable and will smear out in the solution by time. Figure 2.10 presents a unique solution where both velocity and entropy conditions are satisfied.

As shown in Figure 2.10, the propagation velocity of compositions are monotonically increasing from point "a" to "b" (veloctiy constraint is satisfied) and the wave velocity at the upstream side of the shock a-b, point "b" is equal to the shock velocity. Construction of a shock which satisfies both entropy and velocity constraints is shown in Figure 2.11.

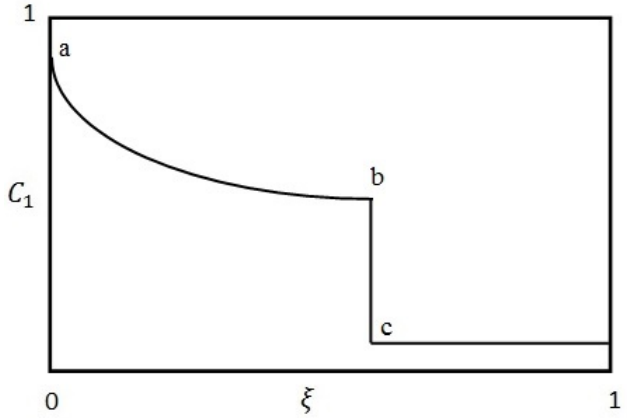

Figure 2.10: Sanctification of velocity and entropy conditions for a two-component gas/oil displacement

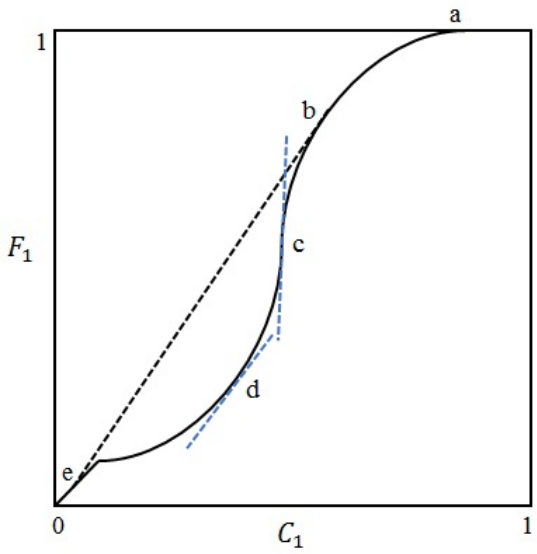

Figure 2.11: Shock construction in a two-component system

Figure 2.11 displays the overall fractional flow against overall composition C_1 in a two-component system. According to Equation 2.32, the propagation velocity of composition C_1 is the slope of the overall fractional flow curve plotted in Figure 2.11. Figure 2.11 shows that starting at point "a" the slope $\frac{dF_1}{dC_1}$ is gradually increasing to a maximum at point "c", and then the slope decreases, therefore velocity starts decreasing. Following this trend leads to the solution presented in Figure 2.8. Even though the material balance equations are satisfied here, the velocity constraint is violated. To resolve the issue, a shock wave is constructed. In order to satisfy the material balance equations, areas "A1" and "A2" must be equal in Figure 2.8. This leads to the Rankine-Hugoniot condition which is the integral form of the mass conservation equation,

$$\Lambda^{be} = \frac{F_i^b - F_i^e}{C_i^b - C_i^e} \tag{2.33}$$

where, b and e are the upstream and downstream sides of the shock and Λ^{be} is the shock speed. F_i^b, F_i^e, C_i^b, and C_i^e represent the overall flux and and the overall composition of the component i at the upstream and the downstream side of the shock, respectively. The solution construction becomes more complicated as the number of components increases in the system. In three-component systems, two key tie-lines, the injection gas tie-line and the initial oil tie-line, control the solution and a new path, a nontie-line path appears in the solution. In four-component systems, a new tie-line known as crossover tie-line appears in the solution. A schematic solution for three-component and four-component systems are shown in Figures 2.12 and 2.13, respectively. The detailed procedure for determining the composition path is described in Section 3.2.1 in Chapter 3.

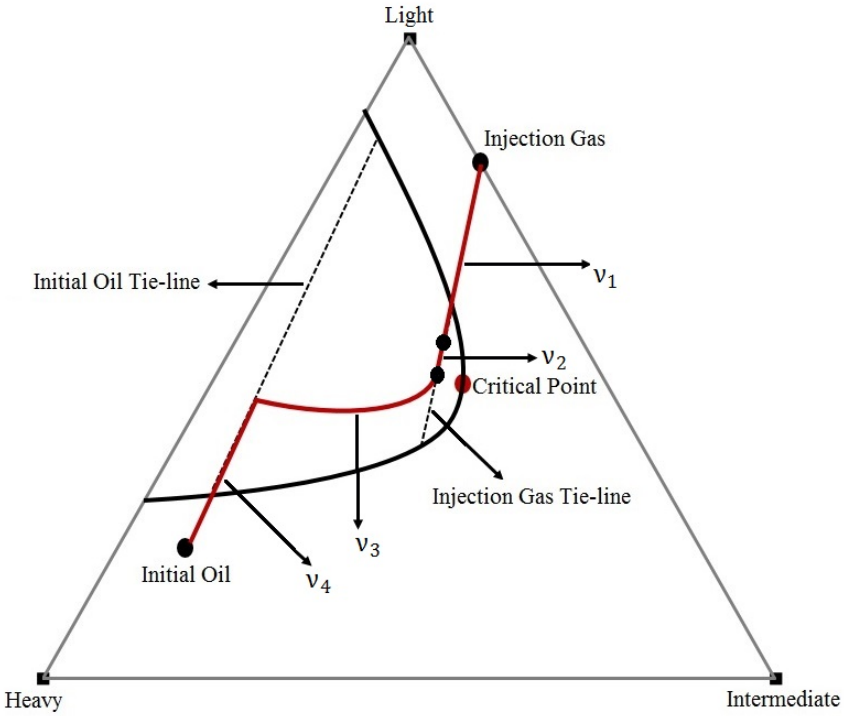

Figure 2.12: A typical solution for three-component systems

2.3 Analytical Solutions for Two and Three-phase Systems

Conservation of mass in an arbitrary control volume in a one-dimensional, dispersion-free displacement leads to a Riemann problem that may be solved analytically. Buckley and Leverett [4] were the first who found the analiytical solution for this Riemann problem for displacement of oil by water. This is the fractional flow theory where an immiscible fluid displaces another in a one-dimensional space. The conservation equation for such a system is a first order hyperbolic partial differential equation in time and space, i.e.

$$\frac{\partial S_w}{\partial t} + \frac{u_T}{\phi}\frac{\partial f_w(S_w)}{\partial x} = 0 \tag{2.34}$$

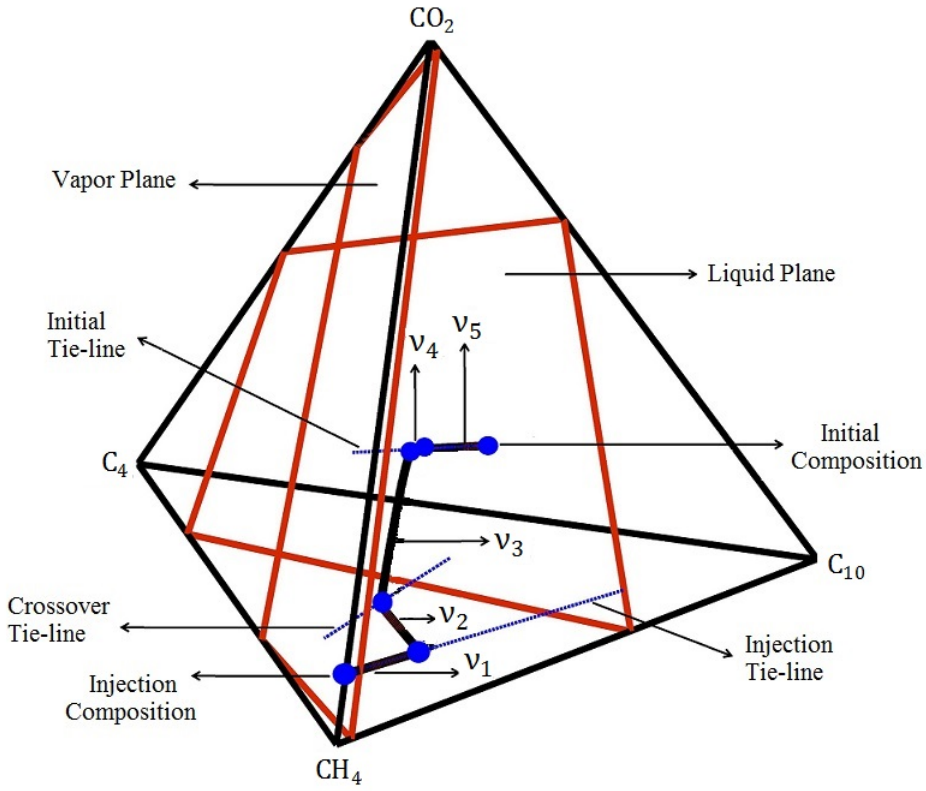

Figure 2.13: A typical solution for four-component systems

In Equation 2.34, S_w is the water saturation, t is the time, ϕ is the porosity, x is the distance from the inlet, f_w is the fractional flow of water and u_T is the total velocity where $u_T = constant$. Buckley and Leverett [4] obtained the water saturation distribution and estimated the velocity of the water front moving in the one-dimensional space. A schematic of their solution is shown in Figure 2.14.

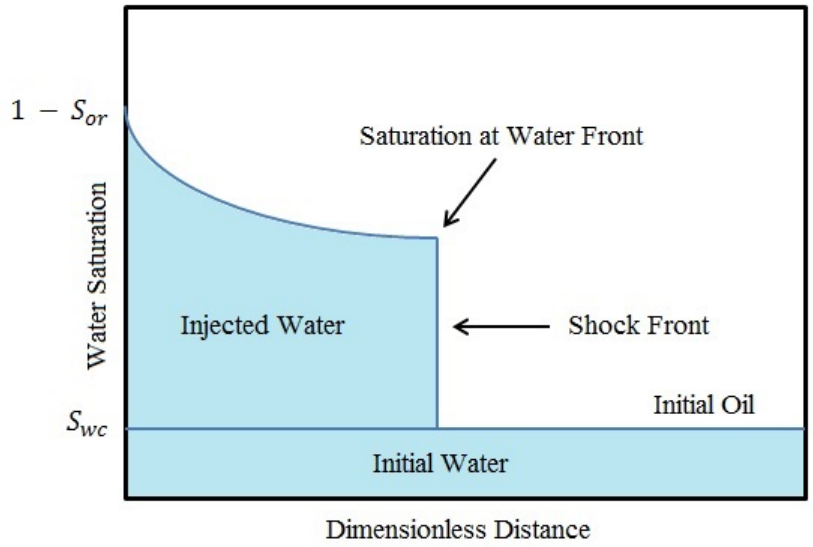

Figure 2.14: An schematic view of Buckly-Leverett [4] solution for water/oil displacement in porous media

Figure 2.14 shows how the injected water moves through the porous media. The water saturation decreases monotonically from a maximum value at the injection well to the shock front saturation at the leading water bank. Buckley and Leverett [4] discovered that each water saturation moves through the porous media with the following equation,

$$\frac{\partial x}{\partial t} = \frac{u_T}{\phi} \frac{f_w(S_w)}{\partial S_w} \tag{2.35}$$

Welge [64] used the Buckley-Leverett fractional flow theory to simulate the oil displacement from reservoirs by gas cycling or gravity drainage. He assumed that the gas pressure was sufficiently constant with respect to time and position to achieve an immiscible displacement. In his method, the gas saturation distribution is not required to calculate the oil recovery and the recovery is determined by computing the average gas saturation and hence numerical integration of the area under saturation profile is avoided. Welge [64] used the below equation to evaluate the average gas saturation,

$$S_{ave} = \frac{\int_{in}^{out} S dx}{x_{out}}, \tag{2.36}$$

where S_{ave} is the average gas saturation and x is the distance from the inlet. Welge [64] used the fact that at any x position the saturation is unique and applied Equation 2.35 to rewrite Equation 2.36 in terms of fractional flow of gas, f, i. e.

$$S_{ave} = \frac{\int_{in}^{out} S df'}{f'_{out}} \tag{2.37}$$

Therefore he changed the variable in Equation 2.36 to f. The numerator in Equation 2.37 was evaluated by integration by parts and the following equation was suggested for calculating the average saturation and hence the recovery factor.

$$S_{ave} = S_{out} - \frac{f_{out} - 1}{f'_{out}} \tag{2.38}$$

Welge et al. [63] presented the analytical solution for the displacement of oil by

enriched gas in a three-component, two-phase flow system. They extended the calculations to actual crude oil-natural gas systems by lumping the components into three groups based on their equilibrium ratios (K-values). A typical solution for a crude oil divided into light, intermediate, and heavy components is shown in Figure 2.15.

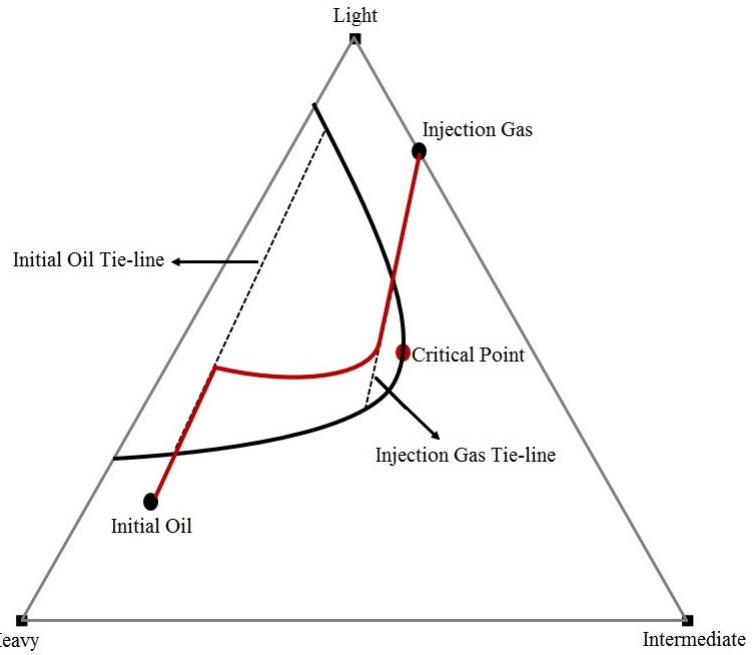

Figure 2.15: A typical analytical solution for three-component gas/oil displacement

Figure 2.15 shows that two main gas/oil equilibria are developed in the system; a trailing mixture along the injection gas tie-line and a leading mixture along initial oil tie-line. In the trailing mixture, some of intermediate components are condensed into the oil and create an oil which is lighter than the initial oil present in the system. Development of this low viscosity oil helps to increase the recovery factor in the injection process. This work was an extension of the Buckley-Leverett [4] solution for the immiscible displacement of oil by water. They improved the method

for partially miscible displacement by considering the condensation of some of the intermediate components from the injected gas into the oil and also considering the effect of temperature and pressure on the volatility of heavier components. They used consolidated sand cores and unconsolidated glass beads to confirm the recovery predictions. A strict three-component system, methane, propane, and soltrol in sandstone models, at 2000 psia and 80 ^oF, and a multi-component crude oil system in the glass bead models, at 2000 psia and 220 ^oF, were used in the experiments. They predicted the recovery factor of soltrol in three-component system as well as oil recovery in the multi-component system versus the pore volumes of injected gas. The experimental results confirmed their theoretical predictions.

Wachmann [59] extended the Buckley-Leverett theory to alcohol injection. This work included a three-component and two partially miscible phase system. Three cases were discussed in their research; a system of two immiscible phase displacement (Buckley-Leverett case), a system of two partially miscible phases as an extension of the Buckley-Leverett theorem, and a system of three components including pure alcohol injection or alcohol-rich fluid injection. However, they concluded that under the assumption of one-dimensional flow with chemical equilibrium and no longitudinal mixing, a piston like displacement is possible by pure alcohol and alcohol-rich slugs injection. Longitudinal mixing is unavoidable in reality in the field or in laboratory experiments and one-dimensional flow with chemical equilibrium is hard to achieve in the lab unless a narrow and long porous medium is provided for the experiment and enough time is given to the fluids to reach equilibrium.

Johansen and Winther [29] analyzed the global Riemann problem for polymer flooding problems with nonlinear adsorption. Johansen and Winther included a term to

model the adsorption effects. They proved that the system of equations modeling the polymer flooding are smooth functions. They confirmed their theory with numerical experiments. However, they found that in some cases the finite difference numerical solution does not detect all the features that exist in the exact analytical solution. Johansen and Winther [30, 31] later generalized their solution for two phase immiscible displacements with an arbitrary number of adsorbing components dissolved in the aqueous phase. First they constructed the solution of an associated Riemann problem for a one-phase system and then applied the projection principle to construct the solution for a system with an arbitrary number of components in the aqueous phase. The projection principle decouples the multi-equation system in the original Riemann problem into a finite series of coupled 2 by 2 Riemann problems. They confirmed their technique with numerical experiments.

The first solutions for four-component systems were reported by Monroe et al. [42]. They used the Method of Characteristics (MOC) and an Equation of State (EOS) to find the composition path in a specific four-component system including CO_2, CH_4, C_4, and C_{10}. Through this research, they studied the effect of adding dissolved methane into the oil displaced by pure CO_2 at 71^oC and 1250 psia. They discovered that oil recovery depends on the location of the crossover tie-line, and that a high displacement efficiency can be achieved if the crossover tie-line is close to the critical point, even though miscibility is not developed. They compared their solution with the core flood experimental data reported by Metcalfe and Yarborough [40]. The experiments reported by Metcalfe and Yarborough [40] were conducted in an $8-ft \times 2-in$ Berea sandstone core, for $CO_2/C_4/C_{10}$ and $CO_2/C_1/C_4/C_{10}$ mixtures at 1500, 1700, and 1900 psia, and 71^oC. Monroe et al. [42] compared the composition path

they derived from analytical solution with the core flood experimental data and found their solution consistent with the experiments.

Johansen et al. [28] and Wang et al. [60] analyzed the mathematical structure of four-component gas/oil displacement systems with constant and variable K-values. They showed that the fundamental conservation law in four-component systems leads to an eigenvalue problem whose coefficient matrix has a triangular structure under specific conditions; either if the tie-lines meet at one edge of the quaternary phase diagram or if the tie-lines lie in planes. They proved that if the K-values are constant, the tie-lines lie in planes. In their work, to perform the analysis, the mass balance equations were written in terms of tie-lines and and the equations of the tie-lines were represented in terms of their slope and intercepts. Johansen et al. [28] proved that in systems with constant K-values, the shock and rarefaction surfaces coincide and in systems with variable K-values the rarefaction surfaces are developable surfaces that are almost planar. Wang et al. [60] used the methodology developed by Johansen et al. [28] to derive the solution for hypothetical three and four-component systems with constant equilibrium ratios and discussed the systems with arbitrary number of components. They also found the composition path numerically and showed that the numerical simulation matched with the analytical solution.

The first solution for three-phase, three-component systems was presented by Laforce and Johns [37]. They applied the MOC to find the solution for one-dimensional, dispersion-free flow of water/alcohol/oil system in which up to three partially miscible phases could be present. In their work, alcohol n-butanol (NBA) and hexadecane, C_{16}, were used to represent the alcohol and oil, respectively. Displacement pressure and temperature were not stated in their paper, however, the phase behaviour of the

water/NBA/C_{16} system was taken from Pongpitak [50]. In three-phase displacements, tie-triangles come into play instead of tie-lines and one to two-phase shocks, one to three-phase shocks, two to three-phase shocks, and intra-three-phase shocks appear in the solution. Laforce and Johns [37] determined the unique composition path by considering the mass balance equation, continuity condition, velocity constraint, and the entropy condition. Their research shows that composition route depends on the injection fluid composition and different types of composition routes are obtained by varying the injection point composition. Also, they discovered that the presence of three phases strongly influences the recovery and unlike two-phase displacements in which recovery increases by enriching the injection fluid, the recovery may remain constant by enriching the injection fluid and it even decreased at some points. They predicted the composition path for water, NBA, and C_{16}, as well as phase saturations' profiles and confirmed by numerical simulations.

Laforce and Johns [35] further applied the MOC to the remediation of aquifers contaminated with nonaqueous phase liquids (NAPLs) via the in-situ injection of surfactant-water mixtures. The conservation equations obtained in their work may either be strictly hyperbolic, non-strictly hyperbolic or mixed hyperbolic and elliptic based on the relative permeability parameters used. Their research shows that the chosen relative permeability data strongly affects the composition route and consequently the contaminant recovery. They predicted the composition path of individual components in a water/surfactant/decane mixture at 25 ^oC and atmospheric condition. Laforce and Johns [35] compared the composition path of water, surfactant, and decane derived by MOC with numerical solutions and found good agreement. They also found that the relative permeability data that lead to non-strictly hyper-

bolic conservation laws result in the highest recovery and those that lead to mixed hyperbolic elliptic conservation equations result in the lowest recovery.

Laforce et al. [36] later used experimental data to confirm the analytical composition routes and profiles obtained by the MOC when three-phase partially miscible flow of three-component mixtures occurs. They performed core flood experiments in vertical glass bead packs to reach a one-dimensional displacement. A ternary system with a large three-phase region at ambient conditions including C_{16}, n-butyl-alcohol (NBA), and distilled H_2O was used to conduct the displacement experiments. The relative permeability data were obtained by matching the Corey exponents to fit the profiles obtained from drainage and imbibition experiments. They conducted drainage (C_{16} injection into NBA and H_2O saturated glass bead pack) and imbibition (NBA and H_2O mixture injection into C_{16} saturated glass bead pack) experiments and compared the analytical solution with experimental data and found that the mathematical model captures the important features of the experimental results.

2.4 Minimum Miscibility Pressure

Miscible displacement of oil has been implemented in a number of field scale projects since the middle of the nineteenth century when different methods such as the Liquified Petroleum Gas slug (LPG-slug) process, the enriched gas-drive process and the high pressure gas-drive process were used to achieve miscibility [54]. Since then, the experimental study of miscible displacements has been expanded from equilibrium phase behavior experiments to displacement experiments in high pressure sand packs. Miscibility helps increase incremental oil recovery by reducing the interfacial

tension to zero theoretically, allowing for the residual oil to be displaced and recovered in all the pore space. Miscibility is dictated by the pressure and temperature specific phase behavior of individual hydrocarbon components, creating one single phase in a transition zone developed between the injected gas and the initial oil. Developing miscibility is evolved by component transfer between the injection gas and the initial oil through vaporizing, condensing, or combined vaporizing/condensing mechanisms. The gas and oil compositions determine the developing miscibility mechanism in the system. Developing miscibility can be achieved either by increasing the pressure or adjusting the composition of the injected gas, assuming the reservoir temperature is constant. If the pressure is not high enough, the displacement process will be immiscible with a recovery factor lower than desired. On the other hand, if the pressure is too high, even though the miscibility is achieved and the recovery factor is substantially increased, the cost of pressurizing the system will be unnecessarily high. Hence, knowledge of the minimum pressure at which miscibility occurs, defined as the MMP, is a crucial part of any gas injection design.

Ternary diagrams help to understand developing miscibility, as shown in Figures 2.16 and 2.17.

As shown in Figure 2.16, each ternary diagram has three apices. Each apex represents 100 % of the component at that apex. Normally, the lightest component is shown at top apex, the intermediate component is shown at the bottom right and the heaviest component is shown at the bottom left apex of the triangle. Three sides of the triangle represent binary mixtures of the two components that lie on that side, with 0 % of component at the apex directly opposite that side. Mole (or mass or volume) fraction of compositions inside the triangle are read from the perpendicular distances from the

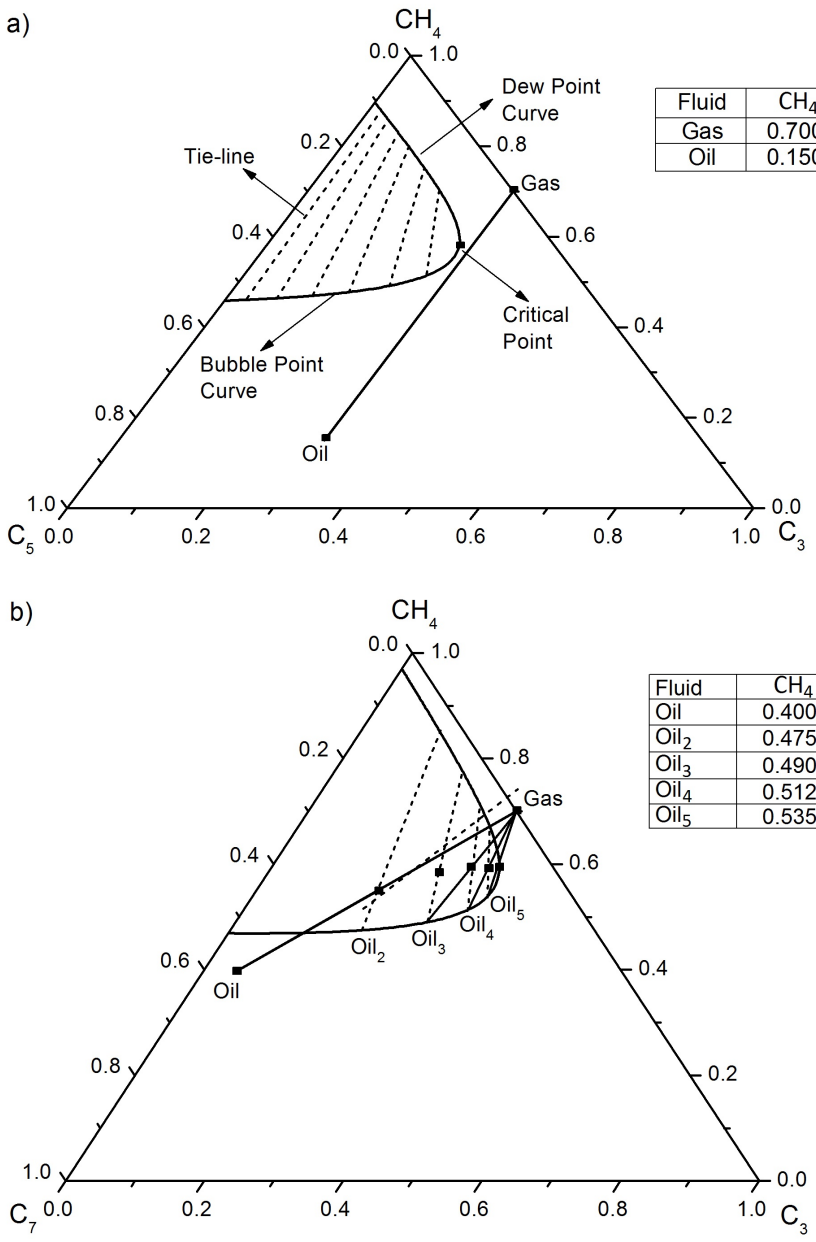

Fluid	CH_4	C_3	C_5
Gas	0.7000	0.3000	0.0000
Oil	0.1500	0.3000	0.5500

Fluid	CH_4	C_3	C_7
Oil	0.4000	0.0500	0.5500
Oil_2	0.4750	0.1904	0.3346
Oil_3	0.4903	0.2769	0.2328
Oil_4	0.5128	0.3224	0.1649
Oil_5	0.5354	0.3394	0.1256

Figure 2.16: Ternary phase diagrams for (a) CH_4-C_3-nC_5 at 1750 psia and 160 ^oF, and (b) CH_4-C_3-C_7 at 2000 psia and 160 ^oF using Peng-Robinson EOS

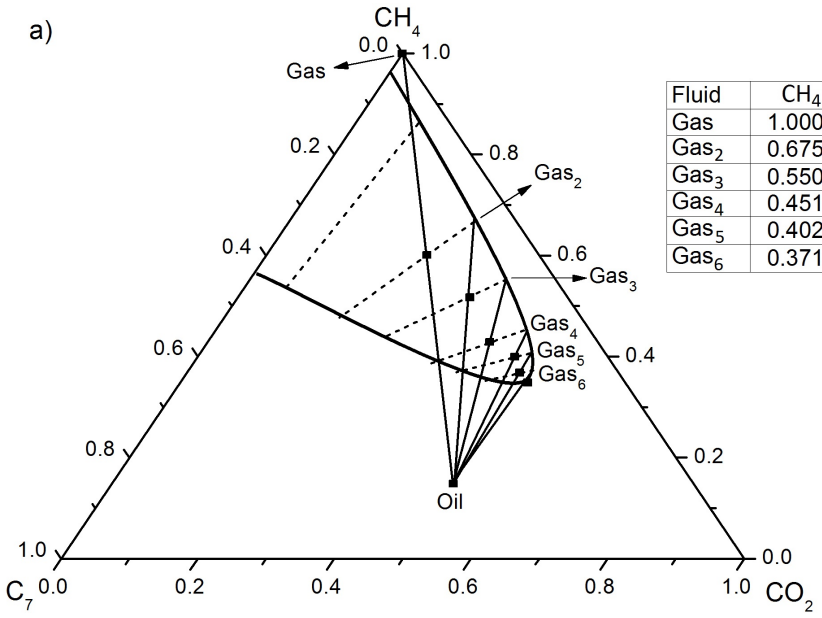

Fluid	CH_4	CO_2	C_7
Gas	1.0000	0.0000	0.0000
Gas_2	0.6751	0.2743	0.0506
Gas_3	0.5502	0.3755	0.0743
Gas_4	0.4511	0.4584	0.0905
Gas_5	0.4027	0.4801	0.1172
Gas_6	0.3719	0.5044	0.1237

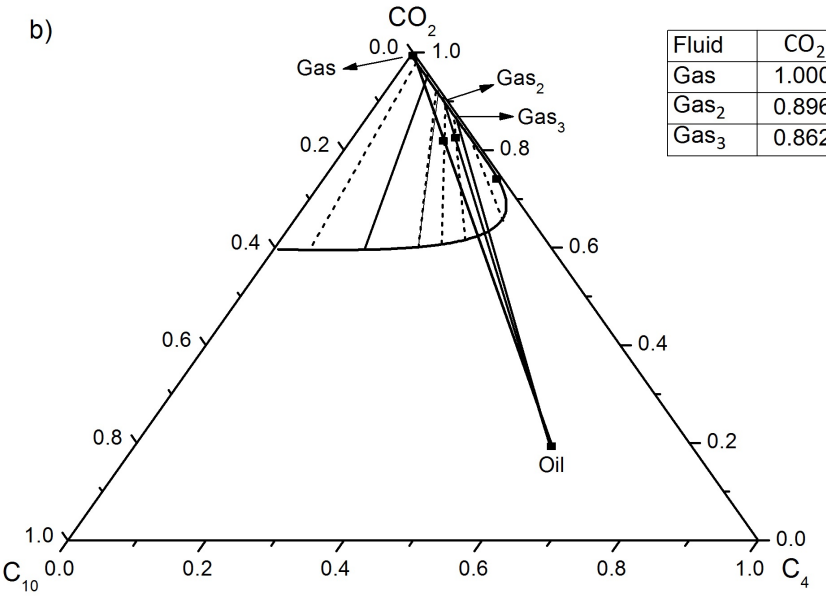

Fluid	CO_2	C_4	C_{10}
Gas	1.0000	0.0000	0.0000
Gas_2	0.8962	0.1012	0.0026
Gas_3	0.8629	0.1338	0.0033

Figure 2.17: Ternary phase diagrams for (a) CH_4-CO_2-C_7 at 1250 psia and 160 ^oF, and (b) CO_2-C_4-C_{10} at 1250 psia and 160 ^oF using Peng-Robinson EOS

composition point to the three sides. In ternary diagrams, the two-phase region is enclosed by binodal curves of liquid and vapor compositions that meet at the critical point. Any overall composition point inside the two-phase region lies on a tie-line connecting the equilibrium vapor and liquid compositions. Therefore, tie-lines can be found by performing flash calculations on overall compositions inside the two-phase region. In these diagrams, the developing miscibility is well described by the fact that the miscibility is controlled by one of the key tie-lines; injection gas tie-line and initial oil tie-line. By the definition the MMP is the lowest pressure at which one of the key tie-lines is the critical tie-line. A critical tie-line passes through the critical point and therefore has zero length.

In gas/oil systems, at any specific pressure, the richness of the injection gas and initial oil from intermediate components is the most important factor in development of miscibility. Figure 2.16a shows a three-component system containing CH_4, C_3, and C_5. In this figure the phase envelope is plotted at 1750 psi and 160 ^oF using the Peng-Robinson EOS. Dash lines in the two-phase region show some of the tie-lines in this ternary system. As indicated in Figure 2.16a, if both the injection gas and initial oil have high enough amount of intermediate components, the dilution line connecting the injection gas to the initial oil lies out of the two-phase region. This means that if the injection gas and the initial oil come together, a single phase fluid will be created, no matter how much gas and oil are mixed. Therefore, the miscibility occurs just after the two fluids come together at the first contact. This is what we know as the First Contact Miscibility (FCM).

Figure 2.16b shows the phase envelope for a three-component system containing CH_4, C_3, and C_7 at 2000 psia and 160 ^oF, plotted using the Peng-Robinson EOS. The most

important factor in developing miscibility in three-component systems is the geometry of the tie-lines. The geometry of tie-lines depends on the components present in the system, the volatility of intermediate component in particular, and reflects the phase behaviour of the fluids. As shown in Figure 2.16b, tie-lines converge at the gas side of the phase envelope. This is because of the low volatility of the intermediate component, C_3, in the system. In the systems with low volatility of intermediate component, developing miscibility through condensing mechanism can be achieved if the injection gas has enough intermediate components. This is illustrated in Figure 2.16b. This figure shows that if the injection gas is rich enough in intermediate components, the miscibility develops after multiple contacts between the injection gas and the initial oil. This shows that when the injection gas and the initial oil meet for the first time, the miscibility does not develop. However, some of the intermediate hydrocarbons are transferred from the gas to the oil to establish a thermodynamic equilibrium. The equilibrium oil is shown as Oil_2 in Figure 2.16b. Since the equilibrium gas has higher mobility than the Oil_2 , it moves faster. Hence, the equilibrium gas moves forward leaving the Oil_2 behind. The equilibrium gas is replaced with the new injection gas which is rich in intermediate components. The fresh gas and the Oil_2 ,which is left from the first contact, make the second contact and establish a new thermodynamic equilibrium. During the second contact, intermediate components are transferred from the injection gas into the oil phase, creating a new equilibrium oil, Oil_3, which is richer in intermediate components. However, because of higher mobility, the equilibrium gas moves forward and leaves the Oil_3 behind. The equilibrium gas is again replaced with the rich injection gas, establishing a new thermodynamic equilibrium between the injection gas and Oil_3. The procedure is repeated and after each contact

the equilibrium oil becomes richer in intermediate components, i.e. Oil_4, Oil_5, and etc. The procedure is repeated until the equilibrium oil is rich enough to make a miscible contact with the injection gas. In the three-component system shown in Figure 2.16b, equilibrium Oil_6 is rich enough to become miscible with the injection gas. The dilution line connecting the injection gas to the Oil_6 does not pass through the two phase region indicating the development of miscibility between the two fluids. This mechanism is know as Multi-Contact Miscibility (MCM) via condensing gas drive as the intermediate hydrocarbons are condensed from the gas to the oil during multiple contacts.

Comparatively, if the intermediate component has a high volatility, tie-lines converge at the liquid side of the phase envelope and developing miscibility through vaporizing mechanism can be achieved if the initial oil has enough intermediate components. This is illustrated in Figure 2.17a by a ternary system containing CH_4, CO_2, and C_7. Figure 2.17a shows the procedure at 1250 psi and 160 ^oF, using the Peng-Robinson EOS for modeling the phase behaviour of the system. The intermediate component in this system, CO_2, clearly has a higher volatility than the intermediate component in previous case, i.e. C_3 in Figure 2.16b. Figure 2.17a shows that if the initial oil is rich in highly volatile intermediate components and the inject gas is a lean gas, miscibility develops after multiple contacts between the injection gas and the initial oil. When the gas and the oil meet for the first time, some of intermediate components are transferred to gas to establish the thermodynamic equilibrium, thus making the gas richer. The equilibrium gas, shown as Gas_2 has higher mobility than the equilibrium oil. Therefore, Gas_2 moves forward and leaves the equilibrium oil behind. As the Gas_2 moves forward in porous media, it meets fresh oil in the reservoir, with high

quantity of intermediate component. Gas_2 makes the second contact with the fresh oil in the reservoir. During the second contact, more intermediate components are transferred into the Gas_2 to establish a new thermodynamic equilibrium. As shown in Figure 2.17a, the result of the thermodynamic equilibrium during the second contact is an equilibrium gas, Gas_3, which is richer than Gas_2. However, Gas_3 moves faster than the equilibrium oil. Gas_3 moves forward, leaves the equilibrium oil behind and makes the next contact with fresh reservoir oil. The procedure is repeated as shown in Figure 2.17a and after each contact the equilibrium gas becomes richer and richer. Eventually, after 5 contacts, the equilibrium gas, Gas_6, is rich enough to make a miscible contact with the reservoir oil. This is known as MCM via vaporizing mechanism, as the intermediate components are vaporized from oil phase to the gas phase to develop the miscibility.

Figure 2.17b shows another scenario for three-component system. In this scenario, the system contains CO_2, C_4, and C_{10} at 1250 psi and 160 ^oF. As shown in Figure 2.17b, since the intermediate component C_4 has low volatility, tie-lines converge at the gas side of the phase envelope. In this case, pure CO_2 is injected to displace an oil which has a high amount of intermediate hydrocarbons. As shown in the figure, at the first contact, some of intermediates are transferred from oil into the gas to create the thermodynamic equilibrium. Like the previous case (c), the equilibrium gas, Gas_2, moves forward, leaving the equilibrium oil behind, and making second contact with the fresh reservoir oil. However, unlike the previous case (c), during the second contact, the equilibrium gas ,Gas_3, does not get much richer than Gas_2. The reason is the low volatility of the intermediate component C_4, therefore, the preference of C_4 to stay in the liquid phase. In fact, this behaviour is reflected in the phase envelope plot

in the direction of tie-lines in Figure 2.17b. As shown in Figure 2.17b, the tie-lines converge sharply to the gas side of the phase envelope which prevents the equilibrium gas acquire richness beyond a certain level. Therefore, in this scenario, miscibility does not develop and the immiscible gas displaces the oil.

From the scenarios discussed above, we show how useful ternary diagrams are to explain developing miscibility but only when miscibility is pure condensing or pure vaporizing. Nevertheless, Zick [68] discovered that a combined condensing/vaporizing drive mechanism is often responsible for developing miscibility in gas flooding projects. In combined condensing/vaporizing drive mechanism, the injected gas establishes thermodynamic equilibrium with the initial oil at several contacts and becomes rich enough to create a condensing drive mechanism further downstream with the initial oil. In condensing/vaporizing mechanism, a crossover tie-line controls the miscibility and becomes the critical tie-line at the MMP. The condensing/vaporizing drive mechanism is well described in four-component systems by Orr [45].

Minimum Miscibility Enrichment (MME) is another important concept associated with gas flooding projects, in which miscibility is achieved through adjusting the composition of injected gas at a constant pressure. The importance of MMP motivated many researchers to develop methods for a rigorous estimation of MMP. To date, several experimental and theoretical methods have been suggested in the literature for the determination of MMP. A review of these methods is demonstrated here.

2.4.1 Experimental Techniques

Accurate determination of the MMP requires experiments that truly rebuild the reservoir environment and capture the transport phenomena in porous media. Over the years, researchers developed numerous experimental methods to measure the MMP. Falling drop, rising bubble, Vanishing Interfacial Tension (VIT), and slim tube tests are the most popular experimental techniques applied to determine the MMP. However, all these experimental techniques are accompanied with advantages and disadvantages. The main features of the experimental methods are pointed in this section.

2.4.1.1 Falling Drop

Christiansen [7] invented the falling drop set up to study the miscibility in gas floods. A schematic view of falling drop set up is shown in Figure 2.18.

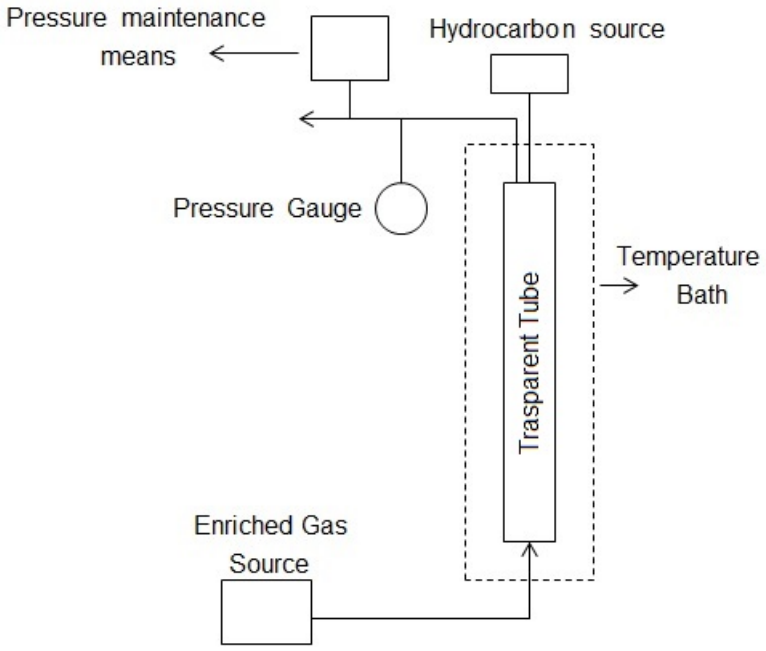

Figure 2.18: Falling drop apparatus designed by Christiansen [7]

In his patent, which is to determine the minimum level of enrichment, an enriched gas is charged into a transparent tube and is maintained at constant pressure and temperature. Then, a droplet of hydrocarbon liquid is discharged from the hydrocarbon source into the gas. The hydrocarbon source is located at the top of temperature bath, as shown in Figure 2.18. The hydrocarbon droplet falls inside the tube under gravity and the droplet is continuously monitored while repeated contacts occur between the droplet and the enriched gas. In the next step, the droplet and the gas are removed from the tube. The gas is replaced with a new gas at the higher level of enrichment and a fresh droplet of hydrocarbon with the same composition as the previous droplet is discharged into the gas. The droplet is again monitored while it falls in the gas column. The procedure is repeated as often as necessary until the hydrocarbon droplet becomes miscible with the enriched gas as a consequence of multiple contacts. This composition of the gas represents the minimum level of enrichment required for a miscible displacement of liquid hydrocarbon. Although this is a cheap and fast method to determine the MME, the method results in a precise estimation of the MMP only when the miscibility mechanism is pure condensing [67]. This is because the oil droplet experiences multiple contacts with the fresh gas as it travels down and at each contact some of the intermediate hydrocarbons of the gas condenses into the oil droplet and after several contacts if the oil droplet is rich enough from intermediate hydrocarbons, the interface between the oil and the gas disappears and the oil droplet becomes indistinguishable from the gas.

2.4.1.2 Rising Bubble

Christiansen and Haines [41] designed the rising bubble apparatus (RBA) to measure the minimum miscibility pressure. A schematic view of the RBA set up is shown in Figure 2.19.

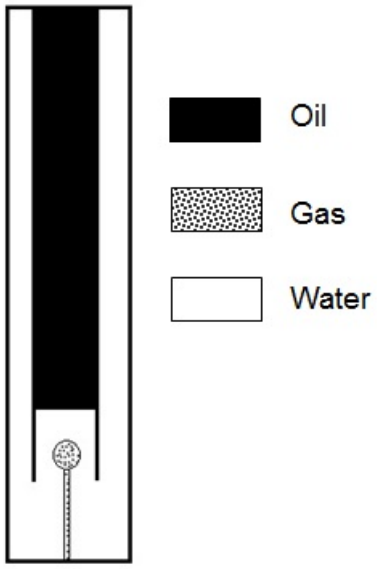

Figure 2.19: Rising bubble apparatus designed by Christiansen and Haines [41]

The RBA apparatus consists of a transparent tube containing a liquid hydrocarbon at a fixed pressure and temperature. A bubble of gas is introduced into the tube at the bottom of the hydrocarbon column, as shown in Figure 2.19. The gas bubble rises in the tube by buoyancy and its shape is continuously monitored while it is moving up. As the bubble reaches the top of the hydrocarbon column, the gas and the liquid are removed and the tube is charged with fresh oil having the same composition as the previous oil. Then, the pressure is increased, while the temperature is kept constant, and a fresh bubble of the gas is injected into the oil. The shape of the bubble is monitored again and the procedure is repeated until the bubble dissipates into

the oil. The pressure at which this happens is recorded as the minimum miscibility pressure. However, similar to the falling drop method, this is a fast and cheap method to determine the MMP but it also has an unavoidable limitation. As inferred from the experimental set up, this method can provide a reliable value of MMP when the miscibility mechanism is pure vaporizing gas drive. This is because the gas bubble has several contacts with the oil as it travels upward and at each contact some of the intermediate hydrocarbons vaporize from the oil phase to the gas phase and after multiple contacts if the bubble is rich enough from intermediate hydrocarbons, the miscibility occurs and the bubble vanishes into the oil. However, Zick [68] found that a combined condensing/vaporizing gas drive mechanism is often responsible for miscibility development in gas injection projects. Therefore, neither of falling drop or rising bubble methods are reliable for determination of the MMP.

2.4.1.3 Vanishing Interfacial Tension (VIT)

Rao [52] presented the vanishing interfacial tension (VIT) technique to determine the MMP and the MME, shown in Figure 2.20.

In this approach, the interfacial tension between the injected gas and the reservoir oil was measured at a fixed reservoir temperature and a set of increasing pressures or enrichments. These measurements are based on the image analysis of a droplet of liquid hydrocarbon surrounded by the injection gas. The interfacial tension is then plotted against pressure or enrichment and the MMP or the MME are obtained by extrapolating the curve to the point at which the interfacial tension is zero. Orr and Jessen [46] analyzed the vanishing interfacial tension technique and discovered that the MMP obtained by this method strongly depends on the overall composition of

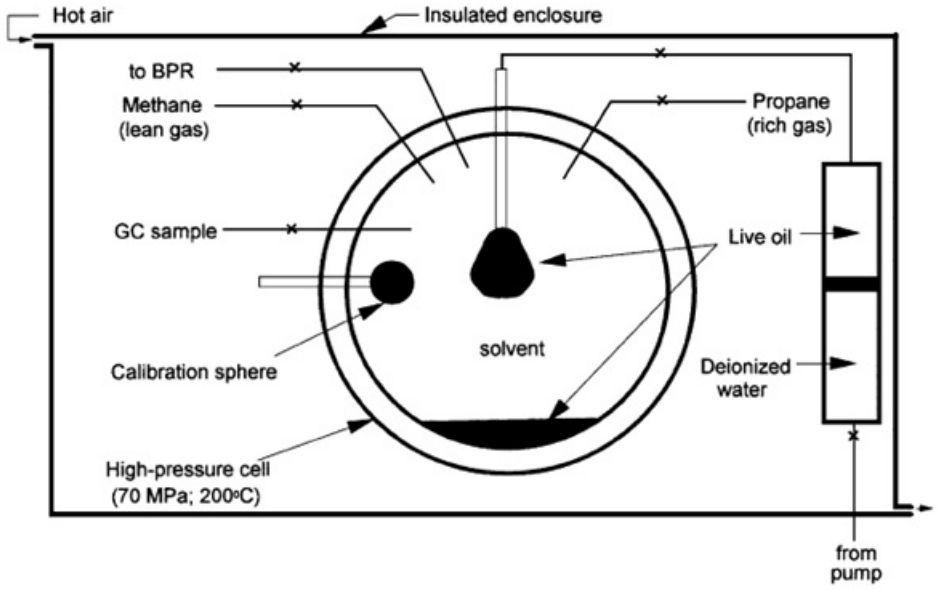

Figure 2.20: Experimental set up to determine the interfacial tension between oil and gas [52]

gas/oil mixture. This is because only overall compositions that are a linear combinations of initial oil and injection gas are considered in this method. In the other words, in this method only one contact happens between the injected gas and initial oil and therefore, the overall composition lies on the dilution line connecting the injection gas composition to the initial oil composition. Jessen and Orr [27] further analyzed VIT method and found that this method is not a reliable tool to determine the MMP.

2.4.1.4 Slim Tube Test

The slim tube test is the most commonly used experimental method to estimate the MMP. In a slim tube set up, the porous media is mimicked by a long narrow tube packed with sand or glass beads. A long tube lowers the dispersion effects and provides multiple contacts between the gas and the oil, where these two conditions are not met in regular gas flood experiments such as core flood. Figure 2.21 is a

schematic view of the slim tube set up used in this research.

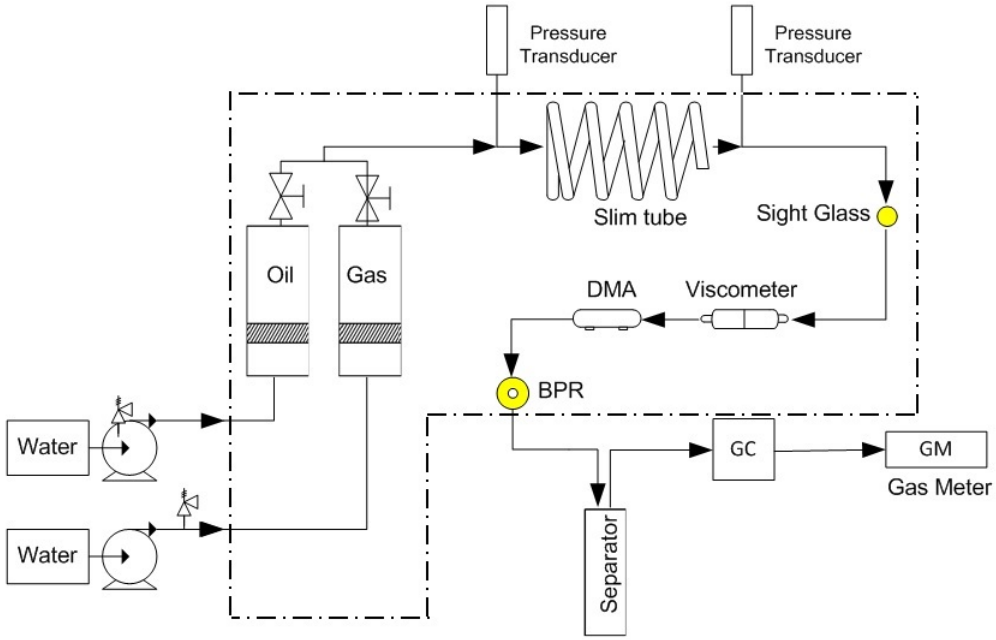

Figure 2.21: A typical view of a slim tube set up

The tube is initially saturated with oil and kept at a constant temperature. Gas is then injected into the tube at a constant flow rate of 0.10 - 0.12 pore volumes per hour to displace the fluid inside the tube. During the test, the fluids from the tube are collected to calculate the recovery factor at the test pressure. The apparatus is then cleaned and the test is repeated in a sequence of increasing pressures. The recovery curve is plotted against different test pressures and the MMP is then obtained from the recovery curve. Figure 2.22 indicates a typical recovery curve against pressure in the slim tube experiments.

Even though the slim tube test is the accepted best practice method to predict the MMP in the oil industry, and it only captures the main interaction of oil and gas in a one-dimensional porous medium. There is neither a standard set up and procedure nor

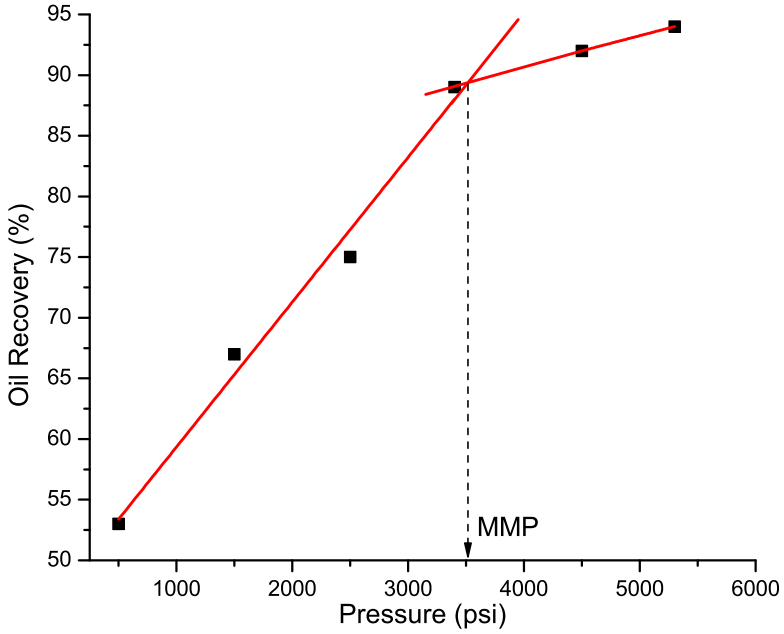

Figure 2.22: A typical recovery curve in the slim tube experiments

a standard miscibility criterion to obtain the MMP [14]. A review of literature shows that slim tube lengths range from 1.5 to 25.6 m, with permeability varying from 1.5 to 24 Darcy with an inside diameter varying from 0.46 to 1.98 cm where the displacement velocities vary nearly two orders of magnitude [47]. However, investigators used different criteria in the definition of the MMP. The most common criterion among the researchers is the bend point in a recovery versus pressure curve when 1.2 pore volumes of displacing fluid is injected [10, 66]. Holm and Josendal [20] defined the MMP as the pressure needed to achieve 80% recovery when gas breaks through. Johnson and Pollin [33] used recovery values of 85% or 90% recovery at the gas breakthrough as the miscibility criterion.

Flock and Nouar [44] performed a parametric study on slim tube experiments and

studied the effect of slim tube length and injection rate on the recovery factor. They found that the recovery factor increases with increasing slim tube length and the recovery versus pressure curve shifts upward by increasing the length. However, the rate of increase in the recovery factor decreases with increasing length. In terms of injection rate, Flock and Nouar [44] did not find any clear effect of injection rate on the recovery factor. Yet, they observed that increasing the injection rate creates a break point in the recovery versus pressure curve. They concluded that increasing the slim tube length has a stabilizing effect on the displacement which makes the effect of injection rate unimportant. Flock and Nouar [44] discovered that increasing the length decreases the viscous fingering effects and a slim tube of at least 12.2 m length is required for a good estimation of MMP. They also recommended not to use the recovery factor, as a sole criterion, for the estimation of the MMP, since recovery is affected by the slim tube length and the injection rate. Instead, they recommended to use the location of the break point on the recovery versus pressure curve, as shown in Figure 2.22, as the MMP criterion.

Thomas et al. [58] compared the slim tube results with the rising bubble apparatus (RBA) results. They performed RBA and slim tube tests on six oil-solvent systems and found that the MMP obtained from RBA tests are normally within 300 psi of the values obtained from slim tube tests. In four cases, the RBA results were larger than the slim tube results, in one case the same results were obtained and in one case the RBA result was less than the slim tube result. However, the general observation was that the MMP values estimated by slim tube were less than those obtained from RBA. Though, the time required to run RBA tests was one tenth of the time needed for slim tube testing.

Wu and Batycky [65] analyzed the miscibility mechanisms through slim tube tests. They concluded that in most cases, a combination of vaporizing and condensing drive is responsible for developing miscibility. Furthermore, Wu and Batycky [65] perceived that the oil recovery, itself, is not a reliable criterion of the miscibility. They suggested to use the analysis of effluent gas composition, visual observation of high pressure effluent phase behaviour, and pressure drop along with the recovery data for the best assessment of miscibility. According to their research, a methane or dry gas peak is observed is miscibility is not achieved, while banking of intermediates in the effluent is detected if miscibility is developed. Visual observation of effluent at the sight glass must show a single phase if miscibility is developed. The pressure drop reflects the flow condition in the slim tube. This helps identifying the miscibility by the fact that upon miscibility a large portion of oil is recovered from the slim tube and, hence, the recorded pressure drop must be consistent with the value calculated with using the slim tube absolute permeability and injection gas viscosity.

Ekundayo et al. [13] later investigated the effect of the slim tube length, injection rate and the inner diameter of the tube on the MMP. Like Flock and Nouar [44], Ekundayo et al. [13] did not find a clear trend between the MMP and the injection rate. They did find a decreasing trend between the tube length and the MMP. To support the findings of Flock and Nouar [44], in their study, two inner diameters were tested and the coil with the larger diameter was found to give a lower MMP. However, the main conclusion of their work, like those presented here, was that not to use the oil recovery as a sole criterion for the minimum miscibility pressure. Instead, they suggest to use the location of the break point, as shown in Figure 2.22, the intersection of two straight lines, on the recovery versus pressure curve as the miscibility indicator.

The cost and time consuming experiments are the major limitations of the slim tube method for prediction of MMP. Yet, the rock and fluid interactions are only captured in slim tube experiments. Also, unlike previously mentioned techniques, this is the only method which considers the combined condensing/vaporizing miscibility mechanism through mobility of gas and oil in the tube. This comprehensiveness of the slim tube tests makes it the only reliable method for the determination of MMP in the oil industry.

2.4.2 Mathematical Techniques

Concurrently with experimental techniques, researchers have been trying to find fast and rigorous mathematical tools to predict the MMP and MME. The most well-known mathematical techniques are critically reviewed in this section.

2.4.2.1 Correlations

Using a correlation is the cheapest and the fastest method to predict the MMP. Numerous correlations are suggested in the literature to estimate MMP [33, 16, 56, 12, 55]. Johnson and Pollin [33] presented the following equation to determine the CO_2 MMP.

$$P_{MMP} - P_{c,inj} = \alpha_{inj}(T_{res} - T_{c,inj}) + I_o(\beta N_M - M_{inj})^2 \tag{2.39}$$

In Equation 2.39, P_{MMP} is the CO_2 MMP in psia, $P_{c,inj}$ is the injection gas critical pressure in psia, $\alpha_{inj} = 18.9 psia/K$, ($T_{res}$ and $T_{c,inj}$ are the reservoir temperature and injection gas critical temperature in kelvin, I_o is the oil characterization index, β

is a constant and equal to 0.285, N_M is the number average molecular weight of the oil and M_{inj} represents the molecular weight of the injection gas.

Sebastian et al. [56] suggested the following correlation to determine the MMP for impure CO_2 injection.

$$\begin{aligned}\frac{P_{MMP,\,impure}}{P_{MMP,\,pure}} =& 1.0 - 2.13 \times 10^{-2}(T_{c,\,g} - 304.2) + 2.51 \times 10^{-4}(T_{c,\,g} - 304.2)^2 \\ & - 2.35 \times 10^{-7}(T_{c,\,g} - 304.2)^3\end{aligned} \tag{2.40}$$

In Equation 2.40, $P_{MMP,\,impure}$ is the MMP of impure CO_2 stream,$P_{MMP,\,pure}$ is the MMP of pure CO_2 injection, and $T_{c,\,g}$ denotes the critical temperature of the injection gas. However, these correlations are based on limited experimental data and are mainly obtained for pure or slightly contaminated CO_2 and N_2 streams. Hence, they will provide reliable values of MMP only when the system under consideration is very close to the reference data on which the correlation is based [25].

2.4.2.2 Mixing Cell Simulation

Another approach is to mathematically simulate a mixing cell to mimic the repeated contacts between oil and gas [24, 43]. In this technique, an EOS is used to describe the phase behavior of the fluids. This method can be conducted in two different ways: forward contacts and backward contacts. In forward contacts, a hypothetical mixing cell is filled with the initial oil and the gas is added to the cell. Flash calculations are performed using an EOS and the resultant liquid is removed from the cell at a constant pressure. Fresh oil is then added to the cell and the procedure is repeated until no change in gas composition is observed. This procedure is shown in Figure

2.23.

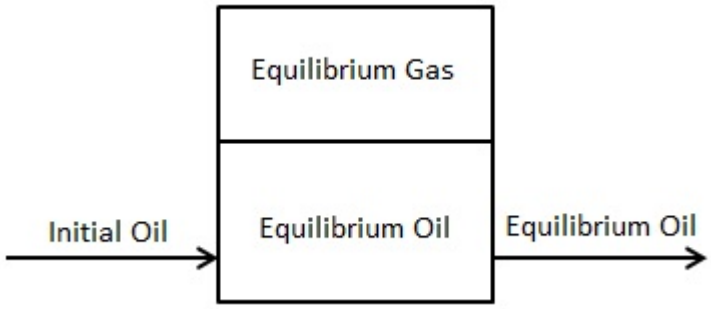

Figure 2.23: Forward contacts single mixing cell simulation at a specific pressure

At this point, equilibrium vapor and liquid compositions are calculated. If all the components have the same composition in the liquid and the gas phases, the test pressure is the MMP. Otherwise, the pressure is increased and the experiment is conducted again until a test pressure is found at which the equilibrium vapor and liquid compositions are identical in the liquid and gas phases at the end of the experiment. Figure 2.24 indicates the logic behind this method. When the gas is injected into the reservoir, it meets the oil just around the wellbore. The injected gas, g_0, and the reservoir oil create a mixture with an overall composition of M_1. After a while, the mixture establishes a thermodynamic equilibrium where the equilibrium gas has a composition of g_1. The gas g_1 moves fast and leaves the equilibrium oil behind. In the downstream path, g_1 meets the fresh oil again and establish a new thermodynamic equilibrium. This step is modeled by removing the equilibrium oil from the hypothetic mixing cell and replacing it with new fresh oil. However, this steps are repeated at each test pressure until the MMP is determined. As can be inferred from the method, in this technique it is assumed that the miscibility mechanism is purely vaporizing.

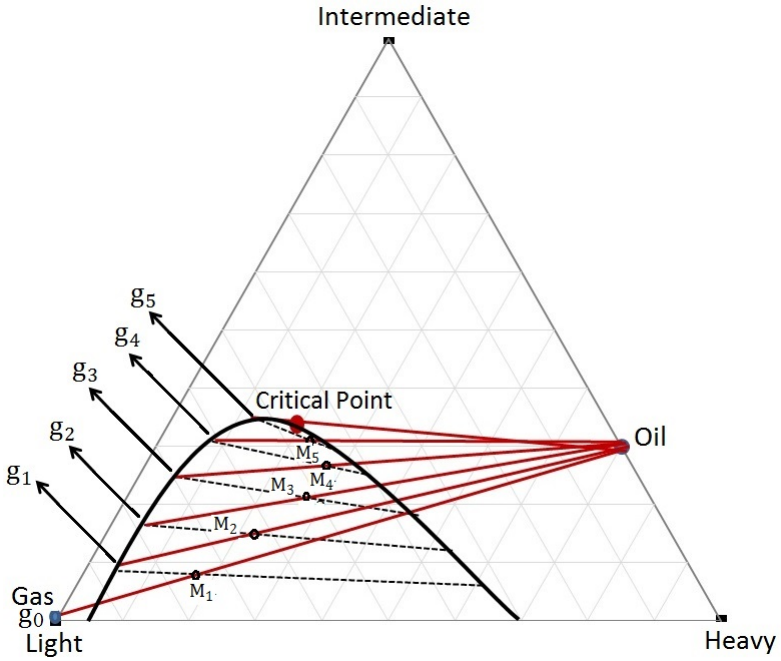

Figure 2.24: Forward contact mixing cell simulation

The procedure for backward contacts is the same as forward contacts except that in the backward contacts the equilibrium gas is removed from the cell at a constant pressure and fresh gas is added to the cell.

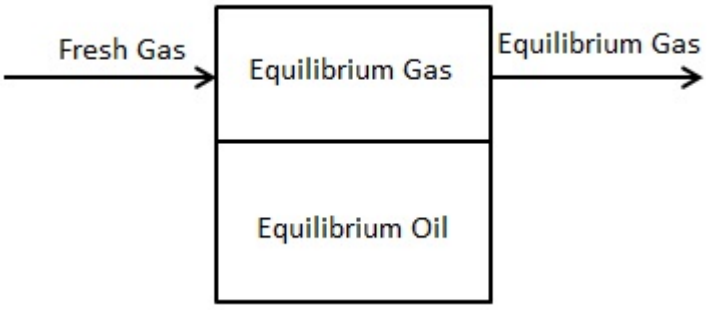

Figure 2.25: Backward contacts single mixing cell simulation

The idea behind backward contacts is illustrated in Figure 2.26.

In the backward contacts, it is assumed that the injection gas is rich in intermediate

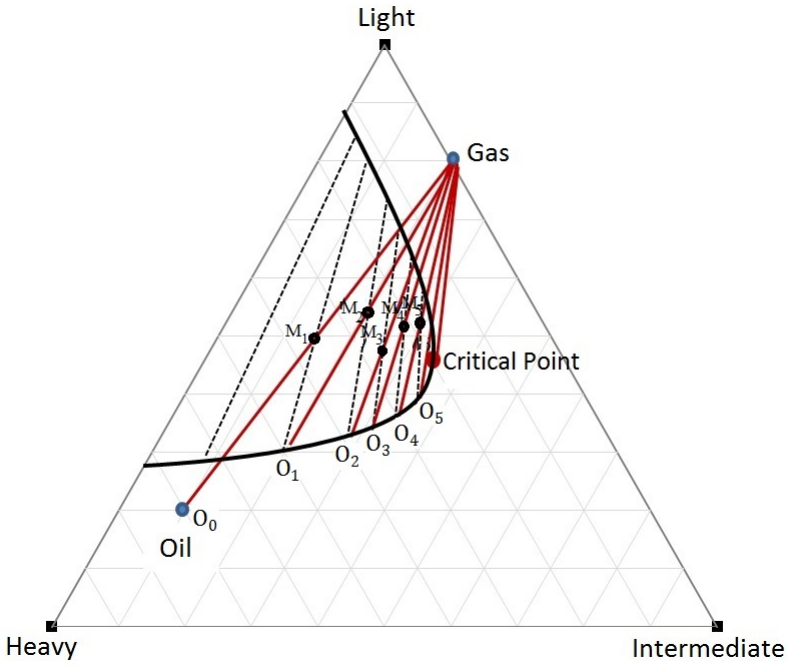

Figure 2.26: Backward contact mixing cell simulation

components. When the gas comes in touch with the reservoir oil, a mixture with an overall composition of M_1 is created. Once the thermodynamic equilibrium is achieved, the equilibrium gas moves away, leaving the eqilibrium oil O_1 behind. The equilibrium gas is then replaced with fresh injected gas. This step is simulated by replacing the equilibrium gas in the mixing cell with the fresh injection gas. The procedure is repeated at each test pressure until the MMP is determined. However, as inferred from the experimental procedure, this technique is suitable when the miscibility mechanism is purely condensing.

2.4.2.3 Multiple Mixing Cell Simulation

Multiple mixing cell methods are the other versions of mixing cell techniques in which a series of interconnected cells are used to study the development of miscibility [22].

In this approach, a batch of injection gas is added to the first cell and with the assumption of chemical equilibrium in the first cell, the flash calculations are performed. The excess volume of the first cell is moved to the next cell and the calculations are repeated for the second cell. The procedure is continued through all the cells and then a new batch of injection gas is added to the first cell. Charging of the first cell is continued until a certain quantity of injection gas is spent. Various mixing cell methods are documented in the literature, which are subject to the study of the development of miscibility rather than calculation of the MMP [23, 39, 48]. Figure 2.27 presents the idea of multiple mixing cell simulation.

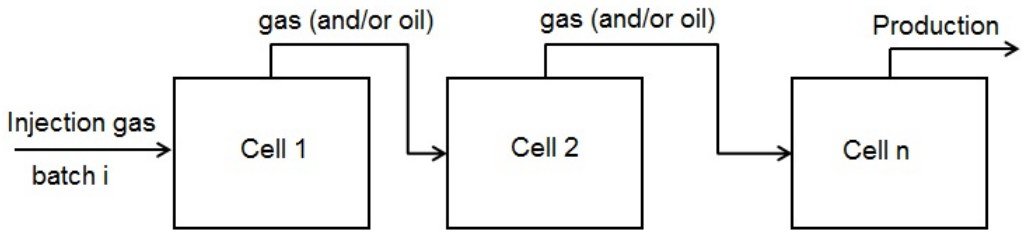

Figure 2.27: Logic of multiple mixing cell simulation [23]

In this technique, 1.2 pore volumes of gas are injected into the system and at a fixed pressure, the recovery factor is calculated with number of mixing cells. The recovery factor is then plotted against $\frac{1}{\sqrt{n}}$ and by extrapolating the recovery curve, the recovery factor is obtained at $n \to \infty$. With the same procedure, the recovery factor is calculated at a sequence of increasing pressures and the MMP is then determined from the plot of recovery vs. pressure.

Ahmadi and Johns [51] later developed a new multiple mixing cell simulation method to estimate the MMP. Unlike conventional multiple mixing cell method, their method

is based on finding the key tie-lines rather than the recovery factor at each pressure. In their method, no flow equation is solved. Instead, flash calculations are performed using an equation of state and the equilibrium gas and oil compositions are calculated. The equilibrium gas in each cell is then moved to the next downstream cell and is mixed with the oil present in that cell. This oil could be fresh oil or and an equilibrium oil which has lost its equilibrium gas to the next further downstream cell. Once three following cells have the same equilibrium gas and oil compositions, a key tie-line is assumed to be found. Applying this approach, all the key tie-lines are found and the length of each tie-line is calculated by Equation 2.41.

$$d_j = \sqrt{\sum_{i=1}^{n_c} (x_i^j - y_i^j)^2} \tag{2.41}$$

In Equation 2.41, d_j refers to the length of key tie-line j, n_c is the number of components present in the system, and x_i^j and y_i^j are the oil and gas compositions on tie-line j, respectively. Using the approach illustrated above, key tie-lines are determined at a set of increasing pressures. The lowest pressure at which one of the key tie-lines has zero length is chosen as the MMP. The multiple mixing cell method developed by Ahmadi and Johns [51] considers purely vaporizing, purely condensing, and combined vaporizing/condensing miscibility mechanisms, as all the key tie-lines are found in this method.

2.4.2.4 Slim Tube Simulation

Simulation of slim tube experiments is another computational option to predict MMP [19]. The tube is divided into a series of grid blocks and the flow equations are solved

numerically over the length of the tube. An EOS is used to describe the phase behavior of the fluids. Recovery factor is calculated at different pressures and a plot of recovery versus pressure is produced. The MMP is then extracted from the recovery plot. Although it could be a cheap and fast alternative to slim tube experiments, it is also prone to numerical dispersion and, as with a real slim tube tests, no standard criterion exists for the definition of MMP.

2.4.2.5 Analytical Methods

Wang and Orr [61] developed the first analytical technique to calculate the MMP in gas injection systems. They started from the theory of one-dimensional, dispersion-free displacement of oil by a gas and showed how to find the key tie-lines. Determining the key tie-lines is based on the assumption that multi-component systems are fully self-sharpening, i.e. all key tie-lines are connected by shocks. Hence, key tie-lines can be identified by the fact that in fully self-sharpening systems, any two neighbor tie-lines must intersect. Intersection of neighbor tie-lines in fully self-sharpening systems is proved by Orr [45]. In Wang and Orr [61], the theory has been applied to systems in which the injection gas contains only one component such as CO_2 and the extension of the theory to cases with more than one component in the injection gas is discussed. Furthermore, Wang and Orr [61] proved that when the injection gas is a single component, exactly one component becomes a zero composition at each intersection point. Then, this fact is applied to find all intersection points and hence the key tie-lines in the system. In the systems with more than one component in the injection gas, however, this fact is no longer true. Therfore, the following set of non-linear equations need to be solved to find the intersection point of the key tie-lines.

This idea is better illustrated by Figure 2.28.

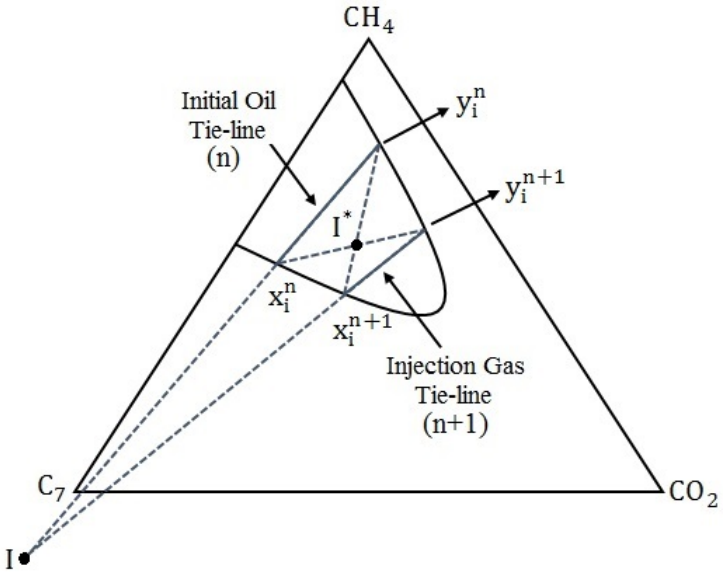

Figure 2.28: Tie-line intersection approach

Assuming that two neighbor tie-lines intersect at point I, the overall composition of all components must be the same in both tie-lines at point I [61].

$$x_i^n \left\{1 + V_n^n \left(K_i^n - 1\right)\right\} = x_i^{n+1} \left\{1 + V_n^{n+1} \left(K_i^{n+1} - 1\right)\right\}, \qquad i = 1, ..., n_c - 1. \quad (2.42)$$

Variables x_i^n and x_i^{n+1} are the liquid compositions of component i on tie-lines n and $n+1$ at the point of intersection, V_n and V_n^{n+1} are the mole fraction of vapor phase on tie-lines n and $n+1$, and K_i^n and K_i^{n+1} represent the K-values of component i on tie-lines n and $n+1$, respectively. Equation 2.42 needs to be solved simultaneously with the material balance equations along the injection and initial oil tie-lines,

$$z_i^{inj} = x_i^{inj}\{1 + V^{inj}(K_i^{inj} - 1)\} \quad (2.43)$$

and

$$z_i^{init} = x_i^{init}\{1 + V^{init}(K_i^{init} - 1)\} \tag{2.44}$$

In Equations 2.43 and 2.44, z_i^{inj} and z_i^{init} are the overall composition of component i in the injection gas and initial oil, x_i^{inj} and x_i^{init} are the mole fraction of component i on the injection gas and initial oil tie-lines, V^{inj} and V^{init} stand for the volume fraction of the vapor phase in the injection gas and initial oil, and finally K_i^{inj} and K_i^{init} represent the K-values of component i on the injection gas tie-line and initial oil tie-lines, respectively. Solving Equations 2.42 - 2.44 gives us the liquid and vapor compositions along key tie-lines, i.e. x_i and y_i, and thereafter the length of each tie-line is calculated from Equation 2.41. However, the procedure is repeated at different pressures and the minimum pressure in which one of key tie-lines becomes zero length is the MMP.

This method for finding the tie-lines suffers from numerical difficulties. Since the intersection of tie-lines lies outside of the two-phase region, very large positive or negative values might be obtained for the oil and the gas saturations. Jessen et al. [26] presented a more efficient technique to identify the key tie-lines. They used an equivalent form of tie-line equations in which liquid and vapor compositions are unknowns and defined a new intersection point that lies in the two-phase region.

Their technique is based on the tie-line intersection approach initially introduced by Wang and Orr [61]. As discussed earlier, in Wang and Orr [61] the intersection point of tie-lines can lie far outside of two phase region and hence can lead to large positive/negative saturation values at this point. Calculation difficulties arise from these unusually large values. In a new formulation, Jessen et al. [26] resolved this

issue by using the fact that a new intersection point must exist for every pair of coplanar tie-lines. Figure 2.28 represents this idea for a three-component system [26]. Point I shows the actual intersection point of two tie-lines and I^* is the new intersection point suggested by Jessen et al. [26]. The system of equations based on the new intersection point, I^*, inside the two-phase region, is as follows,

$$
\begin{aligned}
& x_i^{n+1}(1-\alpha_n) + y_i^n \alpha_n - x_i^n(1-\beta_n) - y_i^{n+1}\beta_n = 0 \quad ; \quad i = 1, ..., n_c, \\
& z_i^{oil} = x_i^{n=1}(1-\beta_{oil}) + y_i^{n=1}\beta_{oil} \quad ; \quad i = 1, ..., n_c, \\
& z_i^{inj} = x_i^{n=n_c-1}(1-\beta_{inj}) + y_i^{n=n_c-1}\beta_{inj} \quad ; \quad i = 1, ..., n_c. \\
& x_i^n \widehat{\phi}_i^{l,n} - y_i^n \widehat{\phi}_i^{v,n} = 0 \quad ; \quad i = 1, ..., n_c, \\
& 1 - \sum_{i=1}^{n_c} x_i^n = 1 - \sum_{i=1}^{n_c} y_i^n = 0 \quad ; \quad i = 1, ..., n_c.
\end{aligned}
\tag{2.45}
$$

In the system of Equations 2.45, α_n and β_n fix the location of new intersection point, I^*, on which based the system of equations is derived. α_n is the fractional distance of the intersection point I^* from liquid composition on tie-line $n+1$ to the vapor composition on tie-line n and β_n is the fractional distance from liquid composition on tie-line n to the vapor composition on tie-line $n+1$. β_{oil} And β_{inj} are parameters that set the location of initial oil and injection gas compositions along initial oil and injection gas tie-lines. Finally, $\widehat{\phi}_i^{l,n}$ and $\widehat{\phi}_i^{v,n}$ denote the fugacity coefficient of component i in liquid and vapor phases along tie-line n, respectively.

The system of Equations 2.45 needs to be solved for x_i^n, y_i^n, α_n, β_n, β_{oil}, and β_{inj} . The set of equations are strongly nonlinear as fugacity coefficients are functions of

liquid and vapor compositions. Hence, an iterative method is required to solve them. In this work, the Newton-Raphson technique is applied to solve the equations. By solving the system of equations, equilibrium vapor and liquid compositions along key tie-lines are determined and hence the length of key tie-lines can be calculated via Equation 2.41.

2.4.3 Summary

In this section all experimental and computational methods for calculation of MMP are briefly compared in Tables 2.1 - 2.4 in terms of their advantages and disadvantages. Table 2.1 summarizes the advantages and disadvantages of the most well-known experimental methods. As indicated in this table the slim tube method is the only approach that has a reliable imitation of what happens in the reservoir. This is because of the nature of this experiment and the set up which is improved over the years by the researchers. None of the other techniques, although they are faster and cheaper than the slim tube, can predict the condensing/vaporizing miscibility drive which is the most common type of miscibility drive in practical cases.

Table 2.1: Advantages and disadvantages of experimental methods for calculation of MMP

Method	**Advantage**	**Disadvantage**
Rising Bubble	Fast and cheap	Unable to predict condensing and condensing/vaporizing mechanism
Falling Drop	Fast and cheap	Unable to predict vaporizing and condensing/vaporizing mechanism
Multiple Mixing Cell	moderate timing and cheap	Unable to predict condensing/vaporizing mechanism
VIT	Fast and cheap	Highly dependent on composition
Slim Tube	Reliable imitation of multiple contacts between the fluids	Expensive and time consuming

Table 2.2 provides a comparison of MMP values obtained from various experimental methods. In this table oils A, B, C, and D refer to different samples used in the stated references for testing the MMP.

Table 2.2: Comparison of MMP values obtained from experimental methods

Method	**Time Order**	**MMP Values (psi)**
Rising Bubble	1 - 2 Hours	Oil A: MMP = 1200 [14] Oil B: MMP = 3650 [14] Cost = $ 15,000 [14]
Falling Drop	Hours	Not commonly used
Multiple Mixing Cell	Days	Oil C: MMP = 2500 [3]
VIT	Hours	Oil D: MMP = 3141 [46]
Slim Tube	Weeks	Oil A: MMP = 1260 [14] Oil B: MMP = 3600 [14] Oil D: MMP = 2200 [46] Cost = $ 40,000 [14]

Table 2.3 is briefly discussing the mathematical methods for calculation of MMP. The main advantages and disadvantages of all main mathematical methods are provided in this table. However, to the best knowledge of the author, analytical methods are the most reliable methods for calculation of MMP. Analytical methods are fast and cheap alternatives to the slim tube experiments. Unlike most of other computational methods, analytical methods are not prone to the numerical dispersion and they can predict the combined condensing/vaporizing miscibility mechanism.

Table 2.4, reported by Wang and Orr [62], compares MMP values estimated from different computational methods and slim tube experiments for the injection of two types of gases; lean gas and reach gas. Wang and Orr [62] calculated the MMP for the two cases using analytical tie-line intersection method and compared the values with

Table 2.3: Advantages and disadvantages of different methods to calculate the MMP

Method	**Advantage**	**Disadvantage**
Correlations	Fast and cheap and able to predict condensing/vaporizing mechanism	Unreliable results and dependent on oil and gas compositions
Single Mixing Cell methods	Fast and cheap	Unable to predict condensing/vaporizing mechanism
Multiple Mixing Cell Simulations	Fast and cheap and able to predict condensing/vaporizing mechanism	Prone to dispersion
Slim Tube Simulation	Fast and cheap and able to predict condensing/vaporizing mechanism	Prone to dispersion
Analytical Methods	Fast and cheap and able to predict condensing/vaporizing mechanism	No disadvantage is observed by the author so far

the single cell and slim tube simulations, as well as experimental results, reported by Hearn and Whitson [18]. A good agreement of analytical methods and experimental results is observed.

Table 2.4: Comparison of MMP values obtained from different calculations [62, 18]

Method	**Lean Gas MMP (psi)**	**Rich Gas MMP (psi)**
Single cell	5860	4540
Slim tube simulation	5860	3225
Analytical Calculation	5253	3115
Slim tube test (experiment)	5215 $\pm$ 200	3315 $\pm$100

Chapter 3

Mathematical Investigation of Constant Pressure Gas Injection

3.1 Introduction

Reservoir simulation starts with writing the governing equations describing displacement process in porous media which results in a set of complicated partial differential equations. The set of equations can be solved either numerically or sometimes analytically to to explain the reservoir behaviour in early times natural production, IOR or EOR process. The numerical approaches are approximate methods and time consuming, yet, they could lead to a rigorous approximation if enough number of grid blocks are used to represent the reservoir. On the other hand, more simplifying assumptions are required if one is to solve the governing equations analytically. Analytical approaches provide a more fundamental understanding and are better to directly analyze the underlying transport phenomena inside the reservoir.

The well-known Buckley-Leverett fractional flow theory, as stated in previous chapters, is based on the assumption of constant total flow rate, i. e. $u_T = constant$. For most laboratory and field scale IOR/EOR processes, the pressure is fixed at the injection and the production wells. More particularly, when the injection fluid is gas, it is difficult to control the flow rate and fixed injection and production pressures would be a more feasible scenario. Under this boundary condition, u_T would be a function of time and the Buckley-Leverett theorem is no longer applicable. Johansen and James [32] generalized the Buckley-Leverett theorem for constant pressure boundary condition.

In this chapter, the methodology developed by Johansen and James [32] is applied for practical gas injection cases. First, the mass balance equations are briefly reviewed. Then, two types of boundary conditions, i.e. (1) constant flux boundaries and (2) constant pressure boundaries, are discussed. The deployment of these boundary conditions into mass balance equations is explained and it is illustrated how the solution of systems with constant flux boundaries can be used to derive the solution of the corresponding systems with constant pressure boundaries. Finally, three case studies are discussed for the further clarification of the newly developed analytical solution. Also, the analytical procedure introduced by Jessen [25] is applied to determine the MMP to be corroborated by the experimental results in the future.

3.2 Mathematical Methodology

It is shown in Chapter 2 that conservation of mass in a one-dimensional, dispersion-free porous media leads to a Riemann problem in the form of

$$
\begin{aligned}
&\frac{\partial G_i}{\partial \tau} + \frac{\partial H_i}{\partial \xi} = 0 \quad ; && && i = 1, ..., n_c, \\
&G_i(\xi, \tau) = G_i^{inj} \quad ; && \xi = 0 \quad ; && i = 1, ..., n_c, \\
&G_i(\xi, 0) = G_i^{init} \quad ; && \xi \geqslant 0 \quad ; && i = 1, ..., n_c.
\end{aligned} \tag{3.1}
$$

In Model 3.1 G_i and H_i are the overall molar concentration and the overall molar flow of component i, respectively, τ is the dimensionless time and is calculated in terms of the number of pore volumes of gas injected into the porous medium, and ξ is the dimensionless length and is calculated as a fraction of the medium length, i.e. $\xi \in [0, 1]$. G_i^{init} represents the overall molar concentration of component i in the reservoir at the initial time, when no gas is injected, and G_i^{inj} denotes the overall molar concentration of component i at the injection well. Furthermore, it was explained that Riemann problem 3.1 can be simplified to 3.2, if the components do not change volume as they transfer from one phase to the other.

$$
\begin{aligned}
&\frac{\partial C_i}{\partial \tau} + \frac{\partial F_i}{\partial \xi} = 0 \quad ; && && i = 1, ..., n_c - 1, \\
&C_i(\xi, \tau) = C_i^{inj} \quad ; && \xi = 0 \quad ; && i = 1, ..., n_c, \\
&C_i(\xi, 0) = C_i^{init} \quad ; && \xi \geqslant 0 \quad ; && i = 1, ..., n_c.
\end{aligned} \tag{3.2}
$$

In Model 3.2, C_i and F_i are the overall volume fraction and the overall fractional volumetric flow of component i, respectively. To solve the system of partial differential equations in 3.2, the initial and boundary conditions must be known. As stated above, in gas/oil displacement systems, the initial oil composition and the injection

gas compositions constitute the initial conditions. For given initial conditions two following cases are possible for boundary conditions; constant flux boundary condition and constant pressure boundary condition.

3.2.1 Constant Flux Boundary Condition

The constant flux boundary condition which is the main assumption of all traditional displacement problems has been investigated thoroughly by many researchers [4, 64, 63, 59, 29, 42, 28, 37, 34]. A schematic of constant flux boundary condition is shown in Figure 3.1a.

As shown in Figure 3.1a, the gas is injected at a constant flow rate at the left side and the oil is produced with the same flow rate at the right side. During the displacement process, gas overrides the oil and breaks through at the production well. Nevertheless, gas and oil compositions along the porous media are not constant. To find the fluids' compositions, Model 3.2 must be solved first with constant flow boundary conditions. The solution of this, is the gas saturation distribution along the porous media. Then, using the gas saturation profile, the fluids' compositions are calculated along the path. Figure 3.1b shows a schematic solution for the system shown in 3.1a. Figure 3.1b illustrates that the solution consists of rarefaction and rarefaction and shock waves that connect the left state,injection well, to the right state, production well. The saturation profile has a maximum at the left state, S_L, and, through a number of rarefaction and shock waves, decreases to S_R at the right state. The number of elementary waves depends on the number of components present in the system. Generally, more components impose more elementary waves into the solution. Figure

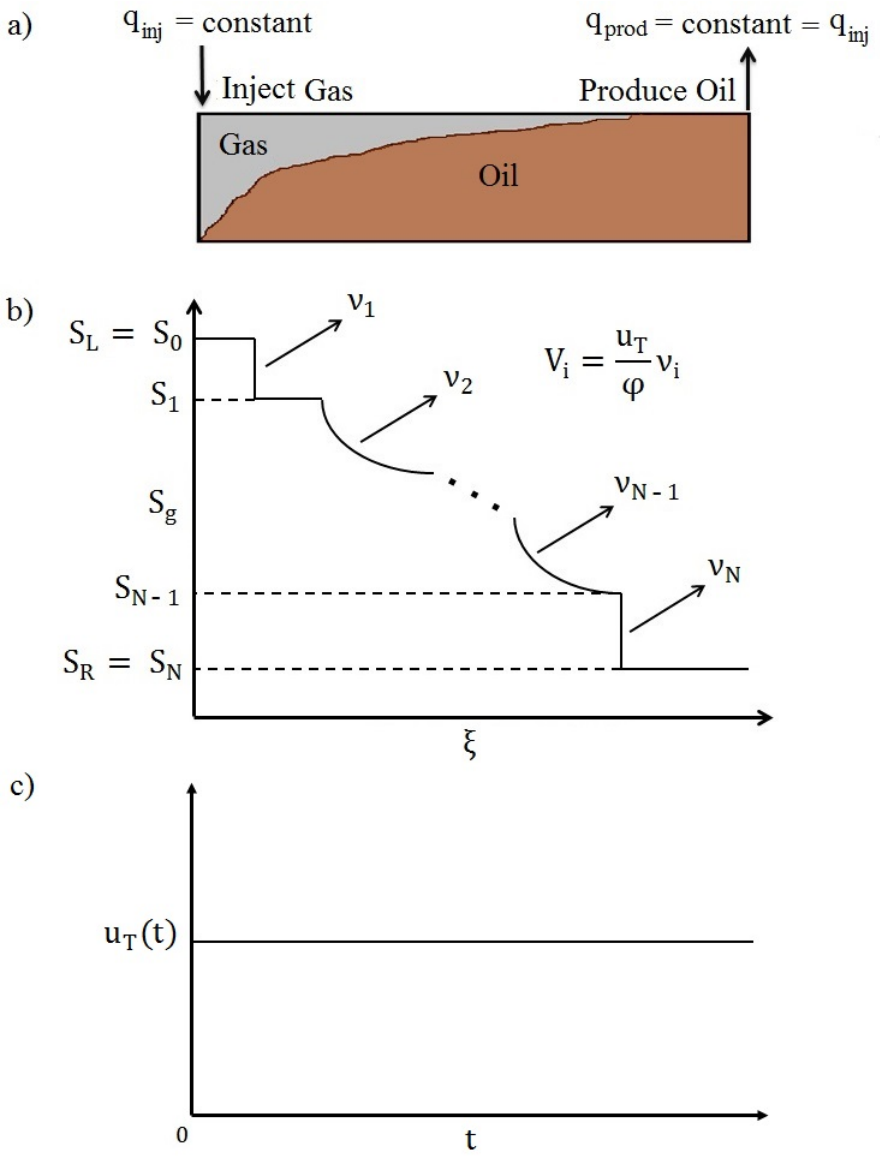

Figure 3.1: a) Schematic of a multi-component gas injection system with constant flux boundary condition, b) Schematic solution of a multi-component gas injection system with constant flux boundary condition, c) Schematic graph of total velocity as a function of time in multi-component gas injection systems with constant flux boundary condition

3.1c, represents the total velocity. As shown the total velocity is constant in problems with constant flux boundary condition. The solution of Model 3.2 is based on Method of Characteristics (MOC) described in Section 2.2.3. Lax [38] proved that this systems have self-similar solutions, i.e. the solution is a function of ξ/τ. Assuming $C = C(\psi = \xi/\tau)$ is a solution of Equation 3.2 and applying the chain rule leads to,

$$\frac{\partial C}{\partial \tau} = \frac{dC}{d\psi}\frac{\partial \psi}{\partial \tau} = -\frac{\xi}{\tau^2}\frac{dC}{d\psi} \tag{3.3}$$

$$\frac{\partial F}{\partial \xi} = \frac{dF}{dC}\frac{dC}{d\psi}\frac{\partial \psi}{\partial \xi} = \frac{1}{\tau}\frac{dC}{d\psi}\frac{dF}{dC} \tag{3.4}$$

Substitution of Equations 3.3 and 3.4 into 3.2, considering that C and F are vectors with $n_c - 1$ independent components, gives

$$\frac{dC}{d\psi}\left(\frac{dF}{dC} - \frac{\xi}{\tau}I\right) = 0 \tag{3.5}$$

or

$$\frac{dC}{d\psi}\left(A - \lambda I\right) = 0 \tag{3.6}$$

where A is a $(n_c - 1) \times (n_c - 1)$ matrix. Equation 3.6 illustrates that as long as $\frac{dC}{d\psi} \neq 0$, λ is an eigenvalue of matrix A and $\frac{dC}{d\psi}$ is an eigenvector. Therefore, the solution of the Riemann problem 3.2 consists of a number of rarefaction, shock waves and constant states connecting the the inlet to the outlet. Each of these elementary waves shown in Figure 3.1b, v_i, belongs to one of the eigenvalues $\lambda_1, ..., \lambda_{n-1}$ obtained by solving the eigenvalue problem 3.6, i.e. $v_i = \lambda_i$. At any value of λ_i the solution lies on a curve in composition space that is tangent to an eigenvector. In the other

words, the eigenvalues $\lambda_1, ..., \lambda_{n-1}$ are the dimensionless velocities at which overall compositions travel and eigenvectors are the directions in composition space along which composition variations satisfy the conservation Equation 3.2. However, the solution of the conservation Equation 3.2 has a form of $V_i = \frac{u_T}{\phi} v_i$, where V_i is the real propagation velocity of elementary wave i and v_i is the elementary wave velocity or the eigenvalue velocity of wave i which is calculated by solving the eigenvalue Problem 3.6, i.e. $\lambda_i = v_i$.

3.2.2 Constant Pressure Boundary Condition

Another possible boundary condition for Model 3.2 is to have constant pressures at the boundaries. Indeed, it is more practical to keep the pressure constant at the injection and the production wells rather than having a constant volumetric flux everywhere in the porous media. Specifically, when the injection fluid is a gas, it is very difficult to keep the flow rate constant, and there are always fluctuations in the flow rate. This boundary condition is schematically shown in Figure 3.2a.

The solution of Riemann problems with constant pressure boundaries were not known until Johansen and James [32] found that the elementary wave solution of the initial value Problem 3.2 with constant flow rate boundaries can be used to determine the solution of associated problem with constant pressure boundaries, i.e.

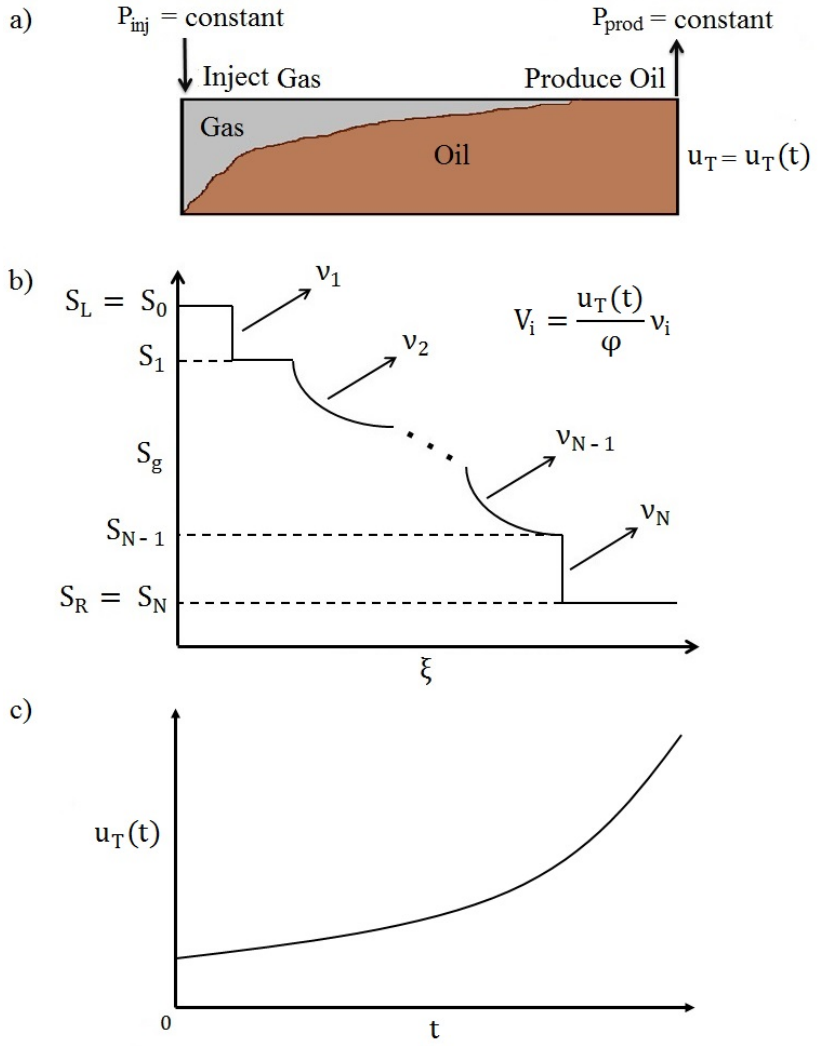

Figure 3.2: a) Schematic of a multi-component gas injection system with constant pressure boundary condition, b) Schematic solution of a multi-component gas injection system with constant pressure boundary condition, c) Schematic graph of total velocity as a function of time in multi-component gas injection systems with constant pressure boundary condition

$$
\begin{aligned}
&\frac{\partial C_i}{\partial \tau} + \frac{\partial F_i}{\partial \xi} = 0 \quad ; && && i = 1, ..., n_c - 1 \\
&C_i(\xi, \tau) = C_i^{inj} \quad ; && \xi = 0 \quad ; && i = 1, ..., n_c - 1 \\
&C_i(\xi, 0) = C_i^{init} \quad ; && \xi \in (0, 1] \quad ; && i = 1, ..., n_c - 1 \\
&p(0, \tau) = p_{in} \quad , \\
&p(1, \tau) = p_{out} \quad .
\end{aligned} \tag{3.7}
$$

In systems with constant pressure boundaries, the total volumetric flux u_T is a function of time, i.e. $u_T = u_T(t)$. However, because of assumed incompressibility, u_T is constant as a function of x. If $V_i = \frac{u_T}{\phi} v_i$ is the solution of the constant flux problem, $V_i(t) = \frac{u_T(t)}{\phi} v_i$ will be the solution of the associated problem with constant pressure boundaries, where v_i is the dimensionless characteristic wave velocity. This is the same in both constant flux and constant pressure boundary problems. Hence, the only time dependent parameter is $u_T(t)$. Therefore, the problem reduces to finding the total volumetric flux as a function of time, $u_T(t)$. This is similar to what Dindoruk found for systems with volume change on mixing. He showed that the eigenvalue problem can be separated into one part that is the no volume change solution and a part that determines the flow velocity [11]. Figure 3.2b and 3.2b show a typical solution of multi-component gas injection with constant pressure boundaries. Comparison of Figures 3.1b and 3.2b shows that the elementary wave solution is exactly the same for both boundary conditions. This is because the elementary wave solution is independent of the boundary conditions and is only a function of the phase behaviour of

the system. Indeed, it depends on the components present in the system and it shows how they are separated in a chromatographic way as they travel in porous media. However, the only difference in the solution appears in the $u_T(t)$ term. Figures 3.1c and 3.2c show the total velocity as a function of time for constant flux and constant pressure boundary conditions, respectively. While the total velocity is constant in constant flux boundary condition, it is monotonically increasing in the gas/oil displacements with constant pressure boundaries. In Section 3.2.3 it is demonstrated how the solution of the problem with constant flux boundaries is used to determine the solution of the corresponding problem with constant pressure boundaries. This is a major contribution of this research.

3.2.3 Solution of the System with Constant Pressure Boundaries

In this research, the solution developed by Johansen and James [32] is employed to calculated the $u_T(t)$ first for a four-component system and thereafter for a five-component system. The five-component system represents a general case with n-components where constant flux problem is solved by the methodology developed by Orr [45]. In this section it is assumed that the solution of the problem with constant flux boundaries is obtained at an average displacement pressure and consists of N elementary waves with the fastest wave v_N as the leading wave and the slowest wave v_1 as the trailing wave. The procedure to calculate the $u_T(t)$ and the breakthrough time of different waves in the corresponding problem with constant pressure boundaries is divided into three periods:

Period 1: the solution before the fastest wave v_N breaks through

The starting point is Darcy's law. Rearranging Darcy's law results in the following equation for the total velocity,

$$u_T = -\lambda_T \frac{\partial p}{\partial x} \quad \Rightarrow \quad \Delta p = u_T \int_0^L \frac{dx}{\lambda_T} \quad \Rightarrow \quad u_T = \frac{\Delta p}{\int_0^L \frac{dx}{\lambda_T}}, \tag{3.8}$$

where p is the pressure and Δp is the differential pressure imposed between inlet and outlet of the medium. Furthermore, x is the distance from inlet and L is the length of the porous medium. Finally, λ_T represents the total mobility defined by $\lambda_T = K \sum_{j=1}^{2} (\frac{K_{rj}}{\mu_j})$, where K is the absolute permeability and K_{rj} is the relative permeability of phase j. To find the total velocity, the integration term in the denominator of Equation 3.8 needs to be evaluated. This can be found by integration by parts and changing the variable. If the viscosities of the phases are constant in the system, the total mobility, λ_T, would only be a function of saturation, S. We assume each wave v_i starts at x_{i-1} and ends at x_i, where the saturation at the upstream side is S_{i-1} and at the downstream side is S_i as shown in Figure 3.3.

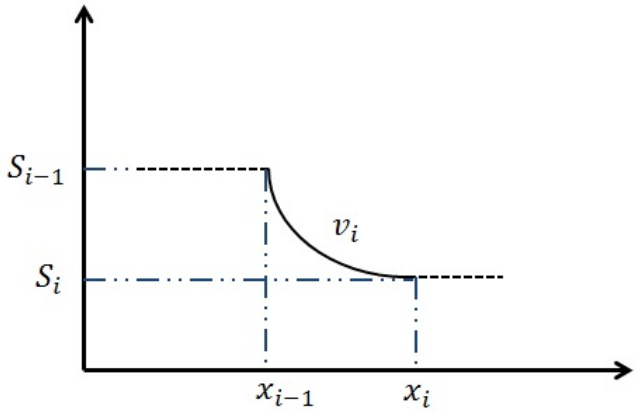

Figure 3.3: Schematic view of a rarefaction wave starting at x_{i-1} and ending at x_i

Then,

$$\int_{x_{i-1}}^{x_i} \frac{dx}{\lambda_T} = \frac{x}{\lambda_T}\Big|_{x_{i-1}}^{x_i} + \int_{S_{i-1}}^{S_i} x(S)\frac{\lambda_T^{'}}{\lambda_T^2}dS = \frac{x_i}{\lambda_T(S_i)} - \frac{x_{i-1}}{\lambda_T(S_{i-1})} + \frac{\psi(t)}{\phi}\int_{S_{i-1}}^{S_i} \frac{v_i\lambda^{'}}{\lambda_T^2}dS$$
$$= \frac{x_i}{\lambda_T(S_i)} - \frac{x_{i-1}}{\lambda_T(S_{i-1})} + \frac{\psi(t)}{\phi}(-\frac{v_i}{\lambda_T}\Big|_{S_{i-1}}^{S_i} + \int_{S_{i-1}}^{S_i} \frac{v_i^{'}}{\lambda_T}dS) = \frac{\psi(t)}{\phi}\int_{S_{i-1}}^{S_i} \frac{v^{'}}{\lambda_T}dS \quad (3.9)$$

where,

$$\psi(t) = \int_0^t u_T(t)dt \quad (3.10)$$

Substitution of Equation 3.9 into Equation 3.8 and further simplification of that results yields the following equation for total velocity:

$$u_T(t) = \frac{\Delta p}{A_N x_N + B_N}, \quad (3.11)$$

where N is the total number of elementary waves and x_N is the location of the leading edge of the fastest wave. If the waves $i = 1, ..., N$ are arranged in order of increasing wave velocities, all the terms with subscript N are valid until the leading wave breaks through. After the leading wave breaks through, the number of the elementary waves reduces by one and there will be another leading wave in the system. Hence, N and all the corresponding terms need to be updated for the new wave structure. The variables A_N and B_N depend on elementary wave solution of the system with constant volumetric flux boundaries, and can be determined by the following equations,

$$A_N = \sum_{i=1}^{N} r_i + \frac{1}{v_N(S_R)}\sum_{i=1}^{N} l_i - \frac{1}{\lambda_T(S_R)}, \quad (3.12)$$

$$B_N = \frac{L}{\lambda_T(S_R)}, \tag{3.13}$$

where,

$$r_i = \frac{v_i(S_{i-1}) - v_{i-1}(S_{i-1})}{v_N(S_R)\lambda_T(S_{i-1})}, \tag{3.14}$$

and,

$$l_i = \int_{S_{i-1}}^{S_i} \frac{v_i'}{\lambda_T} dS. \tag{3.15}$$

As defined in Equation 3.14, r_i generally represents the extension of the constant state between two adjacent waves and l_i in Equation 3.15 represents the span of the elementary waves on eigenvalue axis, which is zero for a shock wave. It is also shown in Johansen and James [32] that x_N satisfies

$$\frac{dx_N}{dt} = \frac{u_T(t)}{\phi} v_N(S_R) = \frac{\Delta p v_N(S_R)}{\phi(A_N x_N + B_N)}, \tag{3.16}$$

where v_N is the characteristic velocity of the leading wave and S_R is the initial gas phase saturation, which also needs to be updated after the breakthrough of each wave. Equation 3.16 is a separable ordinary differential equation with solution given by

$$A_N x_N^2 + 2B_N x_N = C_N t + c, \tag{3.17}$$

where,

$$C_N = \frac{2\Delta p v_N(S_R)}{\phi}, \tag{3.18}$$

and c is an integration constant. It can be calculated if the location of the leading wave is known at time t. Each elementary wave v_i starts from S_{i-1} and ends at S_i. By substituting $x_N = L$, Equation 3.17 can be easily solved to find an explicit expression for the time when v_i breaks through. Knowing the fact that at $t = 0$, the leading wave is at $x_N = 0$, leads to $c = 0$. Hence,

$$t_{BT,N} = \frac{A_N L^2 + 2B_N L}{C_N}, \tag{3.19}$$

where $t_{BT,N}$ is the time when v_N breaks through and therefore,

$$u_T(t) = \frac{\Delta p}{\sqrt{B_N^2 + A_N C_N t}}. \tag{3.20}$$

Period 2: the time after v_N breaks through and before v_{N-1} breaks through

When the leading wave breaks through, three different cases may occur:

Case a: the fastest wave v_N is a shock wave with a constant state behind separating v_N from v_{N-1}.

In this situation, after the breakthrough of shock v_N, the wave structure becomes a new system with $N-1$ elementary waves, where v_{N-1} becomes the new leading wave, and $u_T(t)$ is then calculated exactly as period 1 by removing v_N from the system and putting $S_R = S_{N-1}$.

Case b: the fastest wave v_N is a shock directly connected to rarefaction wave v_{N-1}.

In this case, rarefaction wave v_{N-1} starts to continuously break through just after shock v_N. The calculation of u_T at this period is the same as *Case c* and is described below.

Case c: the fastest wave is a rarefaction wave.

If a rarefaction wave is the fastest wave in the system, S_R is no longer a constant value after the break through of the wave. Indeed, for wave v_N it increases from S_N to S_{N-1}. Figure 3.4 schematically shows how a rarefaction wave continuously breaks through.

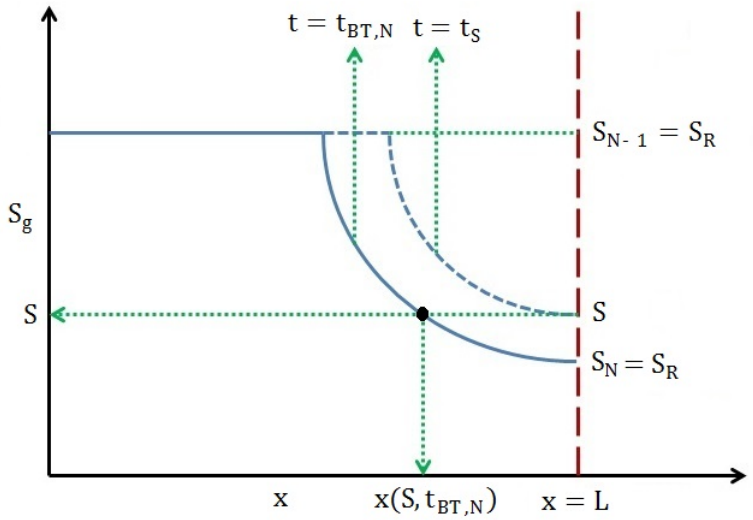

Figure 3.4: Breakthrough of a rarefaction wave

Figure 3.4 shows a rarefaction wave with a downstream edge just broken through at $t = t_{BT,N}$. This rarefaction wave ,v_N, has is defined by downstream saturation of S_N and upstream saturation of S_{N-1}. Now, assuming that S is an arbitrary saturation on this rarefaction wave v_N, this saturation, S, will breakthrough at time $t = t_S$, where clearly $t_S \geq t_{BT,N}$. If $u_T(t_S)$ is the total velocity when the saturation S breaks through, t_S and $u_T(t_S)$ are calculated as follows:

$$t_S = t_{BT,N} + \frac{\phi\left[L^2 - x\left(S, t_{BT,N}\right)^2\right]}{2\Delta p v_N(S)^2}\left\{\sum_{i=1}^{N} r_i v_N(S) + \sum_{i=1}^{N-1} l_i + \int_{S_{N-1}}^{S} \frac{v_N'}{\lambda_T} dS\right\}, \quad (3.21)$$

$$u_T(t_S) = \frac{\phi\left[L^2 - x\left(S, t_{BT,N}\right)^2\right]}{2Lv_N(S)(t_S - t_{BT,N})}, \tag{3.22}$$

In Equation 3.21, $v_N(S)$ is the dimensionless velocity of saturation S on rarefaction wave v_N and $x(S, t_{BT,N})$ is the location of point S at $t = t_{BT,N}$ where it is determined using the following equation,

$$x(S, t_{BT,N}) = \frac{v_N(S)}{\phi}\psi(t_{BT,N}), \tag{3.23}$$

where $\psi(t_{BT,N})$ is given by Equation 3.10. In order to perform the calculations more accurately in this step, we break the entire rarefaction wave into discrete saturation values starting from $S(0) = S_N$ to $S(n) = S_{N-1}$ as follows:

$$\begin{aligned} &S(0) = S_N && , \\ &\vdots && \\ &S(n) = S(n-1) + \Delta S = S_{N-1} && . \end{aligned} \tag{3.24}$$

Since $t_{BT,N}$ and $u_T(t_{BT,N})$ are known, Equations 3.21 and 3.22 can be applied to find the $t_{BT,S(1)}$ and $u_T(t_{S(1)})$. These values can be used to calculate the breakthrough time and corresponding flux of $S(2)$ by replacing $t_{BT,N}$ with $t_{BT,S(1)}$ and S with $S(2)$. The procedure is repeated until the whole rarefaction breaks through and corresponding total flux for all discrete saturation values are known.

Period 3: the time after v_{N-1} breaks through

When the wave v_{N-1} has entirely broken through, the calculations go back to period 1 simply by removing v_{N-1} from the system and putting $S_R = S_{N-2}$. Calculations

are repeated until all the elementary waves break through.

3.2.4 Numerical Simulation

A finite difference scheme is used to solve the model 2.21 numerically. A fully explicit approach, marching forward in time and backward in the space leads to,

$$\frac{C_{i,k}^{n+1} - C_{i,k}^{n}}{\Delta\tau} + \frac{F_{i,k}^{n} - F_{i,k-1}^{n}}{\Delta\xi} = 0 \tag{3.25}$$

In Equation 3.25, i refers to the component, k is the grid block number and n represents the time level. Simplification of this equation results in,

$$C_{i,k}^{n+1} = C_{i,k}^{n} - \frac{\Delta\tau}{\Delta\xi}(F_{i,k}^{n} - F_{i,k-1}^{n}) \tag{3.26}$$

Using Equation 3.26 the overall composition of each component at any grid block and any time level, $C_{i,k}^{n+1}$, is calculated from the overall composition that grid block, $C_{i,k}^{n}$, and overall fractional flow of that grid block and one upstream grid block, $F_{i,k}^{n}$ and $F_{i,k-1}^{n}$, at the previous time level. All the parameters at the first time level are calculated using the initial condition, or the time level zero. Results obtained from this finite difference approach to the analytical results if enough number of grid blocks are used for the simulation. However, the numerical dispersion is unavoidable in this method. The Peclet number for this numerical approach is calculated from Equation 3.27 [45],

$$\frac{1}{Pe_{num}} = \frac{\Delta\xi}{2}\left(1 - \frac{\Delta\tau}{\Delta\xi}\right) \tag{3.27}$$

Where Pe_{num} is the Peclet number. The peclet number must be positive if a stable

solution is to be obtained [45]. Therefore, in the numerical approach $\Delta\tau$ must be larger than $\Delta\xi$.

3.2.5 Workflow and Case Studies

In preceding sections a detailed procedure was described to solve the systems with constant pressure boundaries. In this section, a compressed workflow is provided for an easier following of the mentioned procedure. This workflow is shown in Figure 3.5. Following the workflow shown in Figure 3.5, three case studies are discussed. In Case study 1, four components are present. In this case a two-component gas mixture is displacing a four-component oil. This is a simplified case where the components are assumed to have constant K-values. In Case study 2, a more practical case is tried. In this case a two-component gas mixture is displacing a three-component oil where none of the oil components are present in the injection gas. Peng-Robinson EOS is applied to determine the phase behaviour of the system and no volume change happens upon mixing. In Case study 3, the injection gas and initial oil components are the same as Case study 2. The only difference between Case study 2 and 3 is that the effect of volume change is considered in Case study 3.

3.3 Results and Discussion of Mathematical Developments

Three case studies are discussed and the results are presented here. Case study 1 covers a hypothetical four-component system. In this case study, K-values are given

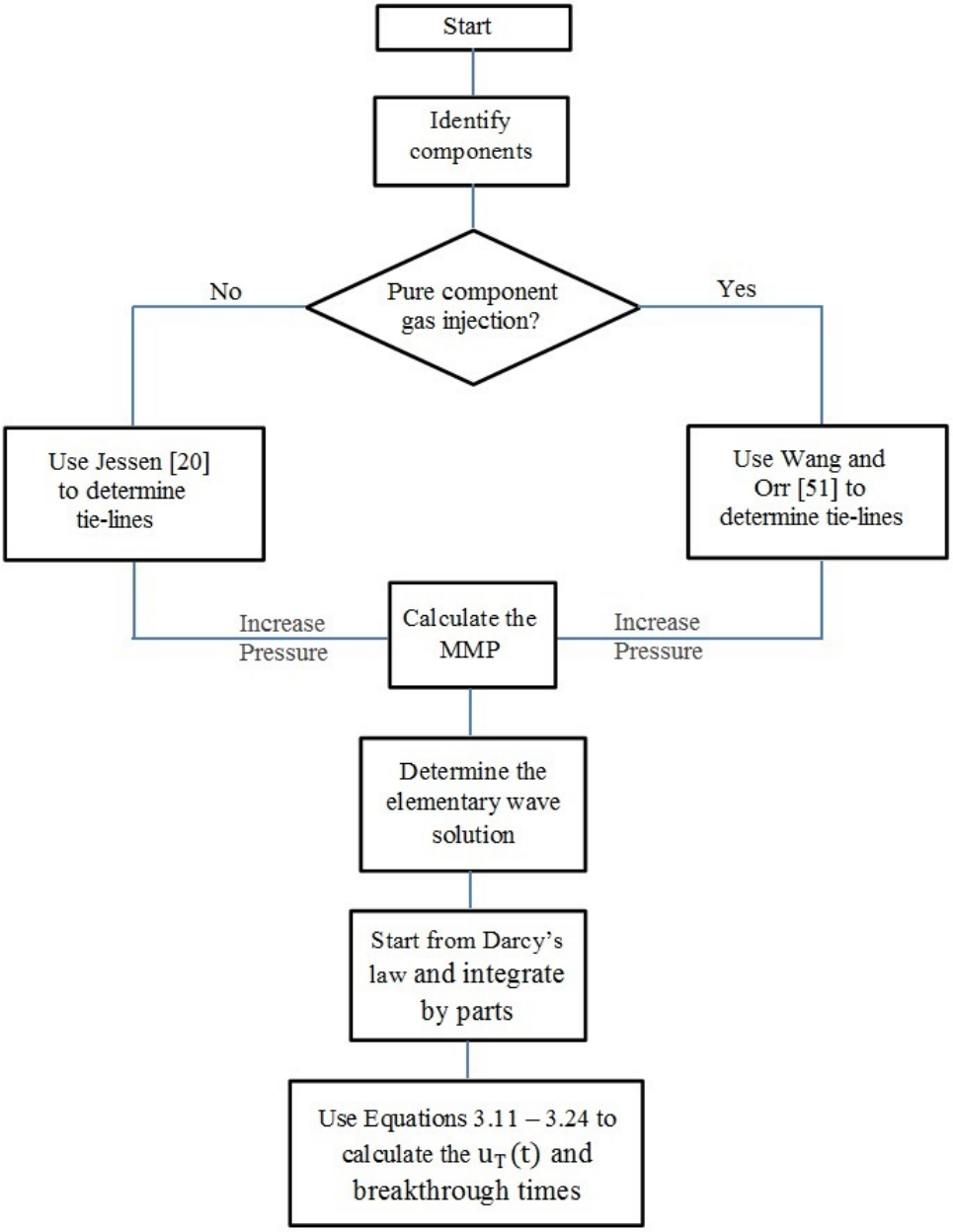

Figure 3.5: Workflow of solving systems with constant pressure boundaries

and assumed to be constant, therefore no phase behaviour calculations is required. This is a preliminary case to apply the procedure presented in Section 3.2.3 for a multi-component gas injection. Case study 2 is a real case scenario, where the results can be verified by experiments. In Case study 2, five-components are present, the displacement happens at reservoir condition, and phase behaviour of fluids is predicted using Peng-Robinson EOS. In Case study 3, the effect of volume change on the results is investigated. The same components as Case study 2 are present in Case study 3, but the displacement happens at a higher pressure. This section explains the application of the theory explained in Section 3.2.3. The confirmation of the results is accomplished through slim tube experiments in Chapter 5.

3.3.1 Case Study 1: Four-component System

In this case study a four-component system is investigated assuming that the injection and the production pressures are constant. Following the procedure described in the Section 3.2.3, the total volumetric flux is calculated as a time dependent parameter and the breakthrough time of different elementary waves is determined using Equations 3.8-3.24. For the sake of simplicity K-values are assumed to be constant. Table 3.1 shows the input parameters for the problem. The initial oil contains four components: CH_4, CO_2, C_4, and C_{10}, and the injection gas is a mixture of CH_4 and CO_2. The viscosity ratio is assumed $M = \frac{\mu_o}{\mu_g} = 10$. The porous media is assumed to be 1.0 meter long, with a porosity of 18 % and an absolute permeability of 1 Darcy. The differential pressure between the inlet and the outlet is assumed to be 344.7 KPa = 50 psi, and $S_{or} = S_{wc} = S_{gc} = 0$. Since the K-values are constant and are given,

the phase behaviour is already known and there is no need for temperature, pressure or phase densities.

Table 3.1: Input parameters for the four-component system (Case study 1)

Component	**Composition (mole fraction)**			
	CH_4	**CO_2**	**C_4**	**C_{10}**
Initial Oil	0.10	0.20	0.30	0.40
Injection Gas	0.90	0.10	0.00	0.00
K-values	2.50	1.50	0.50	0.05

Parameter	**Value**
Oil Viscosity, μ_o (cP)	1.0
Gas Viscosity, μ_g (cP)	0.1
Viscosity Ratio, $M = \frac{\mu_o}{\mu_g}$	10
Displacement Length, L(m)	1.0
Porosity, ϕ	0.18
Absolute Permeability, K(D)	1.0
Inlet Pressure, p_{in} (psi)	1450
Outlet Pressure, p_{out} (psi)	1400
Differential Pressure, Δp (psi)	50
Residual Oil Saturation, S_{or}	0
Connate Water Saturation, S_{wc}	0
Critical Gas Saturation, S_{gc}	0

3.3.1.1 Elementary Wave Solution

In order to derive the solution of the case with constant pressure boundaries, the solution of the problem with constant volumetric flux boundaries must be known. The procedure developed by Johansen et al. [28] and Wang et al. [60] is applied to find the solution for this case. As shown in Figure 3.6, in the four-component system, three key tie-lines exist: the initial oil tie-line, the injection gas tie-line and one crossover tie-line. The structure of the rarefaction and shock waves constituting the solution depends on the geometry of the tie-lines and the geometry of the tie-lines

reflects the phase behavior of the system through the K-values. Figure 3.6 shows the elementary wave solution in the compositional space. The tie-lines and consequently the composition path are found based on the fact that at systems with constant K-values, shock and rarefaction surfaces coincide and are planes [28].

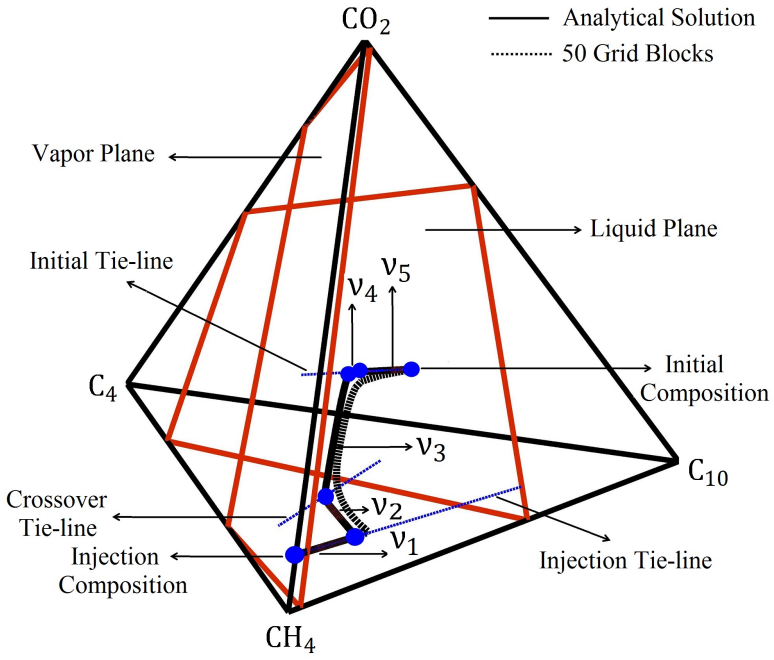

Figure 3.6: Wave structure in compositional space for the four-component system (Case study 1)

Figure 3.6 indicates that starting from the injection composition, the solution jumps into the two-phase region by the shock v_1. v_1 is the trailing wave with the lowest propagation velocity. This shock is followed by another shock wave, v_2, which connects the injection tie-line to the crossover tie-line. The composition path continues with a rarefaction wave, v_3, from crossover tie-line to the initial oil tie-line. Then a rarefaction wave, v_4, occurs along initial tie-line and inside the two-phase region. Finally, shock wave v_5 takes the solution from the two-phase region to the initial

oil composition point. v_5 is the leading wave with the highest propagation velocity. Figure 3.7 shows the saturation against the dimensionless velocity which is another version of elementary wave solution for Case study 1.

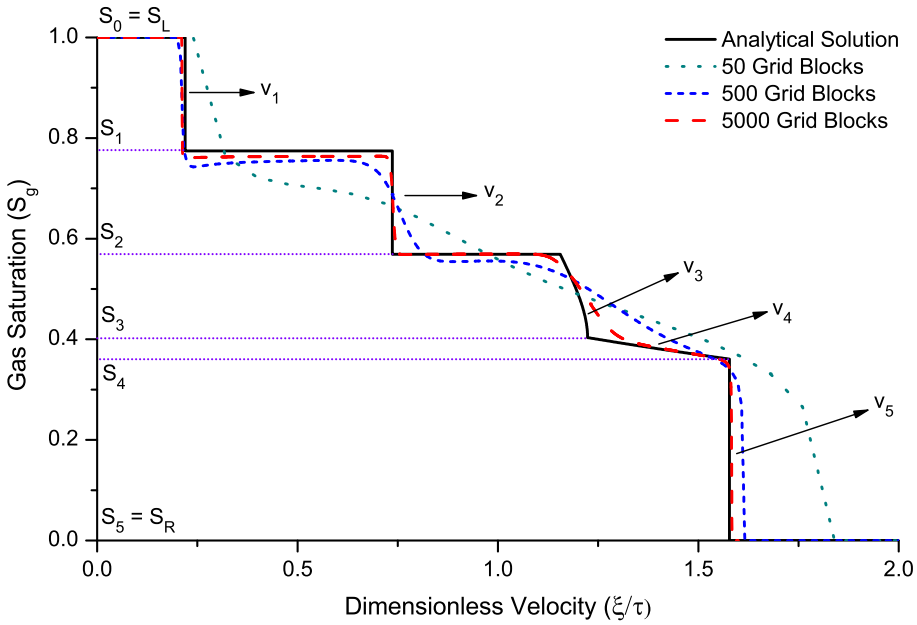

Figure 3.7: Elementary wave solution for the four-component system (Case study 1)

Figure 3.7 clearly shows the propagation velocity of elementary waves in the composition path of Figure 3.6. The saturation profile starts at a maximum gas saturation at the injection gas composition, $S_g = S_0 = S_L = 1$, and decreases as it is traced downstream till it reaches $S_g = S_5 = S_R = 0$ at the initial oil composition. Saturations S_0, S_1, ..., S_5 are the key saturation points where the eigenvalues are changing in the solution. Key saturation points and key tie-lines can be used to calculate the composition profiles of individual components along the composition path. The composition profile for different components is given in Figure 3.8.

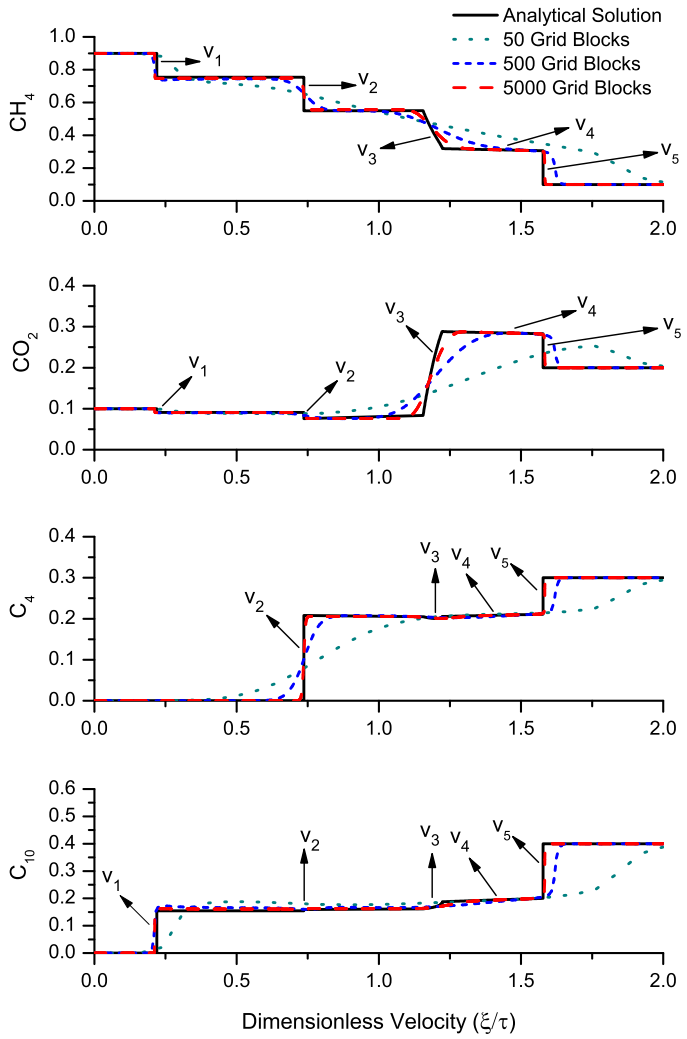

Figure 3.8: Elementary wave solution for the four-component system (Case study 1)

Figure 3.8 illustrates that the leading shock, v_5, is in fact a bank of high concentration CH_4 and CO_2 which moves faster than the other two components, C_4 and C_{10}. It also indicates that behind the shock wave v_2, no C_4 is left at the reservoir. This is consistent with Figure 3.6, where the upstream side of shock wave v_2 is on the $CH_4 - CO_2 - C_{10}$ face of the quaternary diagram, on which C_4 composition is zero. The numerical solutions using different numbers of grid blocks are also presented in Figures 3.6, 3.7, and 3.8. The numerical solution illustrates how difficult it is to obtain sufficient resolution of the elementary waves. As shown in the figures, increasing the number of grid blocks will result in a solution that is closer to the analytical solution. However, a small degree of numerical dispersion is inevitable even with thousands of grid blocks. This numerical dispersion smears the solution and leads to inaccurate estimation of break through time. Furthermore, Figure 3.6 shows that the composition path in quaternary phase diagram is less sensitive to the number of grid blocks. Since the numerical solutions for 500 and 5000 grid blocks are indistinguishable from the analytical solution, only the analytical solution and the numerical solution for the case with 50 grid blocks are shown in the Figure 3.6.

The elementary wave solution in Figures 3.6, 3.7, and 3.8 indicates that the solution consists of two rarefaction waves (v_3, v_4), three shock waves (v_1, v_2, v_5), and three constant states connecting the injection state to the initial state. These elementary waves start and end in key saturation points. Key saturation points and their propagation velocities are provided in Table 3.2.

Individual component recoveries are shown in Figure 3.9. These recoveries are scaled by the initial composition of each component in the porous medium. Hence, the plots indicate the fraction of initial composition of each component that is recovered against

Table 3.2: Key saturation points and eigenvalues

Segment	**Key Saturation Points**	**Saturation Value**	**Eigenvalue**
Injection Gas	$S_L = S_0$	1.0000	1.0000
Trailing	S_0	1.0000	0.2194
Shock v_1	S_1	0.7744	0.2194
Constant	S_1	0.7744	0.2194
State	S_1	0.7744	0.7367
Intermediate	S_1	0.7744	0.7367
Shock v_2	S_2	0.5689	0.7367
Constant	S_2	0.5689	0.7367
State	S_2	0.5689	1.1555
Intermediate	S_2	0.5689	1.1555
Rarefaction v_3	S_3	0.4034	1.2237
Intermediate	S_3	0.4034	1.2237
Rarefaction v_4	S_4	0.3607	1.5777
Leading	S_4	0.3607	1.5777
Shock v_5	S_5	0.0000	1.5777
Initial Oil	$S_5 = S_R$	0.0000	1.0000

dimensionless time, τ, or equivalently against injected pore volumes. This figure shows that almost 1.4 pore volumes of displacing fluid should be injected to recover all the C_4 present in the porous media and almost 4.5 pore volumes must be injected to recover all C_{10} initially in place in porous media. This result is consistent with the composition profiles of individual components presented in Figure 3.8. Figure 3.9 also indicates that the rate of production of CH_4 and CO_2 increases after gas breakthrough (0.6 PV) and the recovery curves for CH_4 and CO_2 have a larger slopes. This is because of the bank of CH_4 and CO_2 moving at the front. Because of this phenomenon and the fact that CH_4 and CO_2 are constituting the injection gas, 100 % recoveries of the CH_4 and CO_2 are achieved by less than one pore volume gas injection.

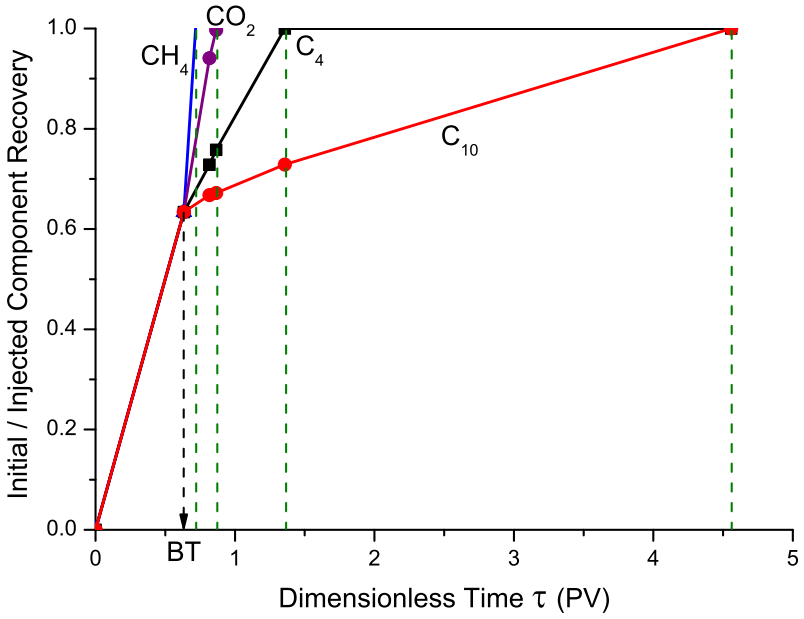

Figure 3.9: Individual component recoveries for the four-component system (Case study 1)

3.3.1.2 Constant pressure boundary solution

Calculation of the break through time and the total flux before the fastest wave v_5 breaks through are shown here as a sample. Using the data provided in Table 3.2, r_i and l_i are first calculated as follows:

$$r_1 = \frac{v_1(S_0) - v_0(S_0)}{v_5(S_R)\lambda_T(S_0)} = 1.3908 \times 10^7,$$

$$r_2 = \frac{v_2(S_1) - v_1(S_1)}{v_5(S_R)\lambda_T(S_1)} = 5.4204 \times 10^7,$$

$$r_3 = \frac{v_3(S_2) - v_2(S_2)}{v_5(S_R)\lambda_T(S_2)} = 7.7571 \times 10^7,$$

$$\Rightarrow \qquad \sum_{i=1}^{N} r_i = 1.4568 \times 10^8. \qquad (3.28)$$

$$r_4 = 0, \quad r_5 = 0,$$

As mentioned earlier, although r_i does not have an exact physical definition, it is somehow a measure of the constant state behind the wave v_i. This is more clear if we compare the calculations in Equation 3.28 with Figure 3.7. This is inferred from Figure 3.7 that there is no constant state behind v_4 and v_5 and therefore, $r_4 = r_5 = 0$. And likewise,

$$l_1 = 0, \quad l_2 = 0,$$

$$\left.\begin{aligned} l_3 &= \int_{S_2} \frac{v_3'}{\lambda_T} dS = 2.4791 \times 10^7, \\ l_4 &= \int_{S_3}^{S_4} \frac{v_4'}{\lambda_T} dS = 1.9290 \times 10^8, \end{aligned}\right\} \quad \Rightarrow \quad \sum_{i=1}^{N} l_i = 2.1769 \times 10^8. \tag{3.29}$$

$$l_5 = 0,$$

In a similar reasoning, l_i is the measure of the length of the wave v_i. Comparison of calculations in Equation 3.29 with Figure 3.7 reveals why $l_1 = l_2 = l_5 = 0$. we also have:

$$v_5(S_R) = 1.5777, \qquad \lambda_T(S_R) = 10^{-9}, \tag{3.30}$$

Hence, A_N, B_N and C_N are calculated from Equations 3.12, 3.13, and 3.18 as follows:

$$A_N = -7.1634 \times 10^8, \qquad B_N = 10^9, \qquad C_N = 6.0433 \times 10^6, \tag{3.31}$$

This leads to the following results for $t_{BT,5}$ and u_T,

$$t_{BT,5} = 212\,s, \quad u_T(t) = \frac{344738}{\sqrt{10^{18} - 43.2906 \times 10^{14} t}}; \qquad t \leq 212\,s. \tag{3.32}$$

3.3.1.3 Total velocity

Figure 3.10 shows the total velocity as a function of time until all the elementary waves break through. In this figure $t = t_3$ is the time when the rarefaction v_3 is completely broken through. As can be seen, due to different type of elementary waves, u_T behaves differently at each time period. However, u_T is generally increasing with time as the less viscous vapor phase saturation is increasing in the medium.

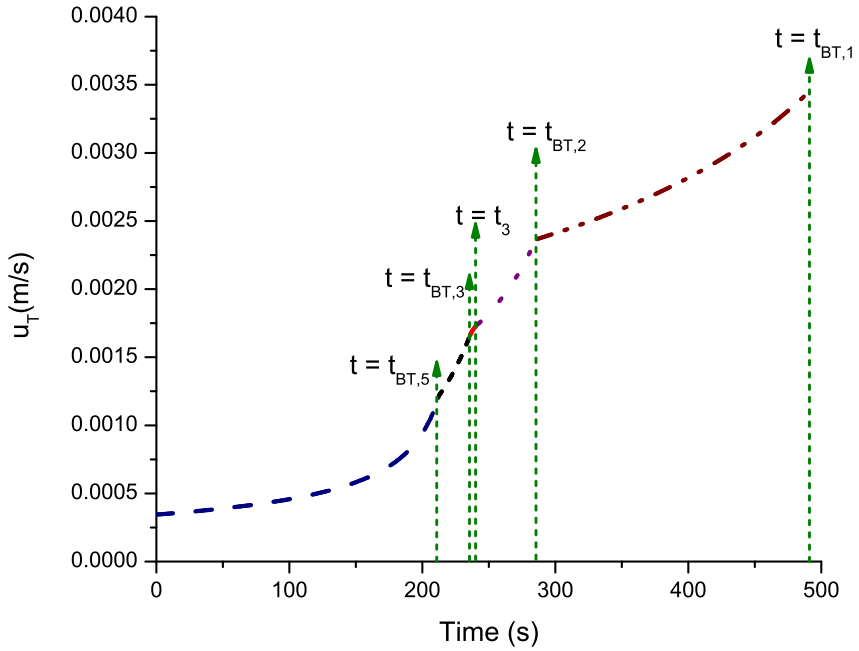

Figure 3.10: Total flux as a function of time for the four-component system (Case study 1)

Figure 3.10 also indicates that the total flux is increasing from $0.0004\frac{m}{s}$ at the begining of the injection to $0.0035\frac{m}{s}$ at the breakthrough of the trailing wave which is almost an order of magnitude.

3.3.1.4 Saturation profile

Once u_T is known, the exact location of each elementary wave can now be calculated at any point in time using Equation 3.23. Figure 3.11 indicates the saturation profile at three times before the fastest wave break through: $t = 0.3\, t_{BT,5}$, $t = 0.6\, t_{BT,5}$ and $t = 0.9\, t_{BT,5}$. It can be seen that, the rarefaction waves and constant states expand as the total flux u_T increases with time. Based on Equation 3.23,

$$x(S,t) = \frac{v(S)}{\phi} \int_0^t u_T(t)dt \tag{3.33}$$

$\int_0^t u_T(t)dt$ Increases with time, and the key saturation point velocities, $v(S)$, is larger at the downstream of elementary waves. Therefore, according to Equation 3.33 the rarefaction waves and the constant states expand with time.

3.3.1.5 Pressure distribution

Since $u_T(t)$ is known, the fundamental Darcy's law can be employed to determine the pressure distribution along the porous media at any certain time,

$$u_T(t) = -\lambda_T \frac{\partial p}{\partial x}, \tag{3.34}$$

The integration of the Equation 3.34 gives,

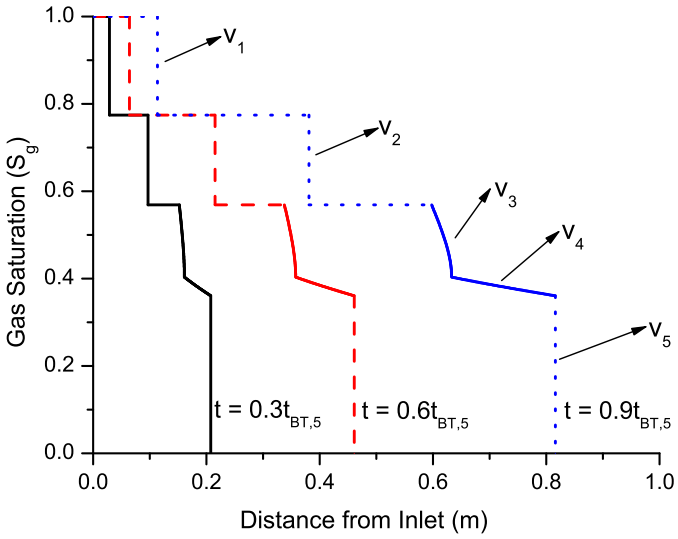

Figure 3.11: Vapor phase saturation before the breakthrough of the fastest wave in constant pressure boundary problem for the four-component system (Case study 1)

$$p_{in} - p_x = u_T(t) \int_0^x \frac{dx}{\lambda_T} \Rightarrow p_x = p_{in} - u_T(t) \int_0^x \frac{dx}{\lambda_T} \tag{3.35}$$

where p_x the pressure value at the distance x from inlet, p_{in} is the pressure at the inlet, and λ_T is the total mobility defined by$\lambda_T = K\left(\frac{K_{rg}}{\mu_g} + \frac{K_{ro}}{\mu_o}\right)$. Determining the pressure distribution using Equation 3.35 can be completed by dividing the porous media into two types of segments: (1) constant state segments, (2) rarefaction wave segments. Along constant state segments, the gas saturation S is constant, therefore so is the total mobility λ_T, and assuming that the upstream side of the constant state segment is the inlet,

$$p_x = p_{in} - \frac{u_T(t)}{\lambda_T} x \tag{3.36}$$

Along rarefaction waves, the total mobility λ_T is no longer a constant value. Indeed,

it is a function of gas saturation and a change of variable from x to S is needed to evaluate the integration in Equation 3.35. This procedure is shown in Equation 3.9. Therefore, the pressure distribution along rarefaction waves, assuming that the upstream side of the rarefaction wave is the inlet, can be calculated from

$$p_x = p_{in} - \frac{u_T(t)\psi(t)}{\phi} \int_{S_{in}}^{S} \frac{v'(S)}{\lambda_T} dS \tag{3.37}$$

where $\psi(t) = \int_0^t u_T(t)dt$, S_{in} is the gas saturation at the inlet, S is the gas saturation at the distance x from the inlet, and $v(S)$ is the wave velocity of saturation S. Figure 3.12 shows the pressure distribution along with the gas saturation at $t = 0.3\,t_{BT,5}$, $t = 0.6\,t_{BT,5}$, and $t = 0.9\,t_{BT,5}$, at different locations in porous media for the four-component system in Case study 1.

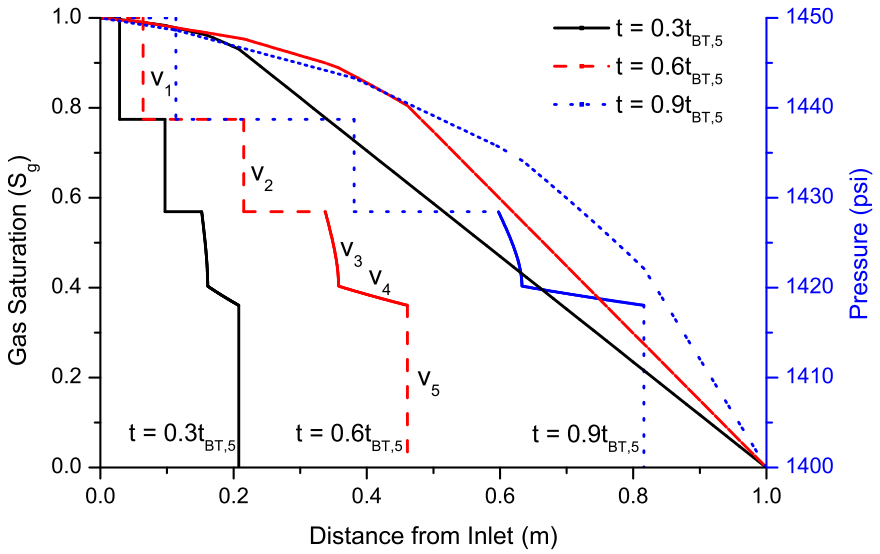

Figure 3.12: Pressure distribution along porous media for the four-component system (Case study 1)

For the sake of simplicity, in Case study 1, we first determine the pressure distribution along the constant state segment behind the shock wave v_1. The pressure value at the upstream of shock wave v_1 is assumed as the inlet pressure for the second constant state piece of the medium, between shock waves v_1 and v_2, and the pressure distribution is determined along this segment. This procedure is repeated until we reach to the rarefaction wave v_3. At this point, the pressure at the upstream of rarefaction wave v_3 is considered as the inlet and employing Equation 3.37, the pressure distribution is determined along rarefaction wave v_3. The same procedure is applied for rarefaction wave v_4, and again, Equation 3.36 is employed to determine the pressure profile ahead of the leading wave v_5. Equation 3.36 illustrates that in constant state zones, the pressure is a linear function of position x, and that the pressure decreases with a rate of $\frac{u_T(t)}{\lambda_T}$ when marching from inlet toward the outlet. This is more clearly shown in Figure 3.12. Figure 3.12 also indicates that the pressure drops more slowly at the single phase gas region, then it drops faster the two phase region and the sharpest pressure drop occurs along the single phase oil region for the three time spots shown; $t = 0.3t_{BT,5}$, $t = 0.6t_{BT,5}$, and $t = 0.9t_{BT,5}$. According to Equation 3.36, the pressure has an inverse relation with the total mobility, λ_T, which justifies the faster pressure drop at the single phase oil region with the lowest mobility. However, the pressure is directly proportional to the total velocity, $u_T(t)$. Thus, as shown in Figure 3.12, the pressure drop is faster in the single phase oil region at $t = 0.9t_{BT,5}$ than the $t = 0.6t_{BT,5}$ and $t = 0.3t_{BT,5}$, as the total velocity increases with time .

3.3.2 Case Study 2: Five-component Systems, A General Case at Practical Conditions

Case study 2 is a general case of n-component systems where the displacement happens at a reservoir pressure and temperature condition. The fluid compositions as well as porous media features are given in Table 3.3.

Table 3.3: Input parameters for the five-component system (Case study 2)

Component	**Composition (mole fraction)**				
	$\mathbf{N_2}$	$\mathbf{CO_2}$	$\mathbf{C_6}$	$\mathbf{C_{10}}$	$\mathbf{C_{16}}$
Synthetic Oil	0.000	0.000	0.200	0.500	0.300
Injection Gas	0.718	0.282	0.000	0.000	0.000

Parameter	**Value**
Oil Viscosity, μ_o (cP)	0.65447
Gas Viscosity, μ_g (cP)	0.02048
Viscosity Ratio, $M = \frac{\mu_o}{\mu_g}$	31.957
API Gravity, (^oAPI)	58.4
Displacement Length, L (m)	24.0
Porosity, ϕ	0.42
Absolute Permeability, K (D)	24.2
Inlet Pressure, p_{in} (psi)	537.5
Outlet Pressure, p_{out} (psi)	526.3
Average Pressure, p_{ave} (psi)	531.9
Constant Differential Pressure, Δp (psi)	11.2
Residual Oil Saturation, S_{or}	0.10
Connate Water Saturation, S_{wc}	0.00
Critical Gas Saturation, S_{gc}	0.00
Temperature, $T(^o\text{C})$	98.0

In this case, the injection of a two-component gas into a three-component synthetic oil is investigated. The injection gas contains 71.8 % CO_2 and 28.2 % N_2. The gas mixture is purchased from Praxair company (purity > 99.0 %). The synthetic oil contains 20.0 % C_6, 50.0 % C_{10}, and 30.0 % C_{16}. Pure components are purchased

from Sigma Aldrich company with a purity > 99.0 % to prepare the synthetic oil. The components are chosen in such way that we could have effective chromatographic separation of components and, therefore, distinct shock and rarefaction waves in the elementary wave solution. The displacement occurs at an average pressure of 531.9 psi and at a constant temperature of 98 ^{o}C. The pressure is kept at a moderate value for safety purposes, and the temperature is equal to a typical conventional oil reservoir. Fluid properties and the porous media features are taken from experiments discussed in Chapters 4 and 5, so as the analytical simulations could be replicated by experiments. The porous medium is one-dimensional and 24.0 meters long, with a porosity equal to 42 % and absolute permeability of 24.2 Darcy. The differential pressure between the inlet and the outlet is assumed to be 11.2 psi, and the residual oil saturation is $S_{or} = 0.1$. Peng-Robinson Equation of State (PR EOS) is applied to predict the phase behaviour of the fluids at the experiment condition.

3.3.2.1 Elementary Wave Solution

The global approach developed by Jessen et al. [26] is employed to determine the tie lines in this case study. This technique is based on the tie-line intersection approach initially introduced by Wang and Orr [61]. Wang and Orr [61] assumed that multi-component systems are fully self-sharpening, *i.e. all key tie-lines are connected by shocks*. Hence, key tie-lines can be identified by the fact that in fully self-sharpening systems, two adjacent key tie-lines must intersect. This is explained in details in Section 2.4.2.5. In five-component systems, four key tie-lines exist: initial oil tie-line, injection gas tie-line, and two crossover tie-lines. In order to show four key tie-lines in the compositional space, in a five-component system, a four-dimensional graph is

required which is not possible. However, Figure 3.13 shows the projection of key tie-lines in two-dimensional space along with a schematic solution of the problem.

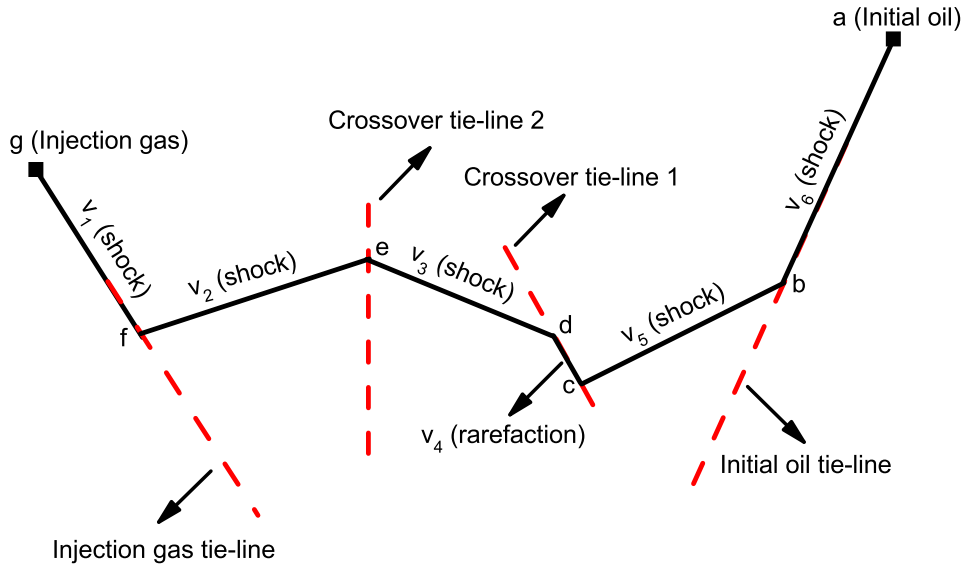

Figure 3.13: Schematic view of all tie-lines for the five-component system (Case study 2)

To obtain the exact solution, coding Peng-Robinson EOS in MATLAB software is used to calculate the equilibrium vapor and liquid compositions on key tie-lines. The gas and liquid equlibrium compositions, for the five-component system under study, are given in Table 3.4.

The exact elementary wave solution for this displacement is shown in Figure 3.14. Figure 3.14 shows the gas saturation, S_g, against the dimensionless velocity, $\frac{\xi}{\tau}$. The high volatility of gas components, N_2 and CO_2, with a high viscosity ratio, $M = \frac{\mu_o}{\mu_g} = 31.957$, results in a fast leading shock wave, v_6, (a-b). This leads to a large two phase region in porous media. However, no information of individual components can be directly extracted from Figure 3.14. Yet, the gas saturation values can be used to calculate the propagation velocity of fixed concentration of individual components

Table 3.4: Equilibrium liquid and vapor compositions along different tie-lines for the five-component system (Case study 2)

Tie-line	**Component**	$\mathbf{N_2}$	$\mathbf{CO_2}$	$\mathbf{C_6}$	$\mathbf{C_{10}}$	$\mathbf{C_{16}}$
Initial Oil	x_i	0.0565	0.0012	0.1878	0.4716	0.2829
Tie-line	y_i	0.9733	0.0052	0.0192	0.0023	0.0000
Crossover	x_i	0.0170	0.1679	0.1648	0.4067	0.2436
Tie-line 1	y_i	0.2744	0.7019	0.0206	0.0030	0.0000
Crossover	x_i	0.0174	0.1718	0.0000	0.5088	0.3019
Tie-line 2	y_i	0.2808	0.7156	0.0000	0.0036	0.0000
Injection Gas	x_i	0.0183	0.1733	0.0000	0.0000	0.8084
Tie-line	y_i	0.2820	0.7179	0.0000	0.0000	0.0001

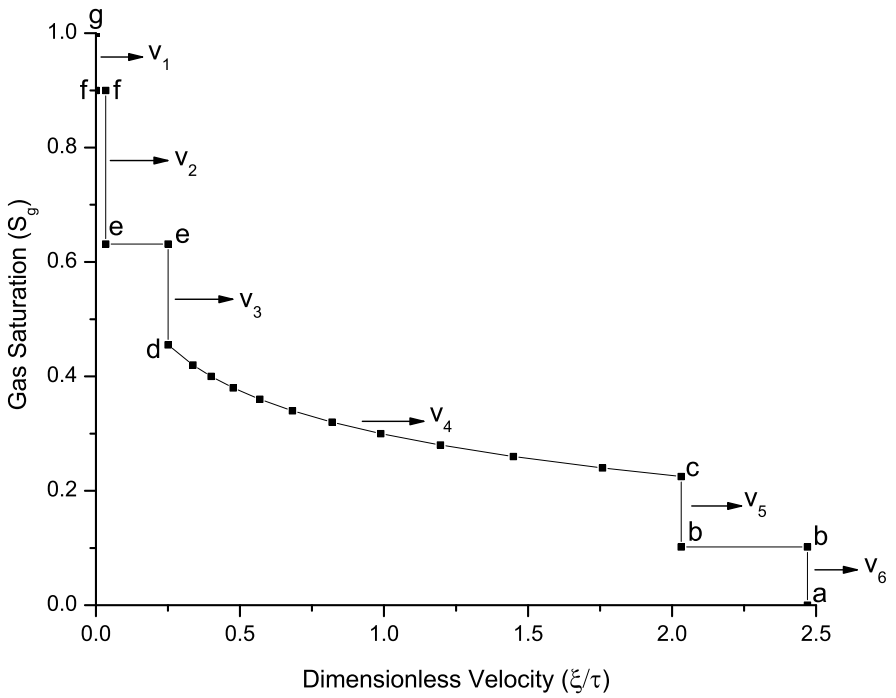

Figure 3.14: Elementary wave solution for gas/oil displacement for the five-component system (Case study 2)

in porous media. Figure 3.15 shows the individual components' profile against the dimensionless velocity. It represents the propagation velocity of fixed concentration of individual components.

As shown in Figures 3.14 and 3.15, the solution consists of five shock waves and one rarefaction wave that happens along the first crossover tie-line. Starting from the initial oil, the solution jumps into the two phase region by a shock wave v_6, (a-b). This shock wave is a bank of N_2 which is moving faster than all others towards the outlet. This is more clear from N_2 concentration profile in Figure 3.15, where between shock waves v_6 and v_5 (b-c), only N_2 component and synthetic oil components are present. According to Figure 3.14, the gas saturation at the upstream side of shock wave v_6 is $S_g = 0.1$, which indicates that the shock wave v_6 is pushing a small amount of the initial oil to the production well. The solution continues with a shock wave from the initial oil tie-line to the first crossover tie-line, v_5 (b-c). This is mainly a bank of CO_2 which comparing to N_2 has less preference to partition in vapor phase because it has a lower K-value. As shown in Figure 3.15, along shock wave v_5, the concentration of CO_2 increases from 0.0 at point b, to about 20 % at point c, while the concentration of other components decreases from point b to point c. The first crossover tie-line is the shortest tie-line in the system. Hence, there is a rarefaction on the first tie-line, wave v_4 (c-d) [45]. Figure 3.14 shows that although the gas saturation S_g increases almost 20 % from point c to point d, the propagation velocity of point d, almost 0.25, is significantly less than point c. This leads to a long rarefaction wave v_4 in Figure 3.14. This rarefaction ends with a semishock to the second crossover tie-line, v_3 (d-e). Figure 3.15 indicates that no C_6 is observed on the upstream side of the semishock v_3, which means that all the C_6 component present in the system is produced when

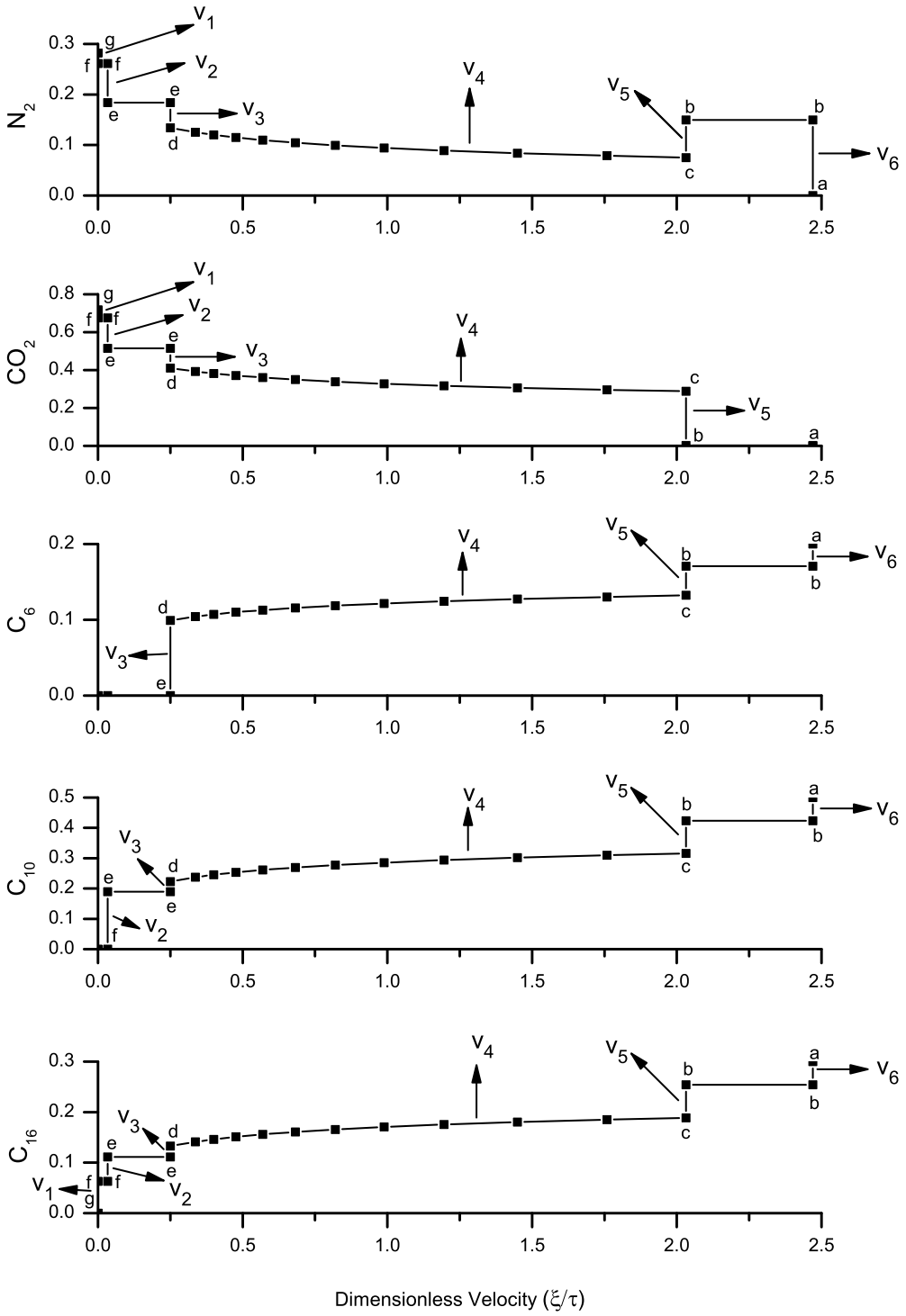

Figure 3.15: Composition profile for individual components for the five-component system (Case study 2)

the semishock v_3 reaches to the outlet. A genuine shock, v_2, then connects the second crossover tie-line to the injection tie-line (e-f). Figure 3.15 illustrates that on the upstream of shock v_2 no more C_{10} is present in the system. Although, all C_{10} is removed by the shock v_2, this shock has a very slow propagation velocity and it will take a very long time to reach to the outlet. From another point of view, almost 30 pore volumes of gas must be injected so that the shock v_2 reaches to the outlet and all C_{10} is fully produced. Finally, another genuine shock, v_1 (f-g), appears as the trailing shock in the system. This shock connects the point f on the injection tie-line and inside the two phase region to the injection point g. It has a very small velocity and carries infinitesimal amount of C_{16} in the vapor phase. This statement is consistent with the table 3.4, where the equilibrium vapor composition of C_{16} on the injection tie-line is equal to 0.0001. This shows that a very large amount of gas must be injected into the system to displace some amount of C_{16} out of the system. The elementary wave solution is justified using a similar approach presented in Orr [45].

3.3.2.2 Constant Pressure Boundary Solution

The procedure applied to Case study 1, is used to determine the total velocity and the breakthrough time of the elementary waves. Figure 3.16 shows the total velocity against the time along with the breakthrough of elementary waves.

Figure 3.16 indicates that unlike constant flux problems, the total velocity increases with time. As gas injection continues, a large volume of porous medium is occupied with gas. Gas has a higher mobility compared to oil, increases the total velocity over time. For this case the leading wave breaks through after 133 minutes of gas injection.

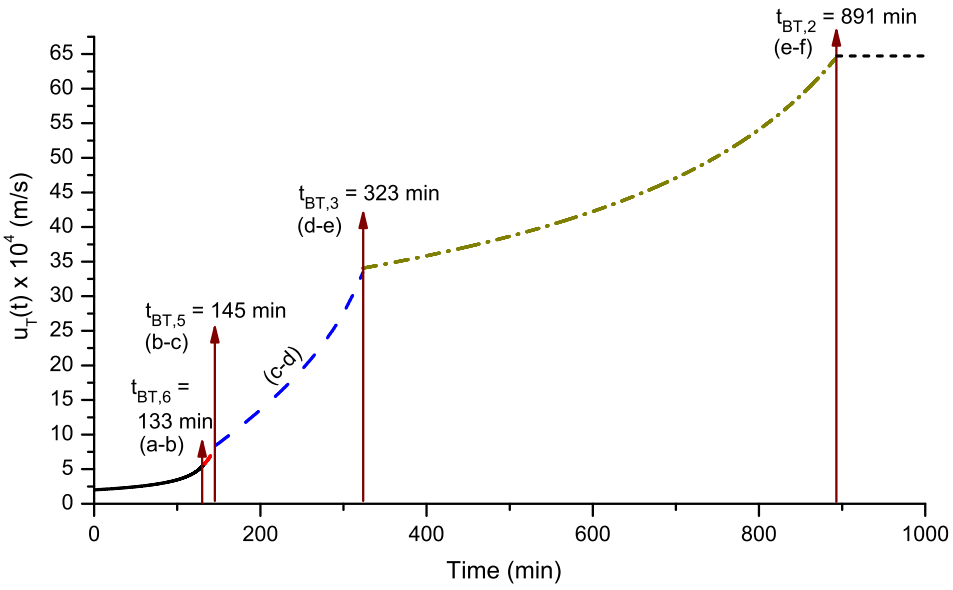

Figure 3.16: Total velocity profile as a function of time for the five-component system (Case study 2)

As presented in Figure 3.16, the total velocity increases gradually until the leading wave breaks through. Once the first wave breaks through, a continuous transition from inlet to the outlet exists for the gas and a high gas flow rate leads to a sharp increase in the total flow rate. Figure 3.16 indicates that the shock wave e-f is is the last wave that breaks through at 891 minutes. The trailing shock wave f-g, has a very small propagation velocity, therefore, it takes a very long time for this shock to reach the outlet. However, after the breakthrough of shock wave e-f, a single phase gas flows in porous media, with constant pressure boundaries. As depicted in Figure 3.16, this leads to a flow with a constant velocity.

3.3.3 Case Study 3: the Effect of Volume Change

In this case study, the same five-component system as Case study 2 is used to investigate the effect of volume change on gas/oil displacement with constant pressure boundaries. The volume change upon mixing changes the elementary wave solution and hence it adjusts the solution of the system with constant pressure boundaries. The composition of oil and gas phases, the fluid properties, and experimental and operating parameters are shown in Table 3.5.

Table 3.5: Input parameters for the five-component system (Case study 3)

Component	**Composition (mole fraction)**				
	N_2	**CO_2**	**C_6**	**C_{10}**	**C_{16}**
Synthetic Oil	0.000	0.000	0.200	0.500	0.300
Injection Gas	0.718	0.282	0.000	0.000	0.000

Parameter	**Value**
Oil Viscosity, μ_o (cP)	0.71083
Gas Viscosity, μ_g (cP)	0.02122
Viscosity Ratio, $M = \frac{\mu_o}{\mu_g}$	33.498
API Gravity, (^oAPI)	58.4
Displacement Length, L (m)	24
Porosity, ϕ	0.42
Absolute Permeability, K (D)	24.2
Inlet Pressure, p_{in} (psi)	939.7
Outlet Pressure, p_{out} (psi)	929.2
Average Pressure, p_{ave} (psi)	934.5
Constant Differential Pressure, Δp (psi)	10.5
Residual Oil Saturation, S_{or}	0.10
Connate Water Saturation, S_{wc}	0.00
Critical Gas Saturation, S_{gc}	0.00
Temperature, T (^{o}C)	98.0

As stated in Table 3.5, the average displacement pressure in Case study 3, is 934.5 psi which is higher than Case study 2. Increasing the average pressure changes the fluids'

properties and, therefore, the phase behaviour of the system. The most important parameter affected by increasing the pressure is the phase viscosities. Both of gas and oil viscosities increase with pressure. However, the viscosity ratio increases by 4.8 %. Yet, it is expected to have a lower viscosity ratio by further increase of pressure. By increasing the pressure, the effect of average pressure on displacement pressure is also examined. The differential pressure between the inlet and the outlet is 10.5 psi which is less than Case study 2, yet very close. In order to replicate the displacement in an experimental set up, all other experimental parameters such as porosity ϕ, absolute permeability K, temperature T, displacement length L, and initial fluid saturations are the same as Case study 2.

3.3.3.1 Elementary Wave Solution with No Volume Change upon Mixing

In this case, the results assuming no volume change upon mixing are presented first and then the effect of the volume change is investigated. Increasing the average pressure in Case study 3 compared to Case study 2, squeezes the two-phase region and changes the equilibrium vapor and liquid compositions on the key tie-lines. Yet, the relative direction of key tie-lines does not change as the same components are still present in the system and therefore, the overall shape of the solution remains the same. Still, the propagation velocity of elementary waves reduces with increasing pressure. Figure 3.17 shows a schematic projection of key tie-lines in a two-dimensional space. As indicated in Figure 3.17, the solution structure remains the same, five shock waves and one rarefaction wave along crossover tie-line 1 construct the solution, but the wave velocities are affected by the pressure. The exact elementary wave solution is shown in Figure 3.18.

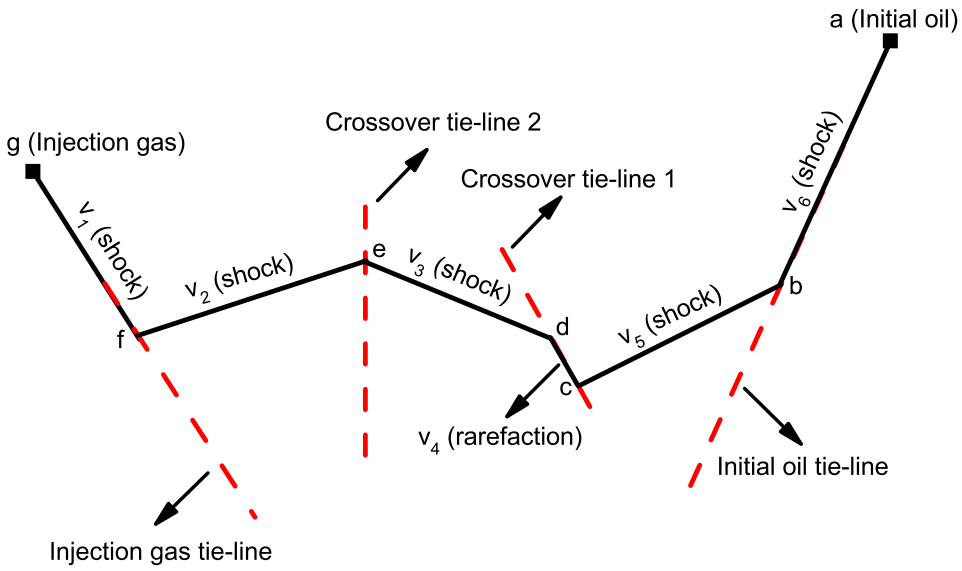

Figure 3.17: Schematic view of all tie-lines for the five-component system (Case study 3)

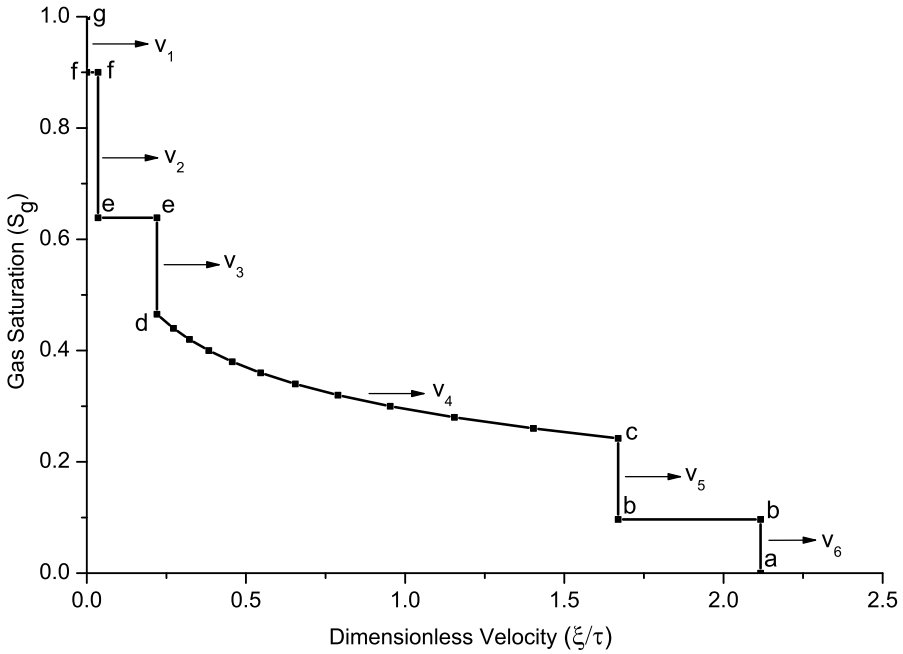

Figure 3.18: Elementary wave solution for gas/oil displacement for the five-component system with no volume change upon mixing (Case study 3)

Figure 3.18 shows the gas saturation S_g versus dimensionless velocity $\frac{\xi}{\tau}$. As expected, the general solution structure is very similar to the Case study 2, since the same components are present in both cases. But, increasing the pressure, has decelerated the leading waves. This will delay the breakthrough time of the leading wave and increase the recovery factor comparing to the lower pressure in previous case.

Like Case study 2, the gas saturation profile in Figure 3.18 gives the overall wave structure and the propagation velocity of elementray waves, but no information of individual components. Figure 3.18 shows that the leading shock wave v_6, (a-b) slows down by increasing the pressure. Slower leading shock wave, postpones the breakthrough time compared to Case study 2, and in turn, it increases the recovery factor. The gas saturation profile in Figure 3.18 can be used to determine the individual components' profile versus the dimensionless velocity. Figure 3.19 presents the propagation velocity of fixed concentrations of individual component in Case study 3.

Figures 3.20 and 3.21 show the effect of pressure on displacement process. These figures indicate that the elementary wave solution has not made a significant change from Case study 2 to Case study 3 with increasing the pressure. The most important change, however, is the propagation velocity of the leaving shock wave v_6, which slows down by increasing pressure. A precise investigation of trailing waves also indicates that the trailing shock v_2 (e-f) speeds up with increasing pressure. This is the result of slightly higher solubility of the heavier components in the gas phase at the higher pressure. The increment in trailing shock velocity is not noticeable in Figures 3.20 and 3.21. Yet, the incremental trailing shock velocity will be more noticeable at

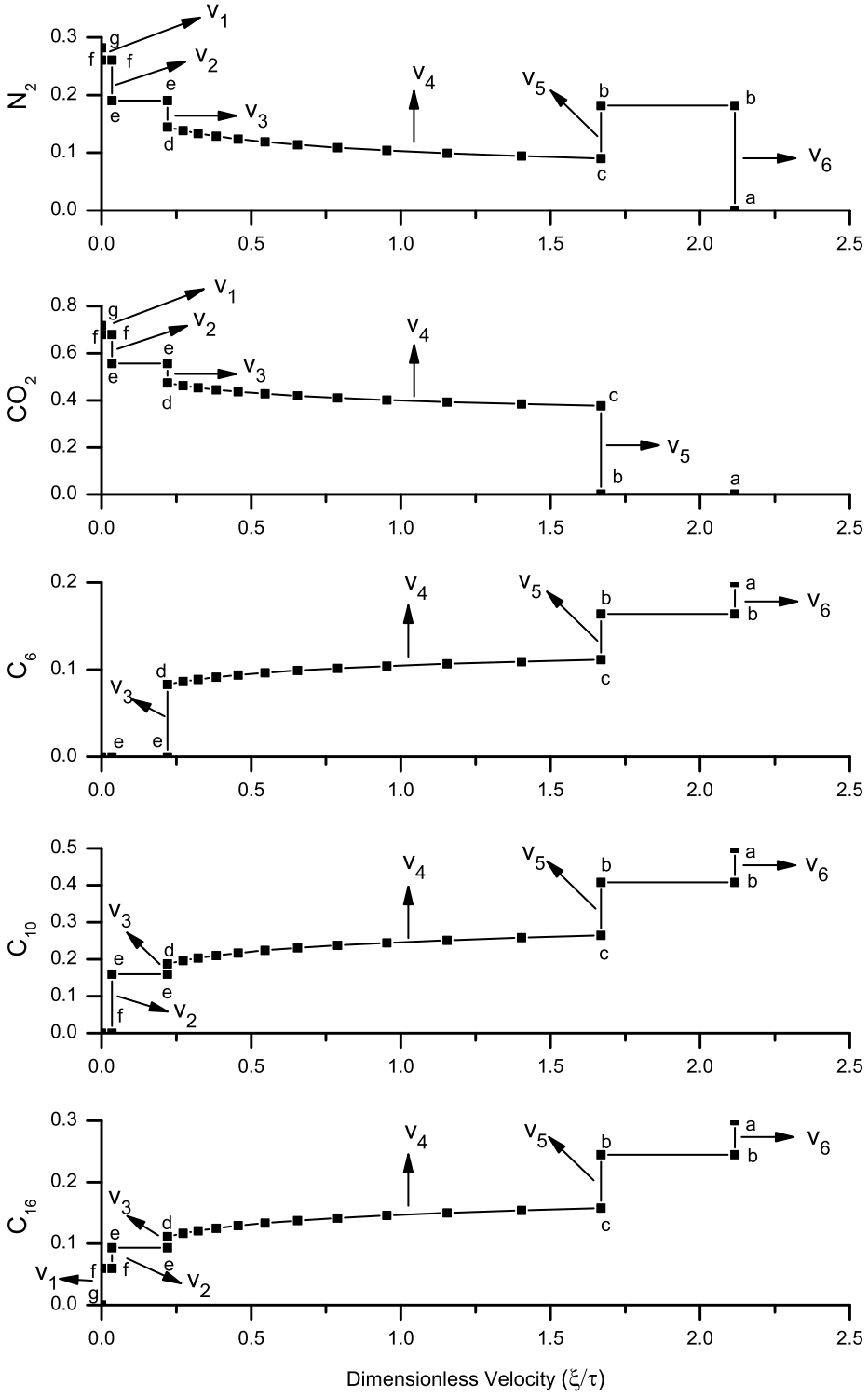

Figure 3.19: Component composition profile for five-component system with no volume change upon mixing (Case study 3)

higher pressure. Figure 3.21 also indicates that the leading N_2 and CO_2 bank have higher concentrations in Case study 3. Therefore, by increasing the pressure, a higher oil recovery can be achieved at gas breakthrough time in Case study 3.

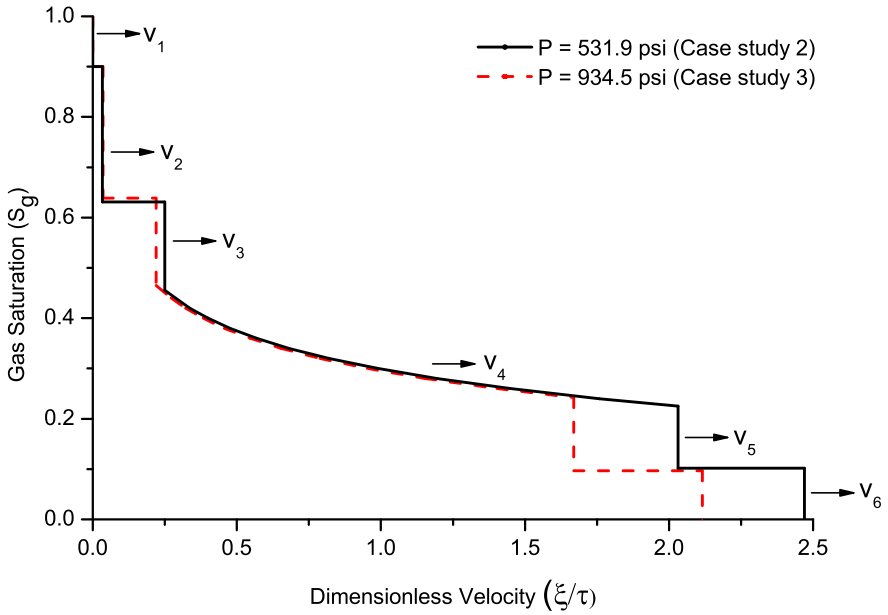

Figure 3.20: Comparison of Case studies 2 and 3 for effect of pressure on gas saturation profile

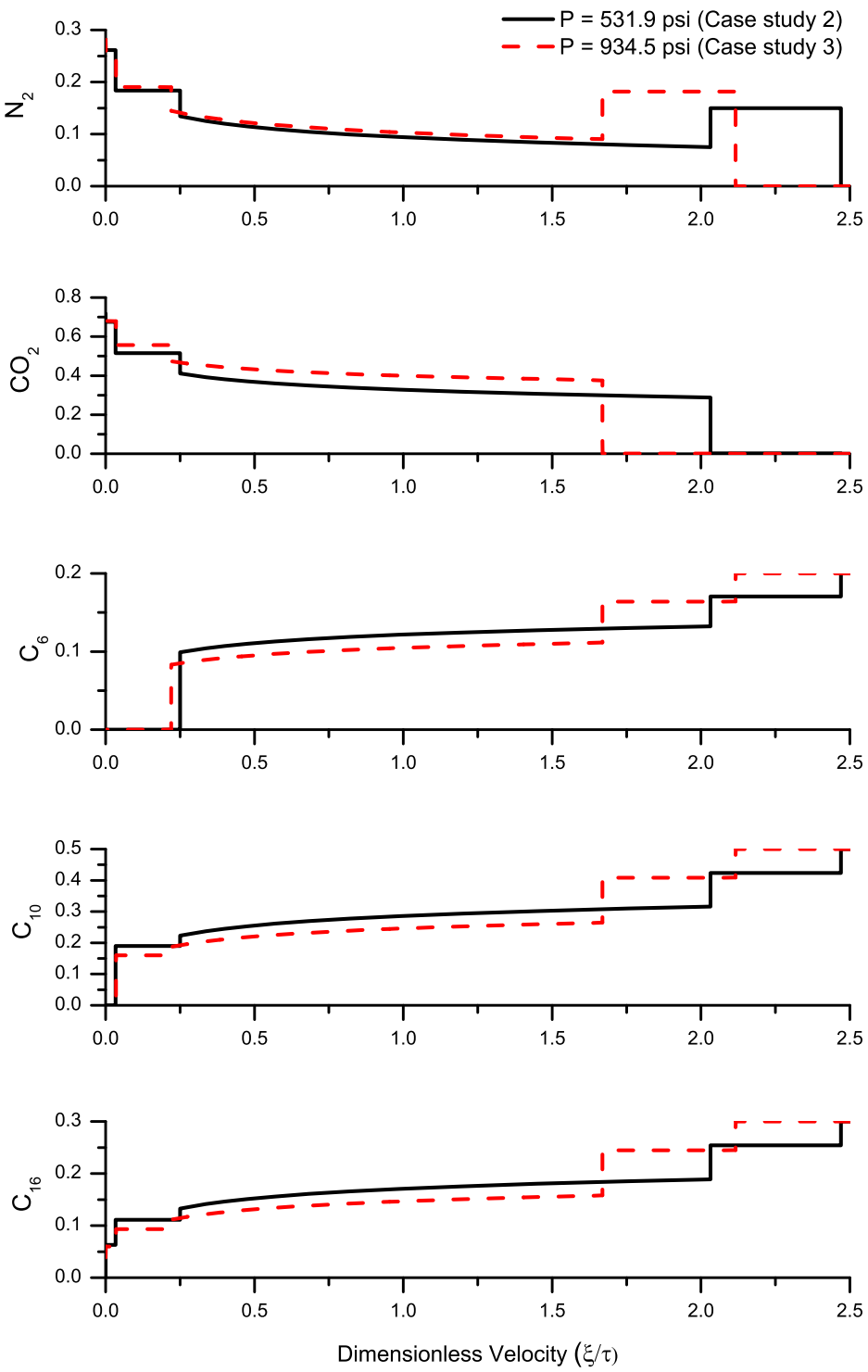

Figure 3.21: Comparison of Case studies 2 and 3 for effect of pressure on component composition profiles

3.3.3.2 Constant Pressure Boundary Solution with No Volume Change upon Mixing

Figure 3.22 illustrates the total velocity against time.

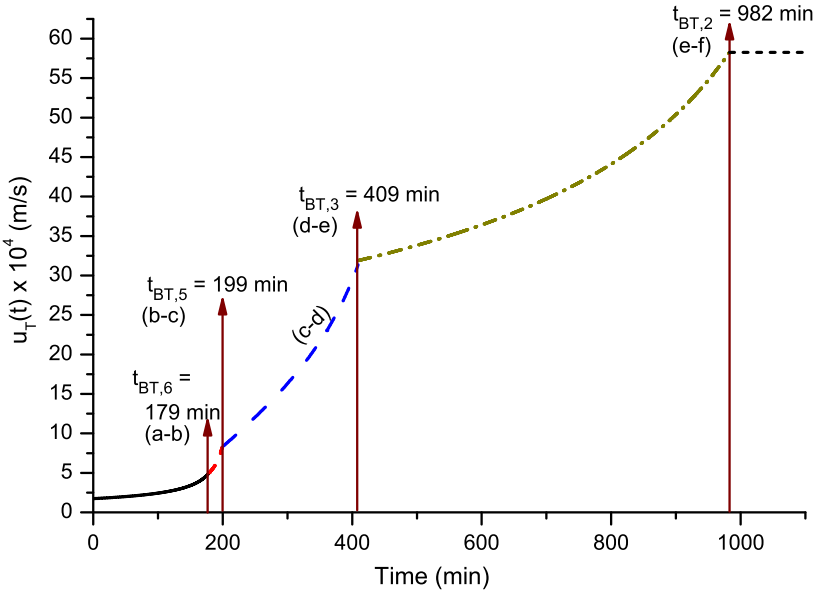

Figure 3.22: Total velocity as a function of time with no volume change upon mixing for the five-component system (Case study 3)

The breakthrough time in this case is determined to be 179 minutes after starting the gas injection. Compared to Case study 2, the gas breakthrough time is delayed by 46 minutes. This delay in gas breakthrough time is mainly because of increasing the average pressure which slows down the leading shock wave a-b. As shown in Figure 3.22 the trailing shock wave e-f, also breaks through with 90 minutes delay, compared to Case study 2. yet, the overall shape of total velocity profile versus the time remains unchanged.

3.3.3.3 Displacement with Volume Change upon Mixing

Both in this case and Case study 2, it is the same components and temperature but the average displacement pressure is lower in Case study 2. In both cases it was assumed that all the components occupy the same volume when they are in gas and liquid phases, *i.e. they do not change volume as they transfer from one phase to another*. In reality, gas components occupy more volume when they are in gas phase, especially at low and moderate pressures. When the components change volume as they transfer between the phases, the local flow rate or the dimensionless flow rate is no longer a constant and it changes across the shocks. In such a case the Riemann problem 2.17 is converted to,

$$\begin{aligned}
&\frac{\partial G_i}{\partial \tau} + \frac{\partial H_i}{\partial \xi} = 0 \qquad ; && && i = 1, ..., n_c, \\
&G_i(0, \tau) = G_i^{inj} \qquad ; && x \leq 0 \qquad ; && i = 1, ..., n_c, \\
&G_i(\xi, 0) = G_i^{init} \qquad ; && x > 0 \qquad ; && i = 1, ..., n_c.
\end{aligned} \tag{3.38}$$

In the set of Equations 3.38, G_i is the overall molar concentration of component i (moles per unit volume) and H_i is the overall molar flux of component i(mole per unit area and time). Comparing set of Equations 3.38 with 2.17, the overall volume fraction of component i, C_i, and overall fractional volumetric flow of component i, F_i, in no volume change Equations 2.17, have changed to overall molar concentration of component i, G_i, and overall molar flux of component i, H_i, in volume change Equations 3.38, respectively. Furthermore, the number of equations has increased by 1, since the local velocity v_D is unknown, in the new set of Equations 3.38. G_i and

H_i can be calculated from the following equations,

$$G_i = c_{i1}\rho_{1D}S + c_{i2}\rho_{2D}\,(1-S) \qquad ; \qquad i = 1, ..., n_c,$$

$$H_i = v_D(c_{i1}\rho_{1D}f + c_{i2}\rho_{2D}\,(1-f)) \quad ; \qquad i = 1, ..., n_c. \tag{3.39}$$

However, the elementary wave velocity is equal to the wave velocity when no volume change happens upon mixing times the local velocity [45],

$$\frac{dG_i}{dH_i} = v_D \frac{df_1}{dS_1} \tag{3.40}$$

Figure 3.23 presents the gas saturation profile when the volume change is considered, in Case study 3.

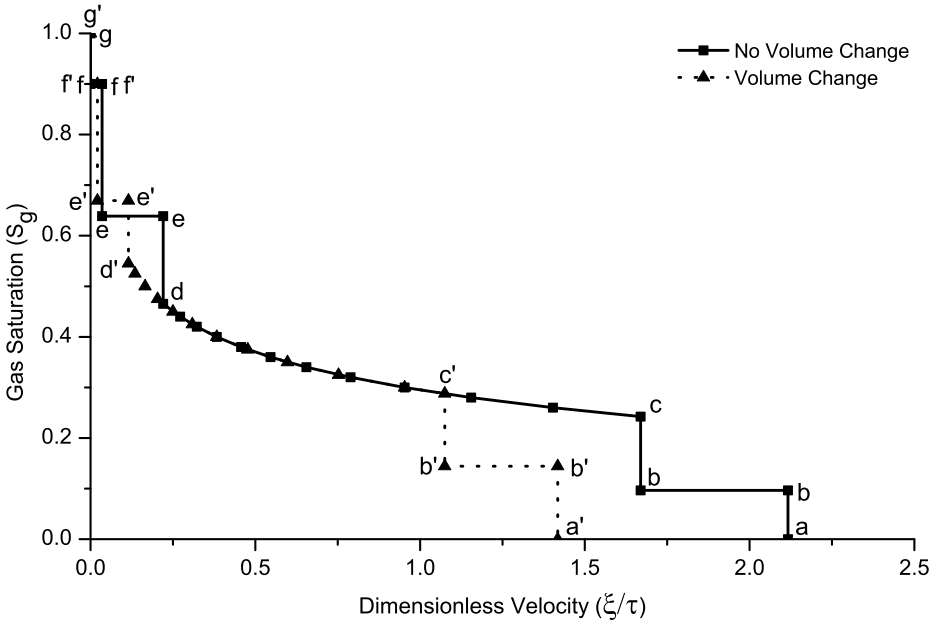

Figure 3.23: The effect of volume change on the elementary wave solution for the five-component system (Case study 3)

Figure 3.23 shows that volume change has a remarkable effect on the elementary wave solution. The volume change substantially affects the propagation velocity of leading waves by slowing down shock waves a-b and b-c. The trailing waves are affeted less by the volume change. The considerable changes in the leading wave velocities occur because CO_2 and N_2 occupy much less volume when they are dissolved in the liquid phase than they do in the vapor phase [11]. When CO_2 and N_2 saturate the synthetic oil in the two-phase region, a significant volume of vapor phase is lost as it goes into the liquid phase, and therefore, waves slow down. Changing the elementary wave solution alters the total velocity profile accordingly. Figure 3.24 shows the effect of volume change on the total velocity.

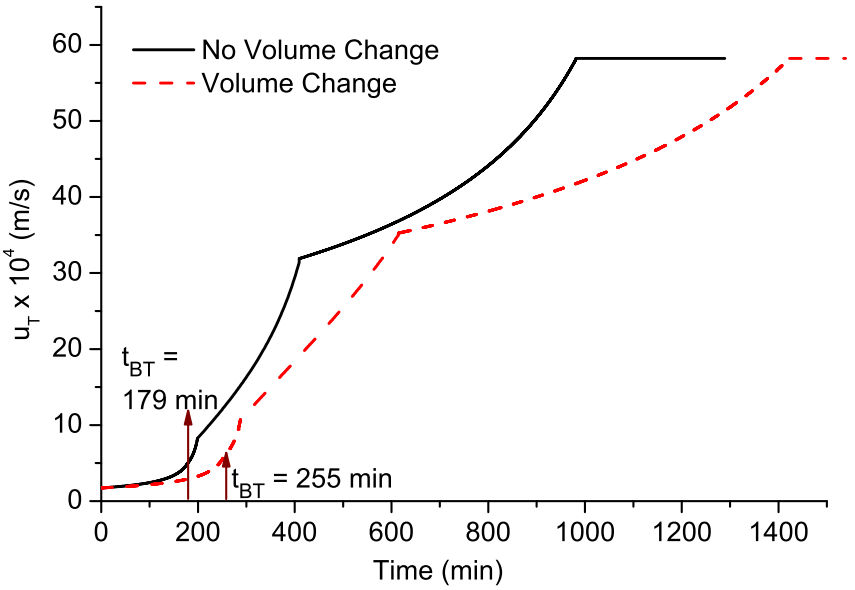

Figure 3.24: The effect of volume change on the total velocity for the five-component system (Case study 3)

Figure 3.24 illustrates the effect of volume change on the total velocity. As shown

in figure 3.24 Considering the volume change upon mixing increases the gas breakthrough time from 179 minutes to 255 minutes. As mentioned above, this is because of dissolution of N_2 and CO_2 in the oil phase and loss of the gas volume. The solubility of injection gas in the initial oil is a decisive factor on the effect of volume change on the displacement process. The effect of volume change upon mixing becomes more important when the CO_2 concentration in the injection gas increases, as CO_2 has a high solubility in the oil. On the other hand, N_2 has a low solubility in the oil, therefore the displacement process becomes less affected by the volume change when the N_2 concentration increases in the injection gas. In Case study 3, the injection gas contains 28.2 % N_2 and 71.8 % CO_2. The gas breakthrough time is shown in Figure 3.24 with and without volume change. The breakthrough time is under estimated by 29.8 % error when the volume change is not considered in the calculations.

3.4 Analytical Calculation of the Minimum Miscibility Pressure

In this section the methodology developed by Jessen et al. [26] is applied to calculate the MMP of the five-component system discussed in case studies 2 and 3. In this system, four key tie-lines exist; initial oil tie-line, injection gas tie-line and two crossover tie-lines. However, in order to solve the set of equations in 2.45 a fairly accurate initial guess is required for the unknown parameters x_i^j, y_i^j, α_j, β_j, β_{oil}, and β_{inj}. Following the strategy suggested in [25] 2.45 is solved. At the first step, using negative flash calculations and tie-line intersection approach in [61] all the key tie-lines are found

at a low pressure, assuming a pure CO_2 is displacing the three-component synthetic oil. Then, at the current low pressure, the injection gas composition is adjusted to the desired injection gas composition by the following equation,

$$z_{inj} = (1-\theta) z_{inj}^{pure} + \theta z_{inj}^{actual} \tag{3.41}$$

In Equation 3.41, z_{inj} is the injection gas composition which is being adjusted to the actual gas composition, θ is the adjusting parameter where, $0 \leq \theta \leq 1$, z_{inj}^{pure} is the pure gas composition which in this case corresponds to 100 % CO_2, and z_{inj}^{actual} is the actual or the interested gas composition. However, a low value like 0.01 is chosen for θ and the injection gas is adjusted a little closer to the actual injection gas composition and the key tie-line coordinates from the first step are used as the initial guess for the set of Equations 2.45. Now, 2.45 is solved for the new injection gas composition. Afterwards, a larger value is chosen for θ and solution from the previous θ is used as the initial guess. Likewise, the procedure is repeated and the θ becomes larger and larger until $\theta = 1$. So far, all the calculations are performed at the low pressure. Once the θ is equal to 1, i.e. the injection gas composition is equal to the desired composition, the length of key tie-lines are calculated from Equation 2.41. If none of the tie-lines has zero length, the pressure is increased by 10 psi and the calculations are repeated until we reach the MMP in which which one the tie-lines has zero length. Figure 3.25 shows the tie-line length versus pressure for the gas/oil system studied in Case studies 2 and 3 at 98 ^oC.

Figure 3.25 indicates that the crossover tie-line 1 is the shortest key tie-line in the system and controls the miscibility. By increasing the pressure, the two-phase region

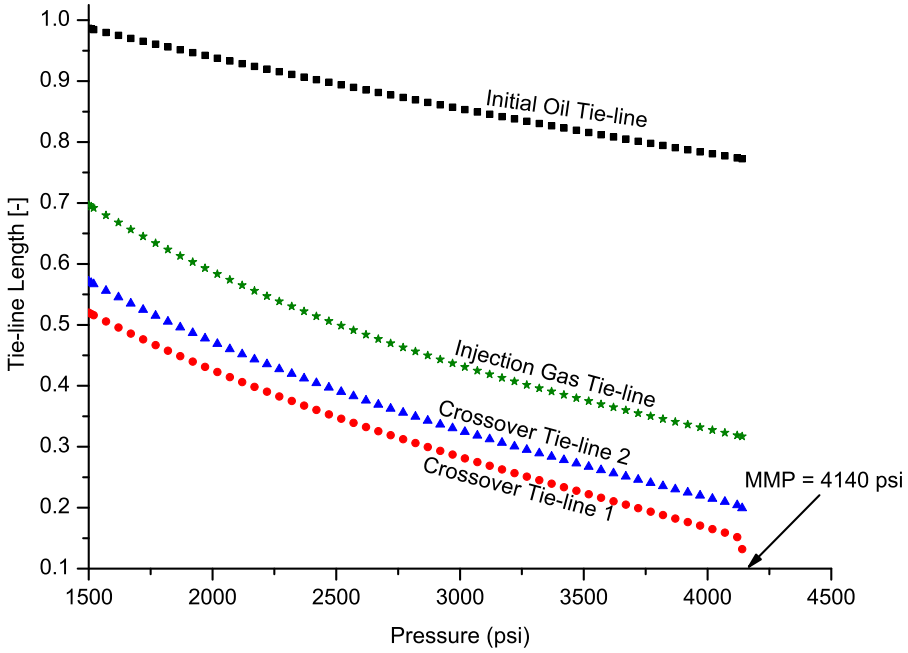

Figure 3.25: Tie-line length against pressure for the five-component system

gets smaller and and the length key of tie-lines decreases. By definition, the minimum pressure at which one of the key tie-line becomes the critical tie-line, is the minimum miscibility pressure. However, as shown in Figure 3.25, in the specific system studied in Case studies 2 and 3, tie-line calculations fail at 4140 psi, where the crossover tie-line 1 has a length of 0.1. The reason is the difficulties of phase behaviour calculation near the critical point. According to Figure 3.25, the estimated MMP for this system is 4140 psi. Controlling the miscibility by crossover tie-line 1 illustrates that the miscibility mechanism is a combined condensing/vaporizing drive, rather than pure vaporizing or pure condensing.

3.5 Discussion

In this chapter, a novel analytical approach is presented to investigate the displacement mechanism in a porous media with constant pressure boundaries. It is explained that when the injection pressure and production pressures are constant, the total volumetric flux is a function of time only, in incompressible systems. Determination of total flux and breakthrough time of elementary waves is described. Construction of elementary wave solution is spelled out and it is explained how this solution is used to derive the total flux and breakthrough time of elementary waves. In order to further clarify the analytical solution for multi-component gas/oil displacement with constant pressure boundaries, three case studies are investigated in this chapter. The elementary wave solution was first obtained in all cases and then using the developed analytical method, the total velocity and breakthrough times of elementary waves were found for the corresponding cases with constant pressure boundaries. Case study 1 is a four-component system with constant K-values. This is a simple hypothetical system for clarifying the procedure. In Case study 2, a more practical situation was examined. This includes a five-component system at a moderate pressure and high temperature assuming no volume chnge upon mixing. Peng-Robinson EOS was applied to predict the phase behaviour and to determine the geometry of the tie-lines. However, the total velocity was determined as a function of time and the breakthrough of elementary waves were obtained successfully using the analytical approach. Case study 3, was a more advanced version of Case study 2. In Case study 3, the volume change upon mixing was considered and the effect of volume change on the results were investigated. Volume change alters the elementary wave solution and

accordingly, the breakthrough time and the total velocity profile. The total velocity and the breakthrough times of elementary waves were obtained successfully for this case and the results indicated that the volume change has a considerable effect on the results. Case studies 2 and 3 are designed in such a way that they could be replicated in the lab via slim tube experiments. Finally, in Section 3.4, the MMP of the gas/oil system studied in Case studies 2 and 3 is determined using the analytical method developed by Jessen et al. [26]. In their method, tie-line calculations sometimes fail near the critical point. The accuracy of this method is further examined by slim tube experiments in Chapter 4. However, in some cases, like the one studied here, the phase behaviour calculations fail when approaching the miscibility pressure, and it becomes difficult to determine the exact pressure at which miscibility is achieved.

Chapter 4

Miscibility Experiments

Mathematical approaches to solving real world problems have always been controversial whether they can fully capture the reality or not. On the other hand, to validate the mathematical approaches, an experimental set up is required that meets the main assumptions of the mathematical model. Two main assumptions in the mathematical description of the gas/oil displacement problems include: (1) one-dimensional flow, and (2) dispersion-free system. These assumptions are hardly met in core flood experiments as the core's large diameter and small length are limiting factors for the one-dimensional flow and dispersion-free systems, respectively. Instead, in order to confirm the analytical model developed in Chapter 3 and validate the assumptions made in the derivation of the model, slim tube experiments are designed to replicate Case studies 2 and 3, experimentally. The long length of the slim tube leads to a large Peclet number which is an indication of low dispersion effects. The length of the slim tube along with a small inner diameter provides a one-dimensional flow rate. As stated in Case studies 2 and 3, to reduce the uncertainties in the characterization

of the initial in place oil a three component synthetic oil was used (20%C_6, 50%C_{10}, and 30%C_{16}). Individual components were purchased from Sigma Aldrich company and were mixed to create a synthetic oil with a desired composition. This reduces the errors in the analytical solution. The two component injection gas (71.8%CO_2 and 28.2%N_2) was purchased from Praxair. The oil and gas compositions are chosen so that the miscibility is achieved at a moderate pressure. To investigate the accuracy of Jessen's method in calculating the MMP [25], the experimental procedure on conducting constant flow rate slim tube tests on the five-component system is explained and the results are interpreted in this chapter.

4.1 Experimental Set up

A schematic view of slim tube set up with its important parts is shown in Figure 4.1.

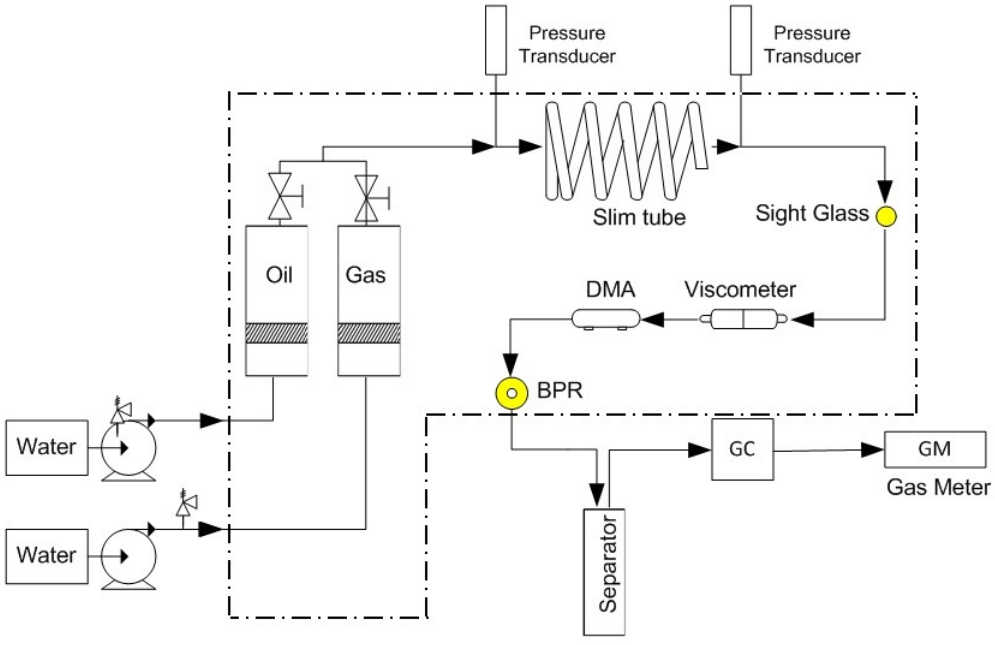

Figure 4.1: Schematic view of the slim tube set up

As indicated in the figure, the main components of the set up can be listed as following,

a) **5K and 20K Quizix pumps:** 5K and 20K Quizix pumps by Chandler Engineering are installed on the set up. These accurate pumps can operate at constant flow rate and constant pressure modes. 5K and 20K Quizix pumps can operate at pressures up to 5000 psi and 20,000 psi and have a maximum flow rate of 15 mL/min and 7.5 mL/min, respectively. These pumps have a resolution of 0.1 and 0.0001 in the pressure and flow rate, respectively.

b) **High pressure gas and liquid accumulators:** High pressure accumulators, manufactured by Craig Instruments, are employed to store the gas and the oil in the oven, where the oil can be used to saturate the slim tube and the gas can be used as the injection gas. The gas and liquid accumulators have 2 liter capacities and withstand pressures up to 10,000 psi.

c) **Needle valves:** Two-way and three-way needle valves isolate the different parts of the set up and tubing. The working pressure for these needle valves is up to 15,000 psi and are manufactured by Autoclave Engineering.

d) **High pressure tubing:** Hastelloy 1/8" tubing which can withstand up to 15,000 psi pressure are installed to ensure safe experiments.

e) **Pressure transducers:** Pressure transducers accurately measure the pressure at different points in the set up. Pressure transducers are manufactured by Paro Scientific and have accuracy of 0.0001 psi. Two standard pressure transducers calibrated by Paro Scientific were used for the calibration of the other transducers in the set up.

f) **Slim tube:** A 24 meter slim tube made by Vinci Technologies mimics the reservoir condition and creates multiple contacts between initial oil and injection gas. 3/8" OD and 0.245" ID hastelloy slim tube can withstand up to 10,000 psi pressure. The slim

tube was filled with $230 - 310\,\mu m$ silica particles and packed by the Vinci Technologies.

g) **Sight glass:** Sight glass is installed right after the slim tube and is used to record the breakthrough time precisely. It also provides visual observation of miscibility when real crude oil is used in the system. The sight glass is manufactured by Vinci Technologies and its working pressure is to 10,000 psi.

h) **High pressure and high temperature viscometer:** this is an inline device which enables us to measure the effluent viscosity at experiment condition. This inline viscometer is manufactured by Hydro Motion and has a resolution of 0.1 cP. The viscometer was calibrated using DI water, toluene, and acetone where the viscosity of these fluids were also measured in a Cambridge viscometer.

i) **DMA densitometer**: Anton Paar DMA densiometer measures the density of effluent which is an important parameter in detection of MMP. This densiometer has accuracy of 0.01 $\frac{Kg}{m^3}$. DMA densitometer was calibrated using DI water, toluene and acetone.

j) **Back pressure regulator:** Keeps the pressure constant at the outlet of slim tube. This is made by Vinci Technologies and its maximum allowable working pressure is to 10,000 psi.

k) **Two phase separator:** A separatory funnel is installed outside of the oven in which the effluent is separated into two phases, the gas is directed to the gas meter and the micro GC and the oil is collected for recovery calculations and composition analysis.

l) **Inline micro GC:** The inline Agilent micro GC analyzes the composition of the outlet gas. The inline micro GC was calibrated using a hydrocarbon gas sample pro-

vided by Agilent technologies

m) **Gas meter:** This is the last part of the set up that measures the gas volume at the standard condition. MK 2000 is manufactured by Emdyne Inc has a resolution of 0.1 cc in reading gas volume accumulated in the gasmeter. The gas meter was calibrated by injecting known volumes of air into the device using a syringe.

n) **Gas Chromatography (GC):** The oil phase collected in the separator is analyzed by the Agilent Gas Chromatography 7890a. The capillary column used in the GC is manufactured by Restek Corporation. This is 15 m long, has a inner diameter of 0.25 mm and the thickness of the coating phase inside the column is 0.10 μm. The GC was calibrated using a calibration sample with known composition, provided by Agilent technologies.

4.2 Experimental Set up Characterization and Measurements

Slim tube properties and set up features are important parameters to perform reliable experiments and analytical simulations. In this section, the main features of the slim tube set up are determined using simple experiments.

4.2.1 Pore Volume and Porosity

In order to calculate the pore volume and the porosity of the slim tube, the inlet and the outlet of the tube are disconnected from the set up. To keep the accuracy, the inlet is directly connected to a pump and the outlet is attached to a transparent

tube and the transparent tube to a collecting vessel. 3-4 pore volumes of toluene with an injection rate of 3.0 cc/min is injected into the tube and injection continues until no bubble is observed in the transparent tube. By measuring the volume of toluene collected in the vessel, the pore volume and the porosity of the slim tube is calculated from the Equations 4.2.1,

$$PV = V_{inj} - V_{Produced} \tag{4.1}$$

$$\phi = \frac{PV}{V_{bulk}} \tag{4.2}$$

The pore volume of the slim tube is denoted as PV, V_{inj} is the volume of injected toluene, $V_{Produced}$ is the volume of produced toluene which includes the toluene left inside the transparent tube, ϕ is the porosity, and V_{bulk} is the bulk volume of the slim tube. Applying Equations and 4.2.1, the PV and the porosity are calculated as,

$$PV = 1152.7 - 841.9 = 310.8cc \tag{4.3}$$

$$\phi = \frac{310.8}{740} = 42\% \tag{4.4}$$

4.2.2 Dead Volume

From the slim tube outlet to the separator, there is a dead volume associated with valves, tubing, and the volume of inline equipment. To have more accurate recovery factor values, the dead volume must be calculated and deducted from volume of produced oil at the end of each test. To calculate the dead volume, the outlet of slim tube is disconnected from the system first and the slim tube is saturated. Then, the

slim tube is connected to the tubing and Toluene is injected until the tubing, valves and inline equipment are filled. The dead volume is then calculated from an equation similar to 4.2.1, where PV is replaced with V_{dead}.

$$V_{dead} = V_{inj} - V_{Produced} \tag{4.5}$$

For the current set up,

$$V_{dead} = 78.9 - 57.9 = 21cc \tag{4.6}$$

4.2.3 Absolute Permeability Measurement

The absolute permeability of the slim tube is required to perform one-dimensional simulations. Prior to the MMP experiments, the absolute permeability of the tube is calculated by flowing toluene through the slim tube at four different flow rates. The slim tube is first saturated by injection of 3 pore volumes of toluene. Then, the injection of toluene continues at four different flow rates, the flow rates are chosen to be all less than 1 cc/min to ensure a laminar flow in the slim tube. At each flow rate the injection continues until a stabilized flow is achieved, i.e. constant inlet and outlet pressures are observed at each flow rate. The inlet and outlet pressures are measured by pressure transducers and then the absolute permeability is calculated by Darcy's law. Table 4.1 shows the data recorded for measuring the absolute permeability.

Table 4.1: Absolute permeability measurement for the slim tube

Flow Rate (ml/min)	$\mathbf{p_{in}}$ **(psi)**	$\mathbf{p_{out}}$ **(psi)**	$\mathbf{\Delta p}$ **(psi)**	**K (D)**
0.3	28.7	14.7	14.0	23.8
0.5	37.2	14.7	22.5	24.7
0.7	45.9	14.7	31.2	24.9
0.9	57.4	14.7	42.7	23.4

An example of absolute permeability calculation is given below,

$$Q = 0.3\frac{ml}{min}: \quad Q = -\frac{KA}{\mu}\frac{\partial p}{\partial x} \Rightarrow K = -\frac{Q\mu\partial x}{A\partial p}$$

$$\Rightarrow K = -\frac{0.3\frac{ml}{min}\frac{1\,min}{60\,sec} \times 0.575\,cP \times 2400\,cm}{0.3042\,cm^2 \times 14.0\,psi\frac{1\,atm}{14.7\,psi}} \Rightarrow K = 23.8\,D \quad (4.7)$$

Figure 4.2 shows the liquid permeability at four different flow rates.

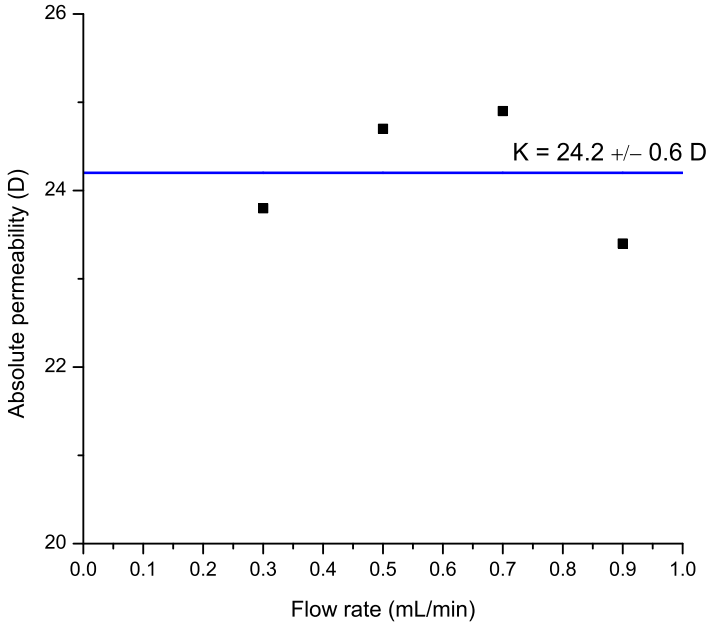

Figure 4.2: Absolute permeability measurement for the slim tube

The absolute permeability of the tube is considered to be the arithmetic average of four data points shown in Figure 4.2. However, a summary of the set up features are provided in Table 4.2.

Table 4.2: Slim tube set up features

Parameter	**Value**
Length, L	24.00 m
Outer Diameter, OD	9.52 mm
Inner Diameter, ID	6.22 mm
Dead Volume	21.0 cc
Pore Volume, PV	310.8 cc
Porosity, ϕ	0.42
Absolute Permeability, K	24.2 D
Porous Media	$230 - 310\,\mu m$ silica

4.3 Minimum Miscibility Pressure Tests

Prior to the test, the set up should first be prepared. The slim tube must be cleaned first. Toluene is an appropriate solvent to wash the tube. Two pore volume of toluene is normally enough for cleaning. Two pore volumes of Nitrogen is then injected to displaces the toluene from the tube. Since the boiling point of toluene is 110.6 ^oC, increasing the oven temperature to 150 ^oC removes the rest of the toluene and dries the tube automatically. Then the oil accumulator is filled with three pore volumes of the synthetic oil and is injected into the slim tube by a flow rate in the range of of 2-4 cc/min. Experience has shown that injecting two pore volumes of synthetic oil will fully saturate the slim tube. However, the synthetic oil injection is continued until no bubbles are observed at the outlet. The saturation procedure is performed

at atmospheric pressure. The back pressure regulator is then charged to the test pressure. Afterwards, the gas accumulator is filled with the injection gas. A gas booster might be required to fill the accumulator to a certain pressure. Now, the oven is turned on to increase the temperature to the reservoir temperature. By increasing the temperature, the pressure of the oil in the slim tube and the gas in the accumulator will automatically increase. If the gas pressure in the accumulator is still less than the test pressure, water is injected to the bottom of accumulator to increase the pressure by decreasing the gas volume. The gas pressure and the slim tube pressure must be equal to the test pressure at the beginning of the test. Now, the apparatus is ready for conducting the test. The experiment starts by injecting the gas at 0.12 PV/hr. While the injection rate is kept constant at the inlet, the pressure is fixed by a back pressure regulator at the outlet. However, the density of the effluent is continuously monitored by the inline DMA device, and it is separated into two phases at the separator, when exits from the oven. The gas is analyzed by the inline micro GC, and the volume of oil collected in the separator is recorded to calculate the recovery factor. Oil samples, are also taken to a GC for compositional analysis. The gas injection has been continued until 1.2 PV of gas is injected into the slim tube.

4.4 Experimental Results

Seven experiments are conducted at seven different pressures. 1.2 PV of gas is injected into the slim tube at each test. The most important parameters recorded during the tests are recovery factor, effluent density and breakthrough time of each test. In the

following sections, experimental results are discussed in more details;

4.4.1 Density

Figures 4.3 show the density profiles at the test pressures.

The DMA density values are recorded every 0.01 PV, 6 minutes, and are plotted against the PV of injected gas. The DMA densitometer in these experiments are calibrated for low temperature and low pressure tests, using DI water, toluene, and hexane. Since the experiments are conducted at high pressure and high temperature condition, the density values, plotted in Figure 4.3, are larger than the real value. However, for the purpose of determining the MMP, the density profile and the trend of data are enough for the experiment analysis. Figure 4.3 indicates that at each test pressure, the density is constant before the gas breakthrough. This constant density represents the density of initial oil in place in the slim tube. Tracking the pressure and recorded density data, show that the initial oil density increases from $\rho_o = 1326.7 \frac{Kg}{m^3}$ at $P = 1230\,psi$ to $\rho_o = 1349.6 \frac{Kg}{m^3}$ at $p = 4600\,psi$, indicating a slight compressibility of oil. Figure 4.3 depicts that the gas breakthrough time delays by increasing pressure. At pressures up to $p = 3260\,psi$, some fluctuations happen in the density profile after the gas breakthrough time. The reason is that, the DMA device has a chamber which gets filled with the effluent passing through it. After the gas breakthrough, this chamber is partially filled with the injection gas and initial oil, therefore, the recorded value is the density of a two-phase mixture. This mixture density, depends on the fraction of the fluid present in the chamber, which continuously change after the gas breakthrough, hence, creating the fluctuations. At

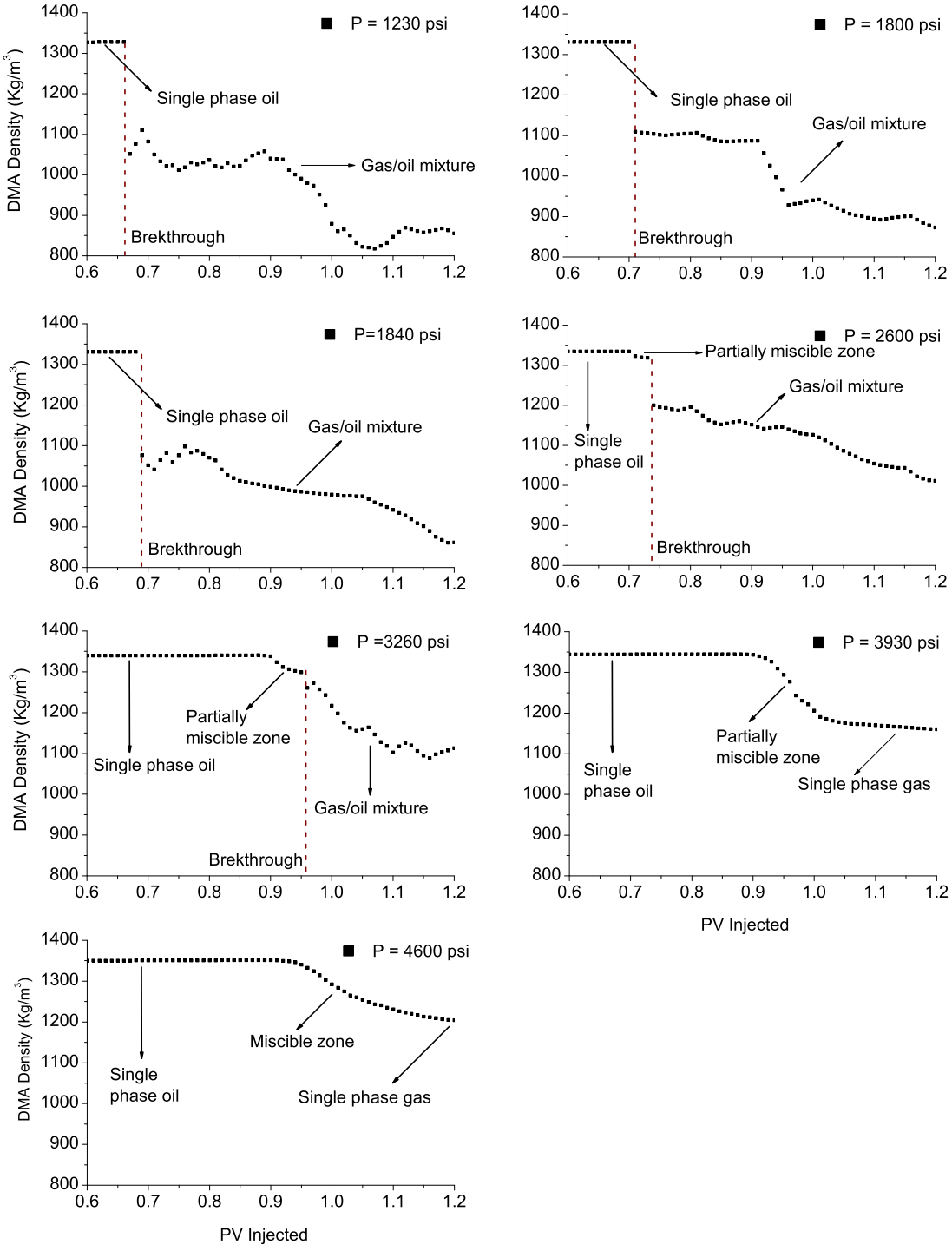

Figure 4.3: DMA density against PV injected for the slim tube tests

higher pressures, $p = 3930\,psi$ and $p = 4600\,psi$, no breakthrough is recorded by the DMA densitometer, although the gas breaks through at the outlet and is produced in the separator. As illustrated in Figure 4.3, at lower pressures, up to $2600\,psi$, the density profile shows a sharp jump from oil density values, to the lower gas densities, at the breakthrough time, when the bubbles arrive at the DMA. This indicates that two distinct phases are still present in the system. Yet, the density profile at $p = 2600\,psi$, shows that before the detection of the bubbles at the DMA, the density decreases gradually for almost 0.03 pore volumes just before the breakthrough time which is an indication of a small level of miscibility in the system. By increasing the pressure a more gradual reduction of effluent density is observed before the breakthrough time. At $p = 3260\,psi$, a higher level of miscibility is observed and the length of the partially miscible zone is increased to 0.06 PV. At $p = 3930\,psi$, a gradual and smooth reduction of density from liquid density to the gas density happens which shows an almost full miscibility between injected gas and initial oil. Finally, at $p = 4600\,psi$, the density changes very smoothly from liquid density to the gas density. This indicates that a fully miscible zone is established between the injection gas and the initial oil and therefore, miscibility has been developed. However, examining the density data does not provide the MMP value. In fact, it only reveals if the miscibility has been achieved at a specific pressure. Therefore, a better method is required for an accurate estimation of the MMP.

4.4.2 Compositional Analysis

An Agilent Gas Chromatography 7890a, is used for the compositional analysis of the experiment effluents. This GC is equipped with a nonpolar MXT-1 capillary column. The column is 15 m long, with inner diameter of 0.25 mm and 0.10 μm thickness of coating phase. This is a Siltek-treated stainless steel, manufactured by Restek Corporation. Three major steps are involved in the separation of components present in the fluid under analysis: (1) Injection of the sample into the GC, (2) Separation of the sample into individual components and (3) Detection of components present in the sample.

Injection of the sample happens using an auto injector installed on the GC system. Normally, to reduce the sample viscosity, simplify the injection process and clean the column after analysis, the crude oil samples are diluted by adding a solvent. In crude oil analysis, CS_2 or C_6 are normally chosen as the dilution solvent. However, in the compositional analysis performed in this research, no dilution solvent is added to the samples as the synthetic oil, $(C_6 - C_{10} - C16)$, is a very light fluid, with a low viscosity and can be cleaned easily from the capillary column. Separation of components take place inside the non-polar capillary column in the oven. Once the sample is injected into the GC injection port and enters the capillary column, it vaporizes by increasing the oven temperature. It is then carried through the column by a carrier gas. In this research, helium is used as the carrier gas. The flow rate of the carrier gas is very accurately controlled by the pressure in the injection port. While the sample is swept through the column it goes through a series of interactions where it is adsorped into the stationary phase in the column and then desorbed back into the carrier stream.

Each sample component is retained based on its solubility in the stationary phase and the boiling point of the sample component. To maximize the sample separation, the oven is usually programmed to increase the temperature with time. The rate of increase of temperature, highly affects the resolution of signals generated at the outlet. A faster increase of temperature gives a lower resolution of the peaks generated at the outlet, while a slower increase of temperature leads to more separated peaks. In this research, the oven temperature starts at 40 ^{o}C, and increases by a rate of 20 $\frac{^oC}{min}$, until a maximum temperature of 315 ^{o}C is achieved. The final stage, is the detection of components which happens using a Flame Ionization Detector (FID). Once the components are separated in the column, they enter into a detector where electrical signals are generated. The signals' area are proportional to the concentration of the samples. The signals are recorded in a data system in the computer where it's called a chromatogram. Eventually the concentration of each component is measured by calculating the area under the signals. Figure 4.4 shows a typical chromatogram generated by the GC.

In Figure 4.4 three peaks have been developed which correspond to three components present in the synthetic oil, C_6, C_{10}, and C_{16}. GC separates the components and shows them as different peaks, but it does not identify to what component each individual peak belongs. In order to identify each peak, the chromatogram is compared to the chromatogram of a calibration sample with known components. Figure 4.5 shows the chromatogram generated by the calibration sample.

The calibration sample used in this research has nineteen components and nineteen peaks are identified in the chromatogram presented in Figure 4.5. As mentioned above, the components present in the calibration sample are already known and using

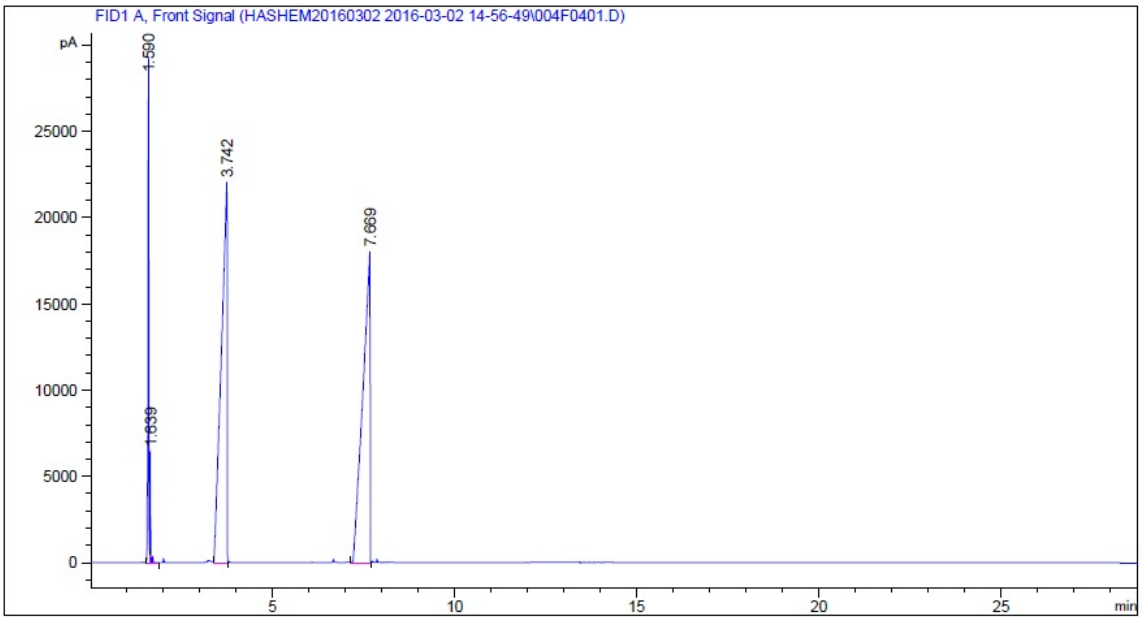

Figure 4.4: A typical chromatogram generated by the GC

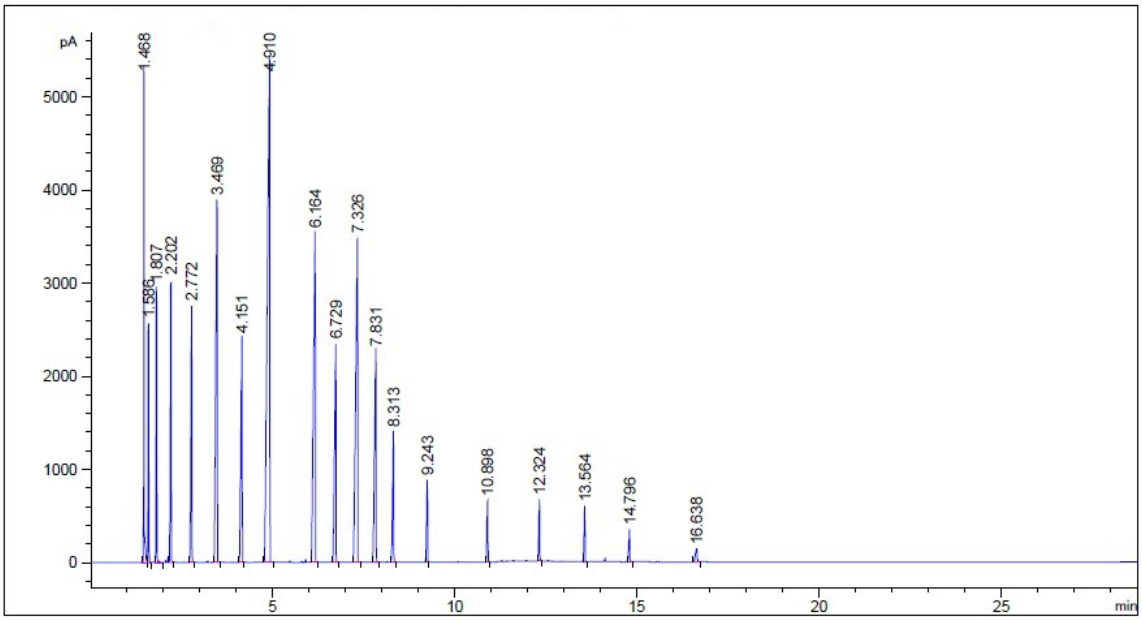

Figure 4.5: Compositional analysis of the calibration sample

the fact that the peaks appear in the order of lightest to heaviest component, all peaks can be assigned to individual components. By comparing Figures 4.4 and 4.5 the unknown peaks in Figure 4.4 can be identified, as each component creates a peak at the same retention time, no matter in what mixture it is. This method for identifying peaks is normally used to identify components of an unknown sample. In this research, however, the samples are know, $(C_6 - C_{10} - C_{16})$, and the very first peak clearly represents C_6, the second peak represents C_{10}, and the last peak shows C_{16}. Yet, the composition of each component needs to be determined by calculating the area under each peak.

In this research, during each MMP test, samples are collected every 0.05 PV and are analyzed by the GC. Analyzing these samples along with recording the volume of collected samples at each step allows us to determine the component recoveries. As an example, Figure 4.6 shows the components' recoveries against the PV of injected gas at the test pressure $p = 1800\,psi$.

The solid line, in Figure 4.6, represents the component recovery obtained from analytical simulations with no volume change upon mixing, experimental results are shown by dots, and the dash line denotes the results from the analytical simulations when the effect of volume change is considered in the calculations. As shown in Figure 4.6, there is considerable disagreement between the experiments and the analytical solution with no volume change. As discussed in Section 3.3.3.3, ignoring the effect of volume change speeds up the leading waves and, therefore, results in an overestimated recovery factor of individual components. In the experiments conducted in this research, CO_2 concentration in the injected gas is 28.2 %. Since CO_2 has a high solubility in the synthetic oil ($C_6 - C_{10} - C_{16}$, it has a remarkable effect on elementary

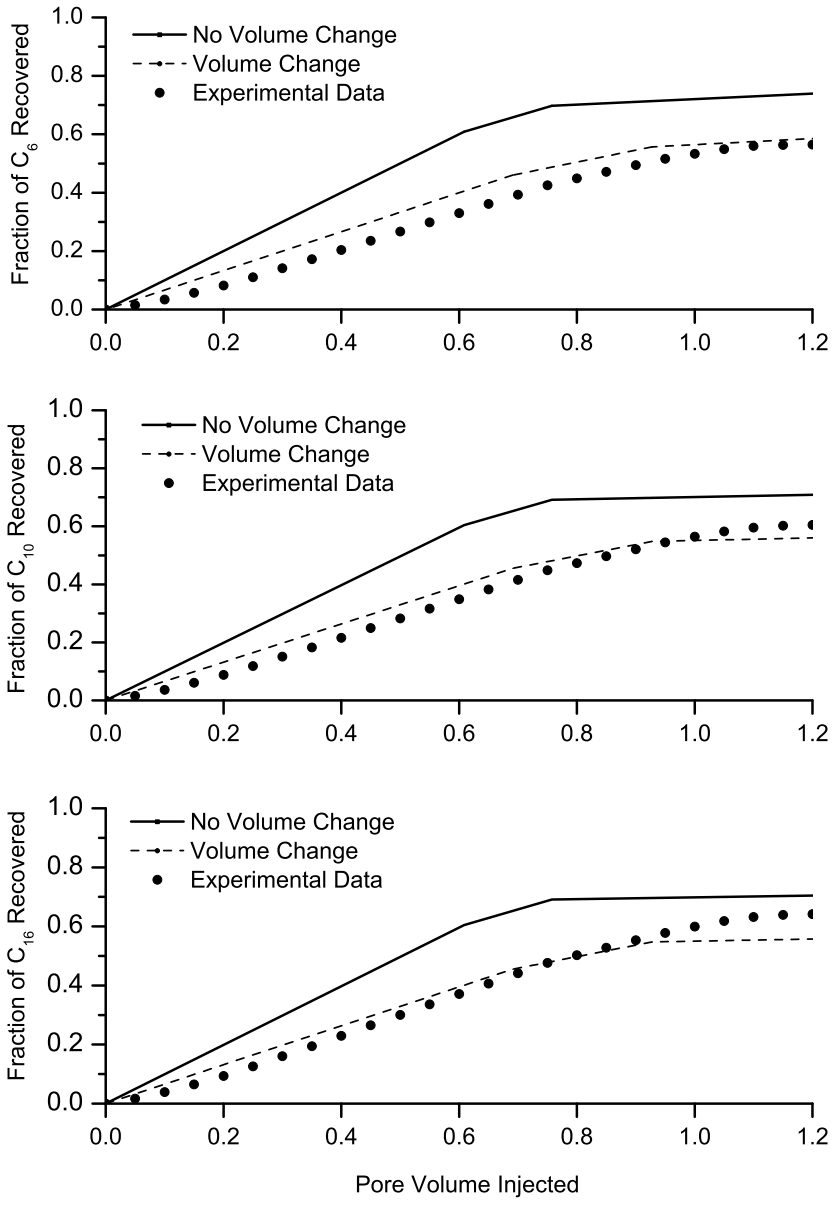

Figure 4.6: Component recovery at 1800 psi and 98 ^oC.

wave velocities, and hence, on the recovery factor. These results illustrates that no volume change upon mixing is not a good assumption for gas/oil displacement studied in this research. Figure 4.6 also shows that by including the effect of volume change, an excellent agreement between experimental results and analytical simulations is achieved.

4.4.3 Breakthrough Time

The gas breakthrough time in each test is determined by taking pictures from the sight glass every minute. Since the gas is injected with $0.12\frac{PV}{hr}$, each minute represents 0.002 PV, as

$$1\,min \times \frac{1\,hr}{60\,min} \times \frac{0.12\,PV}{hr} = 0.002PV \tag{4.8}$$

The DMA densitometer can also be used to determine the gas breakthrough time. At the time when gas bubbles reach to the DMA, a sudden change of effluent density is observed. Table 4.3 shows the breakthrough time determined from both sight glass and the DMA density data.

Table 4.3: Breakthrough time for slim tube tests

Pressure (psi)	**Breakthrough Sight Glass (PV)**	**Breakthrough DMA (PV)**	**Corrected DMA (PV)**	**Difference Error (%)**
1230	0.63	0.67	0.63	0.0
1800	0.66	0.71	0.67	1.5
1840	0.64	0.69	0.65	1.6
2600	0.72	0.74	0.70	2.8
3260	0.94	0.96	0.92	2.1
3930	NA	NA	NA	NA
4600	NA	NA	NA	NA

Table 4.3 indicates that by increasing the pressure the gas breakthrough time is also increasing. This is because of slower leading waves at larger pressures. Comparing the breakthrough times obtained from the sight glass and the DMA, columns "Breakthrough Sight Glass PV" and "Breakthrough DMA (PV)" in Table 4.3, shows that the breakthrough times achieved from DMA density are larger than those actual values recorded by the sight glass and the camera. The delay observed in the gas breakthrough time in the DMA, is because of tubing and valves' volume between the sight glass and the densitometer. Therefore, the breakthrough time obtained from the DMA needs to be corrected by subtracting the dead volume between the sight glass and the DMA. This dead volume is calculated by filling the path with toluene as,

$$V_{d,SG-DMA} = V_{inj} - V_{prod} = 35\,ml - 23.8\,ml = 11.2\,ml \times \frac{1\,PV}{310.8\,ml} = 0.04\,PV \quad (4.9)$$

In Equation 4.9, $V_{d,SG-DMA}$ is the dead volume between the sight glass and the DMA densitometer. The corrected DMA breakthrough times are calculated by subtracting $V_{d,SG-DMA} = 0.04\,PV$ from DMA breakthrough times and is shown as "Corrected DMA (PV)" in Table 4.3. The error in calculating the breakthrough time from DMA is calculated and shown in Table 4.3 as "Difference Error (%)". Table 4.3 shows that at the last two experiments, $p = 3930psi$ and $p = 4600psi$, no gas breakthrough was observed in neither sight glass nor the DMA. This is because a high degree of miscibility at $p = 3930psi$ and a full miscibility at $p = 4600psi$ occur between the injection gas and the initial oil which eliminates the interface between the gas and the oil. This is in agreement with the density profiles shown in Figure 4.3,

where the density is smoothly reducing from the liquid density to the gas density through a miscible zone. By the development of the miscible zone, the very sharp interface between the injected gas and initial oil disappears, and therefor no gas breakthrough is observed in the sight glass. Figure 4.7 shows the pictures taken at the gas breakthrough time.

Figure 4.7 shows the gas bubbles broken through at the outlet. Yet, as discussed above, no breakthrough was recorded at $p = 3930psi$ and $p = 4600psi$.

a) P = 1230 psi, PV = 0.63

b) P = 1800 psi, PV = 0.66

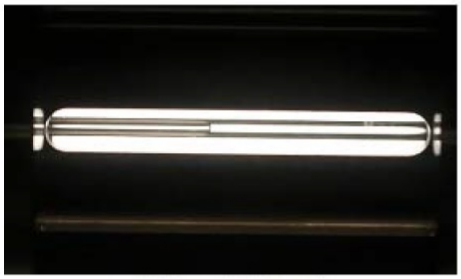

c) P = 1840 psi, PV = 0.64

d) P = 2600 psi, PV = 0.72

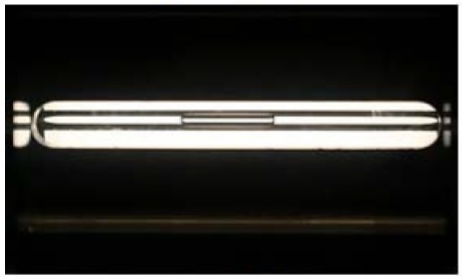

e) P = 3260 psi, PV = 0.94

f) P = 3960 psi, PV = NA

g) P = 4600 psi, PV = NA

Figure 4.7: Pictures of sight glass at test pressures

4.4.4 Pressure Profiles

During slim tube tests, the outlet pressure is kept constant using a Back Pressure Regulator (BPR) and the gas is injected at a constant flow rate of 0.12 PV/hr. Constant outlet pressure along with constant gas injection rate of 0.12 PV/hr, necessitates to have a varying inlet pressure and varying differential pressure between the inlet and outlet accordingly. Figure 4.8 shows the differential pressure over the slim tube versus pore volumes of injected gas, at different test pressures.

As shown in Figure 4.8, at the beginning of the tests, the differential pressure over the tube has a minimum value since the tube is fully saturated with oil and there is no flow in the medium. By starting the test, the gas is injected at a flow rate of 0.12 PV/hour and hence the injection pressure has to increase, in order to create such a flow rate. Figure 4.8 indicates that in all slim tube experiments, the differential pressure is gradually increasing to a maximum value which is required if a flow rate of 0.12 PV per hour is desired. The maximum differential pressure depends on the total mobility of the fluids, λ_T. Therefore, as shown in Figure 4.8, the maximum differential pressure increases with the test pressure, as fluid viscosities increase with pressure. By injecting more gas into the medium, more volume of the porous medium is occupied by highly mobile gas and less injection pressure is required to keep the flow rate at the 0.12 PV per hour. Thus, the differential pressure starts decreasing after it has reached the maximum value. In all the experiments up to $p = 3260psi$, scatter points are observed at the end of the profile. The reason is that the slug type flow happens in the tube. After breakthrough, when most of the recoverable oil is produced, a continuous flow of gas is created in the system and this continuous flow

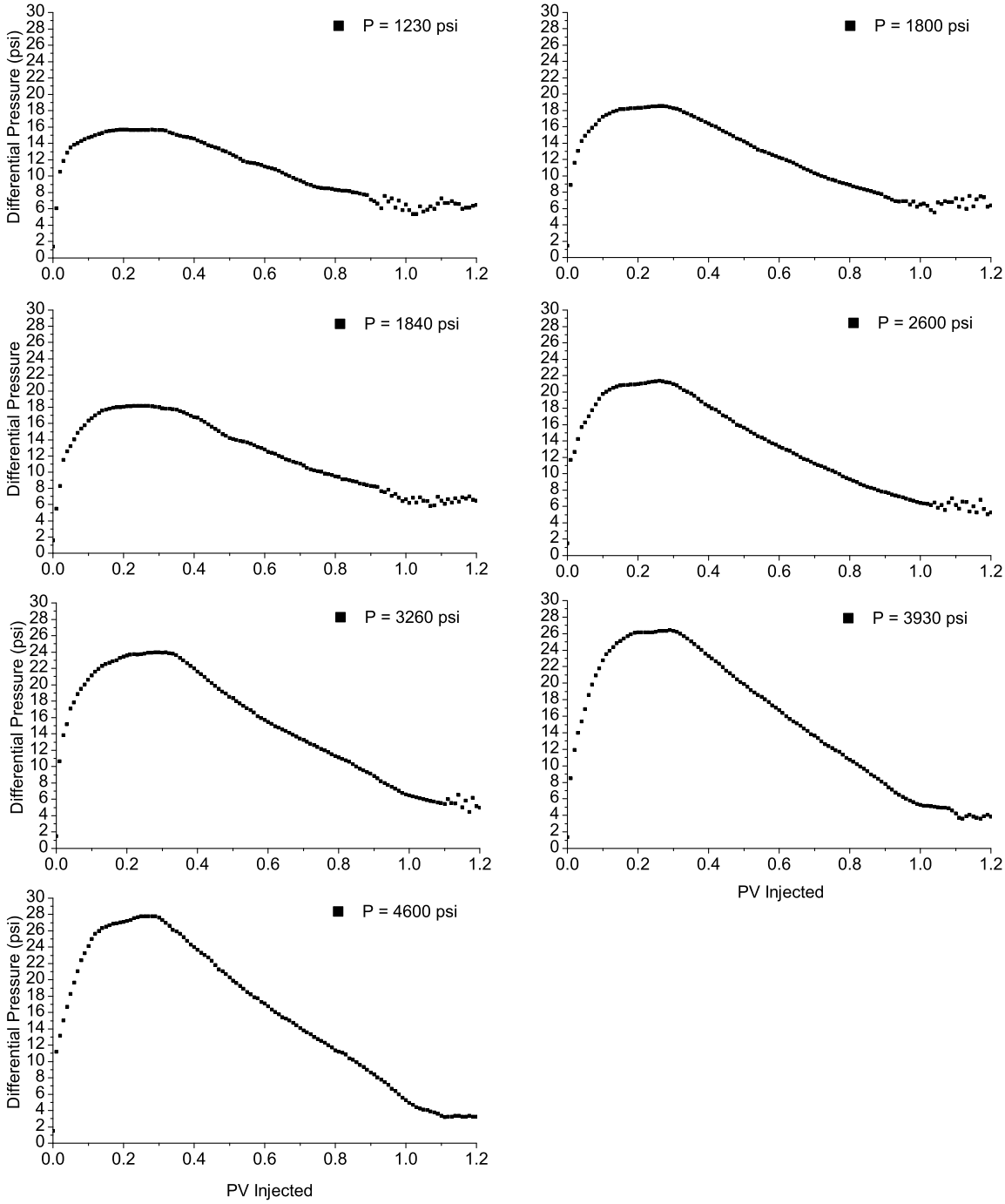

Figure 4.8: The differential pressure over the slim tube against PV injected for slim tube tests

is sometimes interrupted by mobilized oil droplets leading to scatter points in the pressure profile.

4.4.5 Minimum Miscibility Pressure

The oil recovered from the slim tube at 1.20 PV of injected gas is recorded at each test pressure and given in Table 4.4.

Table 4.4: Recovery factor values in slim tube experiments at 1.20 PV gas injection

Pressure (psi)	**Recovery Factor (%)**
1230	50.30
1800	61.51
1840	60.54
2600	69.10
3260	76.87
3930	88.45
4600	90.25

Raw slim tube test data and a sample calculation of recovery factor are given in Appendix A. As expected, the recovery data in Table 4.4 shows that the recovery factor increases by increasing the pressure. The rate of increase of recovery, however, is faster at lower pressures. The data show that in the last experiment, $p = 4600\,psi$, the recovery factor has increased only 1.8 % by 630 psi increase in pressure. For precise determination of MMP, the recovery data need to be plotted against the pressure. This is shown in Figure 4.9.

The miscibility criterion used in this research is the location of break point on the recovery curve. As shown in Figure 4.9, the MMP for this gas/oil system is 4178 psi. Comparison of the MMP calculated using analytical techniques in Section 3.4 and

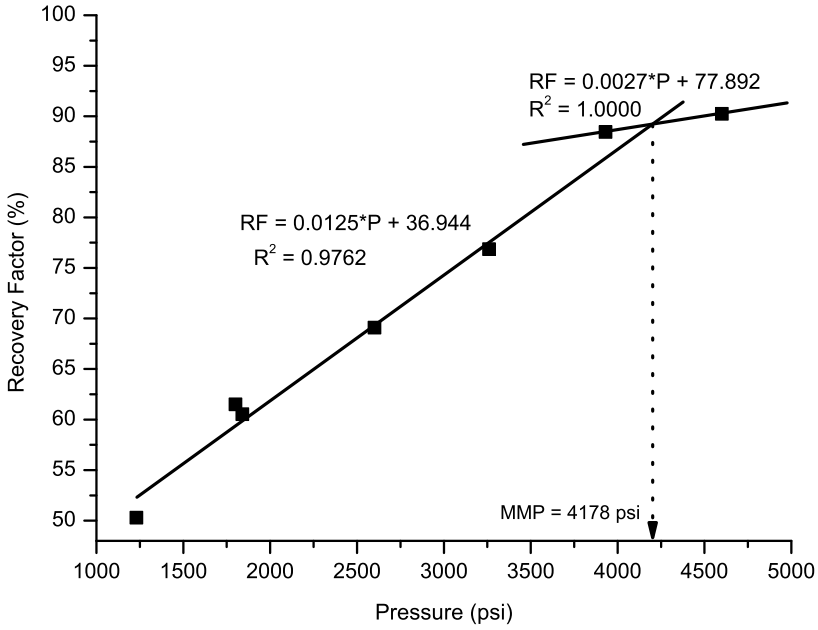

Figure 4.9: MMP determination of the five-component system studied in case studies 2 and 3 at 98 ^oC.

the MMP obtained from slim tube experiments shows the remarkable accuracy of the analytical approach. For more clear comparison, MMP calculation from analytical method is shown in Figure 4.10.

The relative error associated with the analytical approach is calculated from Equation 4.10,

$$E_{MMP} = \frac{|MMP_{slimtube} - MMP_{analytical}|}{MMP_{slimtube}} \times 100 \tag{4.10}$$

Where E_{MMP} is the relative error in the MMP obtained from analytical method, $MMP_{slimtube}$ is the MMP calculated from slim tube experiments, and $MMP_{Analytical}$ is the MMP value obtained from analytical method. Therefore,

$$E_{MMP} = \frac{|4178 - 4140|}{4178} = 0.91\% \tag{4.11}$$

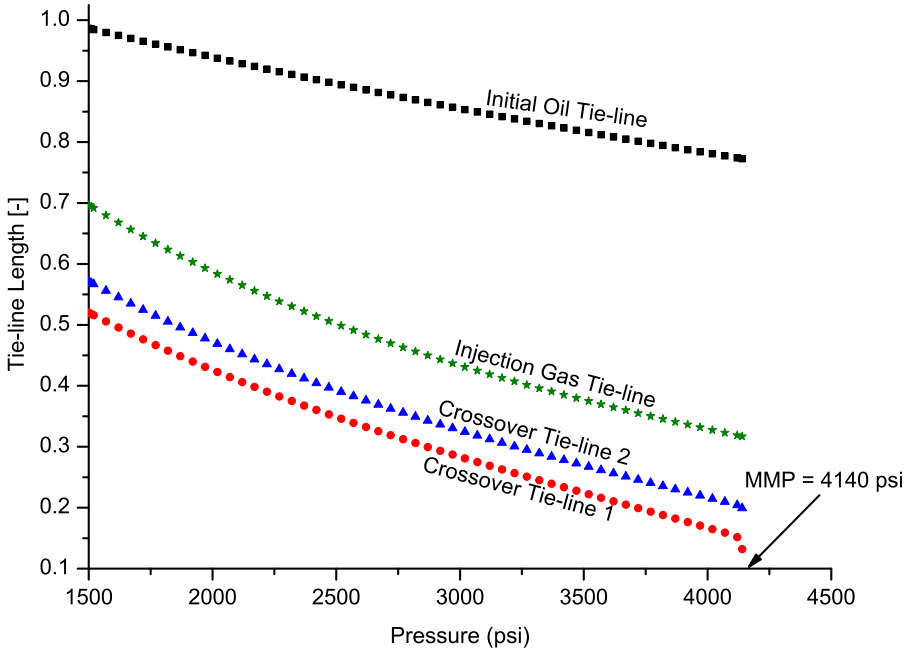

Figure 4.10: Tie-line length against pressure for the five-component system

An error as small as 0.91 % clearly declares the robustness of analytical approach in estimating the MMP.

4.5 Experimental Slim Tube Conclusion

The experimental set up was explained in this chapter. The set up features and properties were determined and slim tube experiments were conducted on a five-component gas/oil system. The experimental results including the density profiles, pressure profiles, breakthrough time, composition of the collected effluent, and the recovery factor data were analyzed. We found that the density profile is a very helpful tool to determine the miscibility development, yet, it is not enough to determine the MMP. The density data indicated that by increasing the pressure the length of misci-

bile zone also increases. The gas breakthrough time was determined using sight glass pictures and the DMA density data. By increasing the pressure, the breakthrough was delayed and at last two test pressures, $p = 3930\,psi$ and $p = 4600\,psi$, no breakthrough was recorded which was because of developing miscibility and development of miscible zone between the injection gas and initial oil. The compositional analysis gives us the component recovery and a comparison of the experimental component recoveries with analytical solution results reveals that volume change upon mixing has a substantial effect on the accuracy of solution obtained from analytical technique. Finally, a graph of recovery versus pressure showed that the MMP between the injected gas and the synthetic oil is 4178 psi. Comparison of this value with the MMP obtained from analytical method depicts 0.91 % error in calculating the MMP by the analytical technique, indicating the robustness of this method. Besides the accuracy, the analytical technique also provides the miscibility mechanism in the system. The miscibility mechanism in the case studied in this research, injection of $N_2 - CO_2$ gas into slim tube saturated with the synthetic oil $C_6 - C_{10} - C_{16}$ at $98\,^oC$, is discovered to be combined vaporizing/condensing mechanism.

Chapter 5

Experiments: Gas/Oil Displacements with Constant Pressure Boundaries

In Chapter 3, the newly developed analytical approach was spelled out for multi-component gas/oil displacements with constant pressure boundaries. Three case studies were chosen to explain the application of the technique. Case study 1 was a hypothetical four-component system with constant K-values, whereas Case studies 2 and 3 were realistic five-component systems at reservoir condition, replicable by experiments. In Chapter 4 the slim tube experimental set up was described and slim tube experiments were conducted to determine the MMP for the five-component system, to investigate the reliability of Jessen's approach in the MMP determination. In this chapter, for the first time, Slim tube experiments are conducted under constant injection and production pressures. The purpose of the experiments is not determin-

ing the MMP, but is validating assumptions made to develop the analytical solution of multi-component gas/oil displacements with constant pressure boundaries. These assumptions include: (1) one-dimensional flow, (2) the effect of dispersion and diffusion are negligible, (3) in particular, capillary forces and mechanical dispersion are zero, (4) fluids are incompressible, (5) phases present at any location are in instantaneous equilibrium; and (6) injection and production pressures are constant. Validation of these assumption allows us to use the new theory in a wide range of EOR applications never studied before. This includes multi-component gas injection, polymer flooding, and alcohol injection under constant injection and production pressures. The developed analytical technique can be further applied in three-dimensional reservoirs by employing the concept of stream tubes. A great application is in optimization problems such as optimal well displacement. In order to achieve the stated goals, two experimental case studies, 4 and 5, are completed in this chapter. Furthermore in this chapter, a history matching of analytical solution results to the experimental data is used to determine the gas/oil relative permeability data. The relative permeabilities are then independently validated using a novel interpretation approach, based on experiments with constant pressure boundaries. In the following sections, the history matching approach is explained first, then experimental Case studies 4 and 5 are illustrated. Finally, a new method for the interpretation of relative permeability data is introduced and the relative permeability data obtained from history matching is validated by the newly developed method.

5.1 Methodology

Cleaning and saturation procedure explained in Section 4.3 is employed to prepare the slim tube set up for constant pressure bounadry experiments, i.e. Case studies 4 and 5. In Case studies 4 and 5, for the first time, slim tube experiments are conducted at constant inlet and outlet pressures. The outlet pressure is controlled using a Back Pressure Regulator (BPR) and the inlet pressure is fixed by operation the advanced injection Quizix pump at constant pressure mode. Case studies 4 and 5 are completed at $p_{ave} = 531.9 \pm 3.1\, psi$ and $p_{ave} = 934.5 \pm 3.5\, psi$, respectively. The experiments can be conducted at any higher pressure, with the same procedure as mentioned here. According to high absolute permeability of the slim tube, $K = 24.2 \pm 0.6\, D$, and in order to achieve the purpose of constant pressure boundaries' displacement, it is better to keep the differential pressure at lower values. The experience of the researcher shows that a differential pressure equal to $10.0\, psi$ is reasonable for the current experiments. To perform the experiments at higher differential pressure, smaller packing materials (silica grains) should be used to reduce the slim tube absolute permeability. To conduct the experiments, the slim tube is saturated with the synthetic oil and the BPR is set to 500.0 psi and 900.0 psi for Case studies 4 and 5, respectively. However, after setting the BPR pressure, the synthetic oil injection is continued to determine the exact flow pressure of the BPR, as a pressure higher than the BPR pressure is required to create a flow through BPR. Once the flow pressure of the BPR is known, the injection gas pressure is set to be 10.0 psi larger than than the flow pressure. Now, the set up is ready to start the experimental Case studies 4 and 5. The experiments start with opening the inlet valve and operation the injection pump at the constant

pressure mode. The experiments are conducted for 12.5 hours. The effluent volume is recorded every 10 minutes. The experimental data are given in Appendix B. The most important results of the constant pressure boundary slim tube experiments are the gas breakthrough time and the total velocity of effluent as a function of time. As the experiment continues for 12 hours, the pressure data are recorded every 3 minutes to track the pressure profiles. The density data are recorded as well. However, the density data are not important in Case studies 4 and 5, as the main output of the developed analytical technique are the gas breakthrough time and the total velocity as a time dependent parameter. In this chapter, constant pressure boundaries' experiments in the slim tube set up are conducted first. The gas breakthrough time and the total velocity of effluent are recorded and are compared with the analytical simulation results. Afterwards, the analytical simulation data are matched to the experimental data to obtain the gas/oil relative permeability in the slim tube. Finally, a novel interpretation method is used to validate the relative permeability curves, obtained from history matching.

5.2 Results

Following the methodology explained above, Case studies 4 and 5 are completed at constant pressure boundaries, therefore, constant differential pressure over the slim tube. Two types of results are obtained in Case studies 4 and 5; experimental results and analytical simulation results. Experimental results include: the gas breakthrough time, total velocity of the effluent as a function of time, the DMA density profile, and pressure data. The analytical simulation results include gas breakthrough time and

the total velocity profiles. After conducting the experiments, experimental results and analytical simulation results must be compared to validate the assumptions made in analytical simulations. The gas breakthrough time and the total velocity profiles are results to be compared. The density data, however, are not representative in Case studies 4 and 5, since the miscibility is not achieved. Thus, the density data are not presented in this section. Yet, all the experimental data, including the density, are presented in Appendix B. In this section, the differential pressure profiles are shown, in order to show that the pressures are fixed at the boundaries. Then, the gas breakthrough time and total velocity profiles calculated analytically are compared with those obtained from experiments. Afterwards, since the slim tube relative permeabilities are not known, gas/oil relative permeability curves are determined by matching the analytical solution to the experimental data, via adjusting the Corey parameters. This history matching shows that analytical simulation results match to the experiments if reliable relative permeabilities are employed. In the other words, assumptions made in the analytical solutions are valid if the slim tube relative permeability data are known. Yet, the matched relative permeabilities needs to be validated by an independent method. This is done, through a novel interpretation method of experiments.

5.2.1 Case Study 4: Constant Pressure Boundary Experiments at $\mathbf{P_{ave} = 531.9\,psi}$

In this case study, it is tried to confirm the analytical modelling of constant pressure boundary systems by conducting an experiment corresponding to the mathematical

modelings in Case study 2. However, for the sake of simplicity the system information are again provided in Table 5.1.

Table 5.1: Input parameters for the five-component system (Case study 2)

Component	**Composition (mole fraction)**				
	N_2	**CO_2**	**C_6**	**C_{10}**	**C_{16}**
Synthetic Oil	0.000	0.000	0.200	0.500	0.300
Injection Gas	0.718	0.282	0.000	0.000	0.000

Parameter	**Value**
Oil Viscosity, μ_o (cP)	0.65447
Gas Viscosity, μ_g (cP)	0.02048
Viscosity Ratio, $M = \frac{\mu_o}{\mu_g}$	31.957
API Gravity, (^oAPI)	58.4
Displacement Length, L (m)	24.0
Porosity, ϕ	0.42
Absolute Permeability, K (D)	24.2
Inlet Pressure, p_{in} (psi)	537.5
Outlet Pressure, p_{out} (psi)	526.3
Average Pressure, p_{ave} (psi)	531.9
Constant Differential Pressure, Δp (psi)	11.2
Residual Oil Saturation, S_{or}	0.10
Connate Water Saturation, S_{wc}	0.00
Critical Gas Saturation, S_{gc}	0.00
Temperature, $T(^o\text{C})$	98.0

Gas and oil viscosities are measured in the lab using a high pressure high temperature Cambridge viscometer. In this case study a residual oil saturation of $S_{or} = 0.1$ is considered for the slim tube, and it is assumed that the residual oil saturation remains is constant for the set up. The residual oil saturation of $S_{or} = 0.1$ is assumed for this system based on the fact that at the last slim tube test in Chapter 4, almost 10% of initial oil in place was not recovered from the system. During the experiment, the outlet pressure is controlled by a BPR and the inlet or the injection pressure is controlled using advanced Quizix pumps. Before starting the constant pressure

boundary experiments, the slim tube set up was cleaned and pressure tested for possible leaks. Pressure transducers were also tested and refilled with Silicone oil. The main difference between constant pressure boundary experiments and regular MMP experiments is that in common MMP experiments, the whole system is set to the BPR pressure and the test is started by injection of gas at inlet with flow rate of 0.12 PV per hour, while in constant pressure boundary experiments, the injection gas pressure is set to be a certain value larger that the saturated slim tube back pressure. This certain value is the constant differential pressure that is desired between the inlet and the outlet. The experiment is then started by operation of the injection pump at constant pressure to keep the differential pressure constant. The differential pressure profile is presented in Section 5.2.1.1.

5.2.1.1 Pressure Profile

Figure 5.1 presents the differential pressure between the inlet and the outlet of the slim tube in Case study 4. The experiment is conducted for 820 minutes and the pressure is recorded with time.

Figure 5.1 indicates that the differential pressure remains fairly stable before the breakthrough time. However, after the breakthrough time some fluctuations are observed in the system. The standard deviation of data plotted in Figure 5.1 is calculated to be 0.4 psi, indicating the closeness of data points to the average of $11.2 \pm 0.3\,psi$. The solid line in Figure 5.1 indicates a constant differential pressure equal to 11.2 psi. This solid line and the calculated standard deviation illustrate that although some pressure fluctuations are observed in the system, the average differential pressure of 11.2 psi is a good approximation for this experiment.

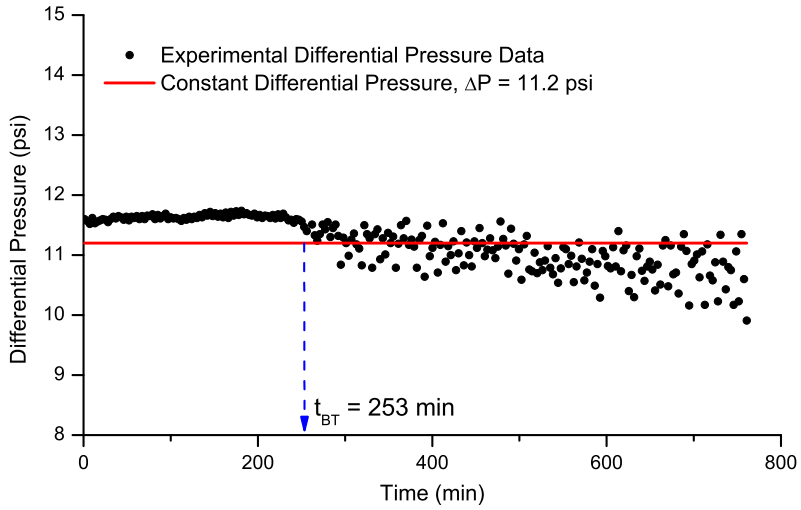

Figure 5.1: Differential pressure measured over the inlet and the outlet in Case study 4

5.2.1.2 Total Velocity

Figure 5.2 presents the total velocity of the effluent exiting the slim tube.

During the experiment, the produced oil is collected in a graduated cylinder and the volume of the gas is recorded using a gas meter. The gas and oil volumes are recorded at room temperature and atmospheric pressure, therefore, the data are converted to the reservoir condition and the total velocity is calculated using the below equation,

$$u_T = u_{Oil} + u_{Gas} = \frac{q_{Oil}}{A} + \frac{q_{Gas}}{A} \tag{5.1}$$

A sample calculation of total velocity, using Equation 5.1, is given in Appendix B.1. By starting the experiment, the injection gas invades into the slim tube and the total velocity increases slowly with time. The total velocity keeps increasing slowly until the breakthrough time at 253 minutes. After the breakthrough time there is an open path for the gas and therefore the total velocity increases faster. The reason is that

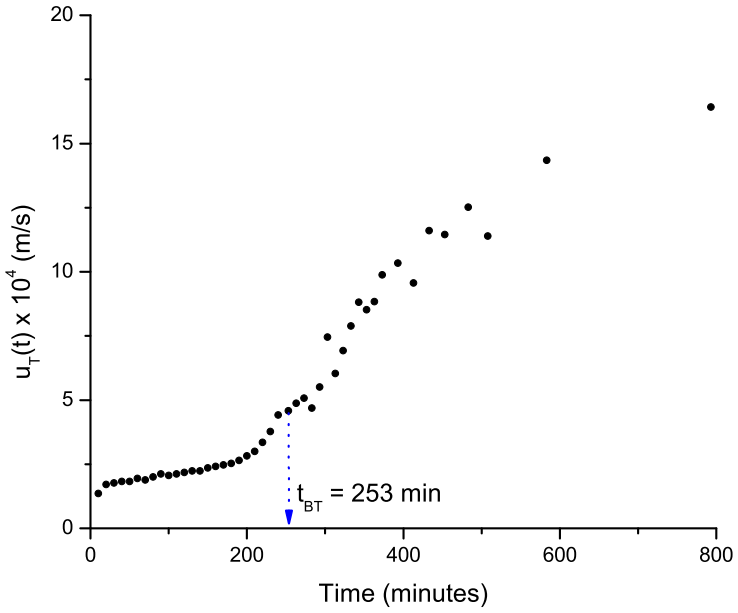

Figure 5.2: The total velocity of the gas/oil displacement system under constant pressure boundary condition and average displacement pressure of 531.9 psi (Case study 4)

in Equation 5.1, the u_{Gas} is the dominant term and it takes larger values compared to the u_{Oil} as the gas has much higher mobility. However, the total velocity does not increase monotonically and there are some fluctuations in the velocity profile. This is because of the slug flow that sometimes happens in the system. Figure 5.3 shows the total velocity obtained from the experiments along with the total velocity obtained by the analytical simulation of the displacement.

The analytical result shown in Figure 5.3 is determined with the basic Corey parameters for the relative permeability curves, i.e. $a_g = 1$, $n_g = 2$, $a_o = 1$, and $n_o = 2$. Figure 5.3 clearly shows that basic Corey parameters are not appropriate to model the relative permeability of the fluids in this system. Figure 5.3 indicates that the basic Corey parameters, can lead to a fairly accurate analytical results at early times

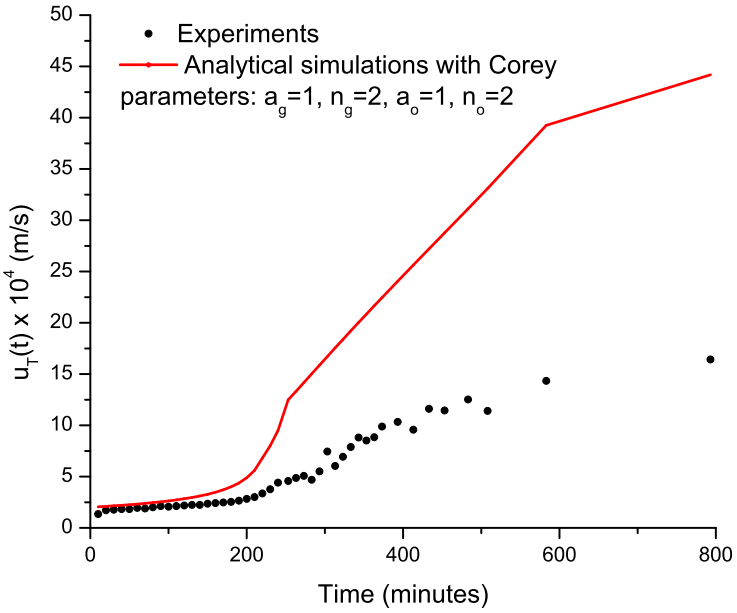

Figure 5.3: The experimental total velocity and the analytical results obtained with basic Corey parameters (Case study 4)

after starting the experiments. A while after, the analytical solution deviates from the experimental data and this deviation becomes larger and larger by passing the time. The relative permeability curves directly affect the total velocity, i.e. in specific saturation values, increasing the relative permeability of each fluid increases the velocity of that fluid. Therefore, Corey parameters have substantial effect on the analytical solutions. Figure 5.3 shows that a huge difference between the analytical solution and the experimental data happens at later time after the breakthrough time, when the gas has the dominant flow. Therefore, this is not wrong to say that the gas relative permeability needs a higher level of adjustment. Yet, Corey parameters need to be adjusted for the oil relative permeability as well. Using the basic Corey parameters leads to a 11.86% error in determination of the breakthrough time and 44.99% error

in total velocity calculation. However, the history matching approach presented in Section 5.2.1.3 shows that remarkable effect of Cory parameters on the analytical simulation results. In Section 5.2.1.3, the Corey parameters are adjusted to match the analytical solution to the experimental data. The obtained relative permeability curves are then independently validated in Section 5.3.

5.2.1.3 History Matching

In this section it is described how to match the experimental data to the analytically simulated data. In the history matching process, the experimental data to be matched must be selected first. The match data depend on availability and the reliability of the data. Then, the adjustable reservoir and fluid properties must be selected. These data must be those with the highest uncertainty and they should have significant effect on the simulation results. In this work, the gas breakthrough time and the effluent velocity data are the reliable results for the history match and the factors that have the highest effect on the breakthrough time are the Corey parameters as they control the velocity of gas and oil when flowing simultaneously. However, the fluid and reservoir properties such as porosity, permeability, pore volume, and etc are determined experimentally and are not a good choice for the history matching. The general shape of Corey-type relative permeability models is given in 5.2 [8].

$$\begin{aligned} K_{rg} &= a_g\left(\frac{S_g - S_{gc}}{1 - S_{gc} - S_{or}}\right)^{n_g}, \\ K_{ro} &= a_o\left(\frac{1 - S_g - S_{or}}{1 - S_{gc} - S_{or}}\right)^{n_o}. \end{aligned} \tag{5.2}$$

In Equation 5.2, a_g and a_o are constants that represent the endpoint values on gas

and oil relative permeability curves, respectively. Theoretically, a_g and a_o can take values from 0 to 1, as the relative permeability of each phase varies between 0 and 1. n_g And n_o are called the Corey indexes. Corey indexes, n_g and n_o, depend on the rock and fluid properties, and can take values from 1 to 4 [17]. A step by step procedure to match the Corey parameters is given below:

1. By solving system of Equations 2.45, determine the key tie-lines in the system and find the equilibrium liquid and vapor compositions along each tie-line.

2. Using the fluid compositions obtained in Step 1, apply PR EOS to determine the density of equilibrium liquid and vapor along key tie-lines.

3. Set Corey parameters for the analytical solution. In this research, a_g and a_o are allowed to vary between 0.0 and 1.0, and Corey indexes, n_g and n_o, change from 1.0 to 4 [17].

4. Considering volume change upon mixing, determine the key saturation points using the procedure described in Section 2.2.3.

5. Following Section 3.3.3.3, calculate the local velocities of the key point and determine the gas saturation profile.

6. Following Section 3.2.3 and using Equation 3.19, determine the gas breakthrough time.

7. Compare the calculated breakthrough time with the experimental value and calculate the relative error of the estimated breakthrough time from the following equation,

$$E_{BT} = \frac{|t_{BT,calculated} - t_{BT,experiment}|}{t_{BT,experiment}} \times 100 \tag{5.3}$$

8. Determine the velocity profile and calculate the average relative error for the

velocity by the following equation,

$$E_{Velocity} = \frac{1}{N}\sum_{1}^{N}\frac{|u_{T,calculated} - u_{T,experiment}|}{u_{T,experiment}} \times 100 \tag{5.4}$$

9. Determine the total average error using a weighted average of E_{BT} and $E_{Velocity}$. In this work, weight 1 is given to the E_{BT} and weight 2 is given to the $E_{Velocity}$. The weighting E_{BT} and $E_{Velocity}$ depends on the reliability and importance of the data as well as the number of data points available for the matching. In the Case studies studied here, the gas breakthrough time and the total velocity data are available for the matching. The gas breakthrough time is of high importance but only one data point is available. On the other hand, more data points of the total velocity are available for the matching. Therefore, weight factors of 1 and 2 are selected for the E_{BT} and $E_{Velocity}$, respectively. The total average error can be calculated from the following equation,

$$E_{ave} = \frac{1}{3}(E_{BT} + 2 \times E_{Velocity}) \tag{5.5}$$

10. Change Corey parameters until a good match of simulated data on experimental data is obtained. In this research, a random search approach is employed to try 10,000 combinations of Corey parameters and find the matched parameters.

As discussed earlier, the deviation of analytical solution from the experimental results is due to the erroneous estimation of the two-phase relative permeabilities. Matching the Corey-type relative permeability curves of oil and gas results in the following relations for the gas and the oil relative permeability data.

$$K_{rg} = 0.55(\frac{S_g}{0.9})^{1.57}$$
$$K_{ro} = 0.90(\frac{0.9 - S_g}{0.9})^{3.16} \tag{5.6}$$

In Equation 5.6, S_g represents the vapor phase saturation. As shown in Equation 5.6, $a_g = 1$ in preliminary analytical simulation is adjusted to $a_g = 0.55$ by the history matching. This new value, $a_g = 0.55$, justifies the remarkable difference between the analytical solution and the experiments, as the basic Corey parameters, $a_g = 1$, $n_g = 2$, $a_o = 1$, and $n_o = 2$ were highly overestimating the total velocity after breakthrough time which was mainly because of high relative probabilities assigned to the gas by $a_g = 1$. Figure 5.4 is the plot of relative permeabilities against the vapor phase saturation.

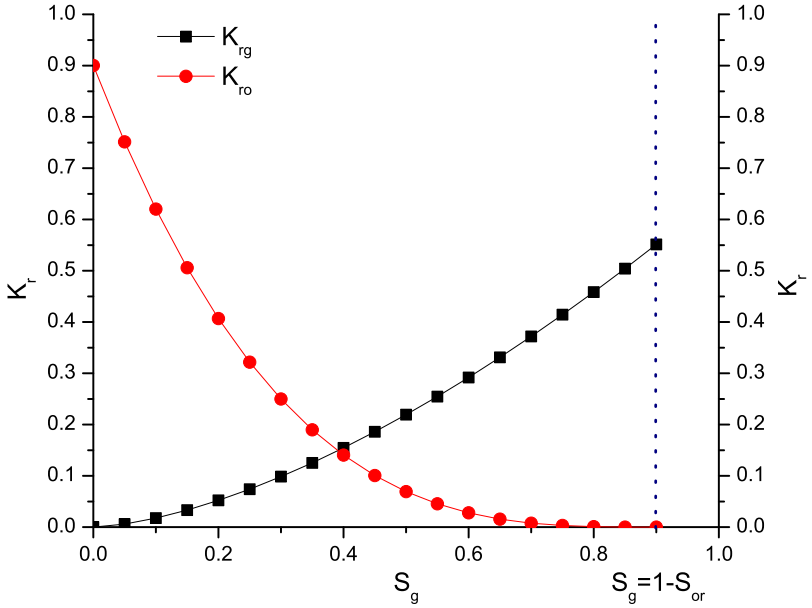

Figure 5.4: Corey relative permeability curves matched with the experimental data (Case study 4)

Employing relative permeability curves shown in Figure 5.4 results in analytical simulation results which are in good agreement with the experimental data. Applying Equation 5.6 in the analytical simulation results in total velocity profile shown in Figure 5.5.

Figure 5.5 illustrates the significant effect of relative permeability data on the analytical simulation results. As shown in Figure 5.5, adjusting the Corey parameters results in 0.3 % error in calculation of gas breakthrough time. Figure 5.5 also shows the good agreement between analytical simulation results and experimental results. An average error of 5.0 % is achieved in calculation of total velocity. However, the relative

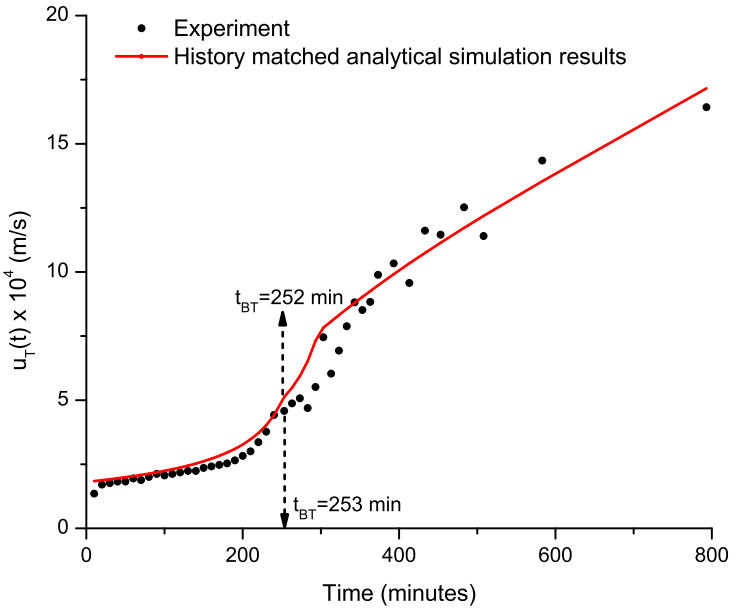

Figure 5.5: History matching of the total analytical velocity to the experimental results (Case study 4)

permeability curves shown in Figure 5.4 still need to validated. This is performed in Section 5.3.

5.2.2 Case Study 5: Constant Pressure Boundary Experiments at $\mathbf{P_{ave} = 934.5\,psi}$

This case study is another practical case for the confirmation of the generalized buckley-Leverett theorem for multi-component gas inject under constant pressure boundaries. The gas and oil used in this experiment are the same as Case study 4. However, the average pressure in this Case study is increased to $P_{ave} = 934.5$ psi. Table 5.2 presents the information used in Case study 5.

The data presented in Table 5.2 illustrates that increasing the average displacement

Table 5.2: Input parameters for the five-component system, $P_{ave} = 934.5\,psi$ (Case study 5)

Component	**Composition (mole fraction)**				
	$\mathbf{N_2}$	$\mathbf{CO_2}$	$\mathbf{C_6}$	$\mathbf{C_{10}}$	$\mathbf{C_{16}}$
Synthetic Oil	0.000	0.000	0.200	0.500	0.300
Injection Gas	0.718	0.282	0.000	0.000	0.000

Parameter	**Value**
Oil Viscosity, μ_{Oil} (cP)	0.71083
Gas Viscosity, μ_{Gas} (cP)	0.02122
Viscosity Ratio, $M = \frac{\mu_{Oil}}{\mu_{Gas}}$	33.498
Displacement Length, L (m)	24
Outer Diameter, OD (mm)	9.52
Inner Diameter, ID (mm)	6.22
Porosity, ϕ	0.42
Permeability, K (D)	24.2
Inlet Pressure, p_{in} (psi)	939.7
Outlet Pressure, p_{out} (psi)	929.2
Average Pressure, p_{ave} (psi)	934.5
Constant Differential Pressure, Δp (psi)	10.5
Residual Oil Saturation, S_{or}	0.10
Connate Water Saturation, S_{wc}	0.00
Critical Gas Saturation, S_{gc}	0.00
Temperature, T ^{o}C	98.0

pressure has affected gas and oil viscosities and consequently the viscosity ratio. By increasing the average pressure, gas and oil viscosities increase, however, the viscosity ratio, M, does not change much. Experimental parameters and slim tube features remain the same, but the differential pressure between the inlet and the outlet is reduced to 10.5 psi. As discussed in Chapter 3, increasing the average pressure slows down the leading elementary waves and a later breakthrough time is expected compared to Case study 4.

5.2.2.1 Differential Pressure Profile

Figure 5.6 shows the differential pressure between the inlet and the outlet of the slim tube.

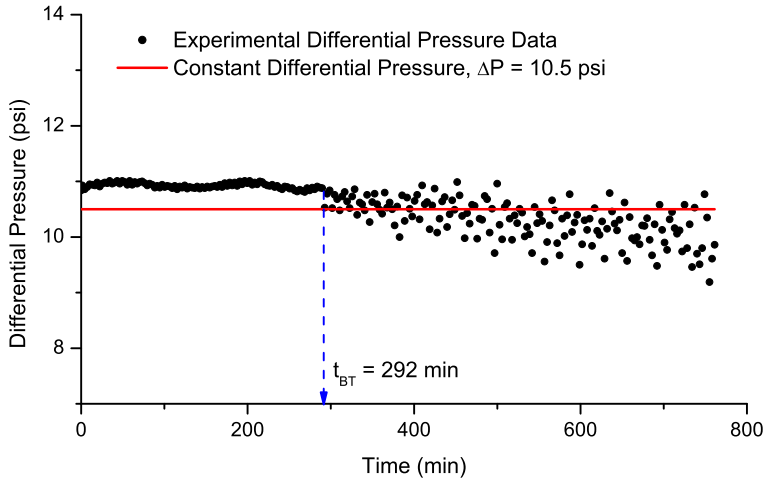

Figure 5.6: Differential pressure measured between the inlet and the outlet in Case study 5

As shown in Figure 5.6, the breakthrough time, in Case study 5, is 292 minutes. Like Case study 4, the pressure data are fluctuating after the breakthrough of the gas at the outlet. The average differential pressure for this displacement is 10.5 psi which is 0.7 psi less than Case study 4. The 0.7 psi less average pressure postpones the breakthrough time. However, another main reason for the later breakthrough time in this case study is a larger average displacement pressure which slows down the leading wave which is a bank of CO_2. Although the differential pressure is not constant all the time, a standard deviation of 0.4 psi indicates that a constant differential pressure of $10.5 \pm 0.4 psi$ is an acceptable assumption for this case study.

5.2.2.2 Total Velocity Profile

Figure 5.7 presents the total velocity as a time dependent parameter, obtained from experiments, in Case study 5.

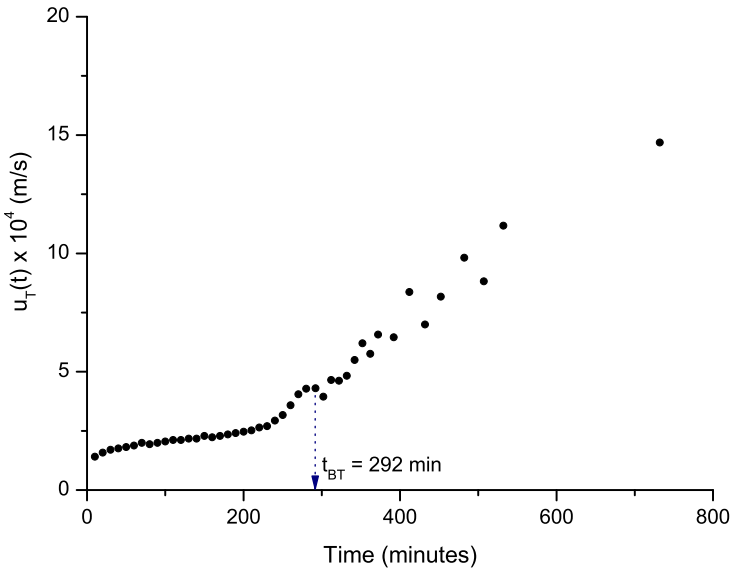

Figure 5.7: Total velocity as a function of time in Case study 5

The data points in Figure 5.7 are calculated using Equation 5.1. As shown in this figure, the total velocity is increasing slowly by starting the gas injection until the breakthrough time. In an intuitive sense, by moving the gas in the forward direction in time, since the pressure drop in the gas segment is much less than that in the oil segment, it is congruent with imposing the same differential pressure over the only oil segment that results in a higher oil velocity at the outlet. Therefore, the oil velocity, or the total velocity, is increasing. After the breakthrough time, however, the total velocity is more controlled by the gas velocity as the low viscosity gas travels faster than the oil inside porous media. Equation 5.1 indicates that the total velocity

highly depends on gas/oil relative permeabilities. Therefore, a poor choice of relative permeability data will lead in analytical simulation results that are far from reality, or experiments indeed. Figure 5.8 presents the analytically simulated total velocity along with experimental results in the same plot.

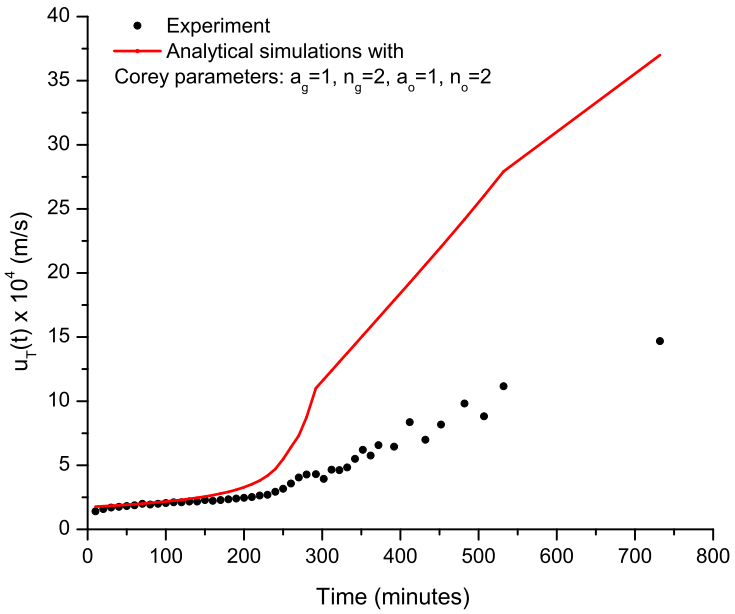

Figure 5.8: Experimental results and analytical results obtained by using basic Corey parameters in Case study 5

In Figure 5.8, basic Corey parameters, $a_g = 1$, $n_g = 2$, $a_o = 1$, and $n_o = 2$, are employed to perform the calculations. Like Case study 4, this indicates that lack of correct relative permeability model could results in large errors in the total velocity as well as breakthrough time calculation. Applying Equations 5.3 and 5.4 reveals that incorrect Corey parameters yields to 12.67% error in calculation of breakthrough time and 36.25% error in the clculation of total velocity profile. Following the same

approach as Case study 4, appropriate relative permeability data are obtained by history matching and the obtained relative permeability data are later validated in Section 5.3.

5.2.2.3 History Matching

The procedure described in Section 5.2.1.3 is followed to match the analytical simulation results to the experiments. Like Case study 4, finding four Corey parameters to match the simulated data to the experimental data could be a time consuming process, as many combination of those four parameters could be used in calculation. In order to save the time in this work, 10,000 combinations of Corey parameters are selected randomly and simulations are conducted in parallel systems to achieve an acceptable match. The results of the history matching process are summarized in Equation 5.7.

$$\begin{aligned} K_{rg} &= 0.51(\frac{S}{0.9})^{1.81} \\ K_{ro} &= 0.94(\frac{0.9-S}{0.9})^{2.87} \end{aligned} \tag{5.7}$$

A plot of relative permeabilities is also provided in Figure 5.9.

Increasing the pressure has changed the properties of the injection gas and the initial oil and therefore, the obtained relative permeabilty curves are different from those obtained in Case study 4. In the Corey model with basic parameters, $a_g = 1$, $n_g = 2$, $a_o = 1$, and $n_o = 2$, it is assumed that the two phases have similar phase behaviour, i.e. at the same saturation values of the two phases have the same relative permeabilities. A closer look at the adjusted parameters in Equation 5.7 reveals that, indeed, the matched parameters are approaching the basic Cory parameters by increasing the pressure. Figure 5.10 shows that total velocity calculated by analytical simulation with adjusted Corey parameters along with the experimental results.

As shown in Figure 5.10, adjusting the Corey parameters, perfectly matches the

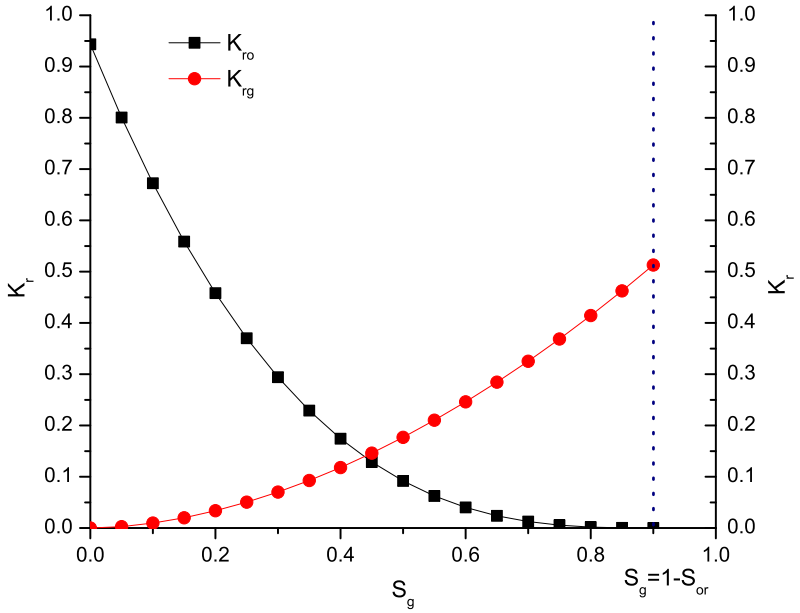

Figure 5.9: Corey relative permeability curves matched with the experimental data (Case study 5)

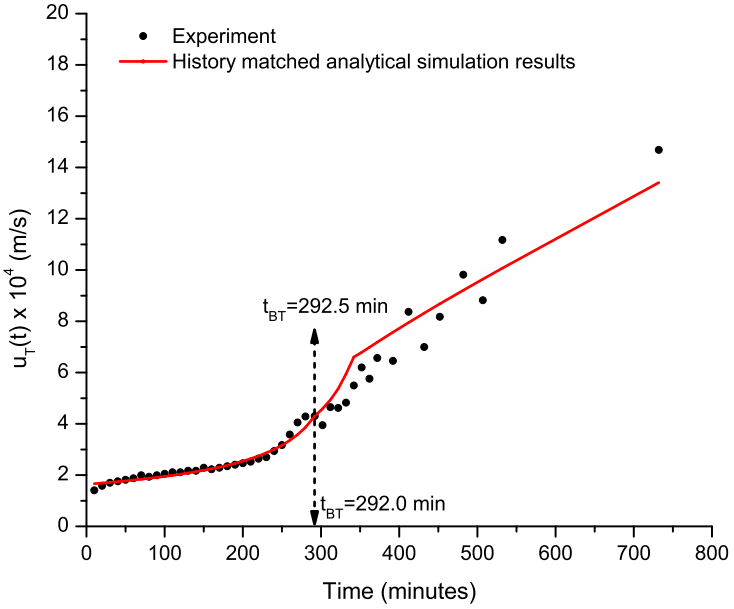

Figure 5.10: Matching of simulation results to the experimental results in Case study 5

gas breakthrough time and leads to a good agreement between analytical simulation and experimental results. The gas breakthrough time is calculated analytically with an error of 0.2 % and the total velocity profile gives an average error of 3.3 %, indicating a good match of experimental and analytical simulation results. As mentioned in Case study 4, the relative permeability data obtained by history matching need to be validated independently. This is done in Section 5.3, for both Case studies 4 and 5.

5.3 Relative Permeability Interpretation with Constant Pressure Boundaries

In this section, a new relative permeability interpretation method based on the generalization of the Buckley-Leverett theory for the systems with constant pressure at the boundaries is applied to determine the gas/oil relative permeability curves. This interpretation method applies analytical solution to fractional flow theory under constant pressure boundary, therefore reducing the need for numerical differentiation and associated errors. this interpretation method was applied for water/oil displacements by Cao et al. [5] and now is extended to immiscible gas flooding systems. In this section, the new interpretation method is applied to Case studies 4 and 5 to validate the relative permeability curves obtained by history matching.

5.3.1 Interpretation Methodology

In one-dimensional gas/oil displacements, the fractional flow model in terms of displacing phase, gas, can be formulated as,

$$\phi \frac{\partial S_g}{\partial t} + u_T(t) \frac{\partial f}{\partial x} = 0, \tag{5.8}$$

where S_g is the gas saturation and f is the fractional flow function in terms of gas defined as,

$$f(S_g) = \frac{\lambda_g}{\lambda_T} - \frac{\lambda_l \lambda_g \Delta\rho}{u_T \lambda_T} \tag{5.9}$$

In Equation 5.9, λ_l is the oil mobility, λ_g is the gas mobility, and $\Delta\rho$ represent the density difference of gas and oil. Under constant differential pressure boundaries, the inlet and outlet pressures are kept constant while the total volumetric flux is a function of time. During the displacement experiment, the breakthrough time is recorded. The breakthrough time (t_S) of a series of saturation points (S_g) are then measured. The corresponding fractional function $f(S_g)$ is then determined based on produced volume of gas and liquid.

In this research the gas/oil relative permeability data are interpreted through constant pressure boundary experiments conducted in the slim tube, as we are going to verify the analytical model by the same experiments. However, in this technique, the end point relative permeabilities, $K_{ro}(S_g = 0)$, $K_{rg}(S_g = 1 - S_{or})$ are calculated from Darcy's law at the beginning and the end of the experiments when the slim tube is saturated with oil and when it contains only residual oil, respectively. The

next saturation point for which we can determine the relative permeabilities is the breakthrough point saturation. Starting from Darcy's law we have the following relations for oil and gas flow rates, assuming that capillary pressure is negligible and displacement happens in a horizontal medium.

$$u_o = -\frac{KK_{ro}}{\mu_o}\frac{\partial p}{\partial x} \tag{5.10}$$

$$u_g = -\frac{KK_{rg}}{\mu_g}\frac{\partial p}{\partial x} \tag{5.11}$$

Fractional flow of gas and oil are defined by Equations 5.12 and 5.13,

$$f_g = \frac{u_g}{u_T} \tag{5.12}$$

and

$$f_o = \frac{u_o}{u_T} = 1 - f_g \tag{5.13}$$

Rearranging Darcy's law and combining them with fractional flow equations results in the following equations for the gas and oil relative permeabilities,

$$K_{ro} = -\frac{u_T(1-f_g)\mu_o}{K\frac{\partial p}{\partial x}} \tag{5.14}$$

and,

$$K_{rg} = -\frac{u_T f_g \mu_g}{K\frac{\partial p}{\partial x}} \tag{5.15}$$

As stated in the previous chapters, u_T is a function of time when constant pressure boundries are applied and the lowest saturation at which the fractional flow of gas and oil are calculated is the gas front saturation at breakthrough time. Hence, Equations 5.14 and 5.15 can be directly applied to find the relative permeabilities at breakthrough time,

$$K_{ro}(S_g^*) = -\frac{u_T(t)[1 - f_g(S_g^*)]\mu_o}{K\frac{\partial p}{\partial x}} \tag{5.16}$$

$$K_{rg}(S_g^*) = -\frac{u_T(t) f_g(S_g^*)\mu_g}{K\frac{\partial p}{\partial x}} \tag{5.17}$$

where, S_g^* is the front gas saturation and is calculated by mass balance at breakthrough time. $f_g(S_g^*)$ is also calculated from experimental data and μ_o and μ_g are oil and gas viscosities, respectively. In order to find the relative permeabilities after the breakthrough time, the recorded volume of produced oil and gas are employed in a mass balance equation to determine the gas saturation at the outlet. If we denote the breakthrough time of saturation S_g, by t_{S_g}, the saturation S_g can be calculated by Equation 5.18,

$$S_g = \overline{S_g} - \frac{1 - f_g(S_g)}{\phi L}\psi(t_{S_g}) \tag{5.18}$$

where, $\psi(t_{S_g}) = \int_0^t u_T(t)dt$ and $\overline{S_g}$ is the average gas saturation in the slim tube and can be calculated by a mass balance equation. $f_g(S_g)$ is determined from experimental data. Therefore, relative permeabilities can be obtained from Equations 5.14 and 5.15 if the the pressure gradient at saturation S, $\frac{\partial p}{\partial x}$ are known. To find the pressure gradient, the location of saturation S_g at breakthrough time is first calculated by

Equation 5.19,

$$x(S_g, t_{BT})^2 + \frac{2u_T(t_{S_g})(t_{S_g} - t_{BT})L}{\psi(t_{BT})} x(S_g, t_{BT}) - L^2 = 0 \tag{5.19}$$

Once the $x(S_g, t_{BT})$ is known, $f_g^{'}(S_g)$ can be determined from the following equation,

$$f_g^{'}(S_g) = \frac{x(S_g, t_{BT})\phi}{\psi(t_{BT})} \tag{5.20}$$

then the pressure at the location of saturation S_g at breakthrough time is,

$$p(x(S_g, t_{BT})) = p_{in} - \frac{\Delta p f^{'}(S_g)\psi(t_{BT})}{\phi L} \tag{5.21}$$

Equation 5.21 can be used to calculate the pressure gradient by numerical differentiation.

5.3.2 Results

The procedure explained in Section 5.3, is applied to determine the gas/oil relative permeabilities in Case studies 4 and 5. Figures 5.11 and 5.12 present the relative permeability data obtained from the new interpretation method for Case studies 4 and 5, respectively. The relative permeabilities at the end points are directly calculated from Darcy's law. It was expected to achieve $K_{ro} = 1$ at the start of experiments, i.e. $S_g = 0$, however, in Figures 5.11 and 5.12 it is observed that the relative permeability at both cases was measured to be less than 1. One reason for this behaviour could be not fully saturation of the slim tube due to trap of bubbles. Another reason for this behaviour could be the change of pore size distribution as the connection of the set

up to the vacuum pump, and flow of gas and oil in the system could potentially move the particles around and change the absolute permeability. In Figures 5.13 and 5.14 the relative permeability results from the history matching are shown for the same systems. A good agreement is observed between the results obtained from the two methods. The difference between the results could be because of the violation of the main assumption of constant differential pressure over the slim tube.

Figures 5.13 and 5.14 compare the relative permeabilities obtained from history matching and the new interpretation method for Case studies 4 and 5, respectively. Both figures show that the new interpretation method overestimates the history matched relative permeabilities to a small degree. However, the relative permeabilities obtained from the new method can now be employed in the analytical simulations to determine the total velocity profiles. First, they need to be converted into the Corey models. Figures 5.15 and 5.16 display the Corey-type curves fitted to data obtained by the new method. Nonlinear regression analysis is applied for the curve fitting. Equations 5.22 and 5.23 represent the Corey-type models fitted to the new method's data.

$$\begin{aligned} K_{rg} &= 0.55(\frac{S}{0.9})^{1.21} \\ K_{ro} &= 0.92(\frac{0.9-S}{0.9})^{2.92} \end{aligned} \tag{5.22}$$

$$\begin{aligned} K_{rg} &= 0.56(\frac{S}{0.9})^{1.54} \\ K_{ro} &= 0.95(\frac{0.9-S}{0.9})^{2.35} \end{aligned} \tag{5.23}$$

Figures 5.17 and 5.18 indicate the total velocity profiles along with the experimental data and results obtained by history matching models. As discussed earlier, the new

method is slightly overestimating the relative permeabilities. Therefore, the overestimation of the corresponding total velocities were expected. The total error calculated by Equation 5.5 are 15.2 % and 11.6 % for Case studies 4 and 5, respectively.

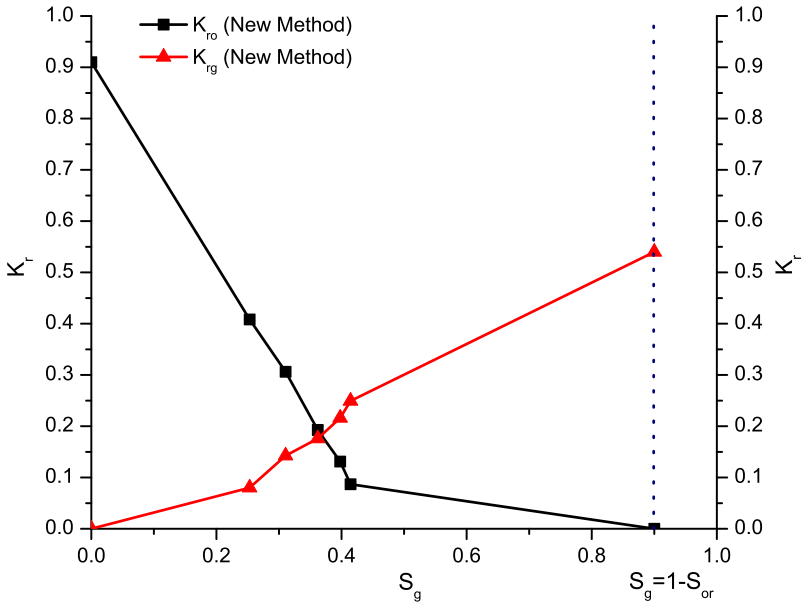

Figure 5.11: Relative permeabilities obtained by new interpretation method from constant pressure boundary experiments (Case study 4)

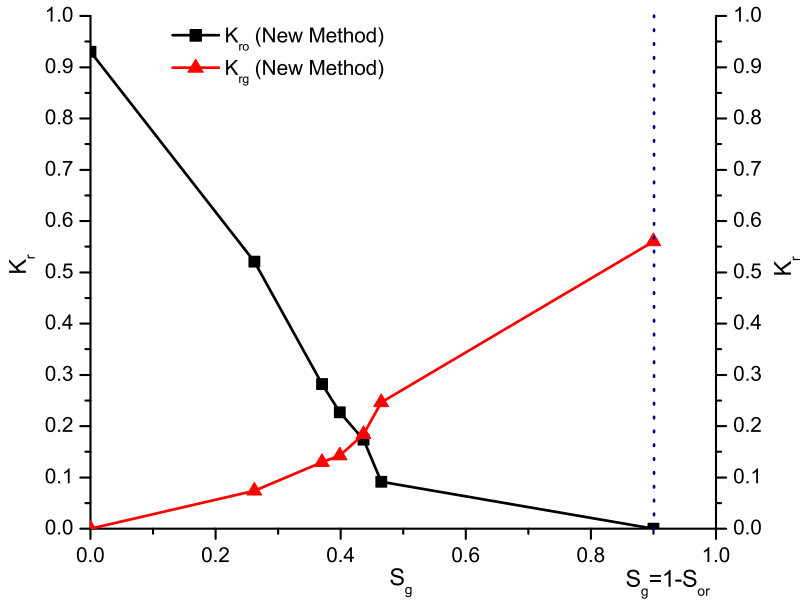

Figure 5.12: Relative permeabilities obtained by new interpretation method from constant pressure boundary experiments (Case study 5)

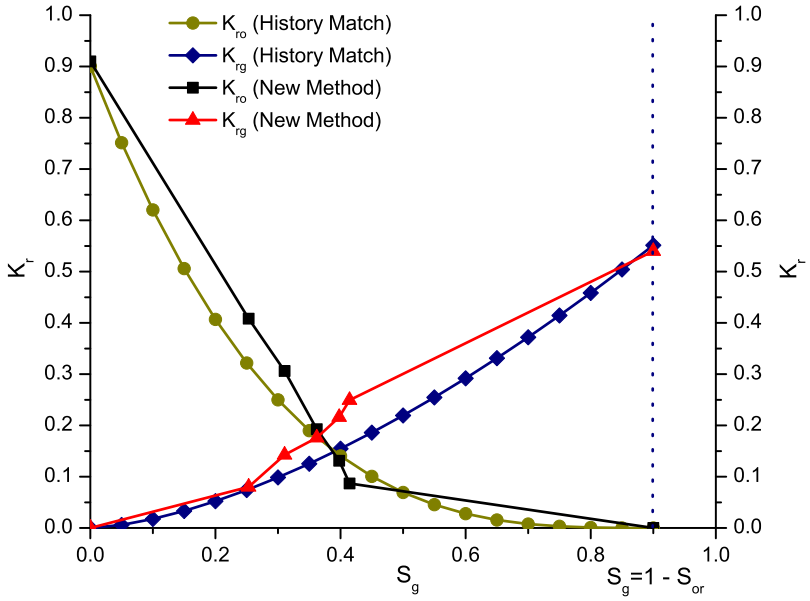

Figure 5.13: Comparison of relative permeability curves obtained by new interpretation method and history matching (Case study 4)

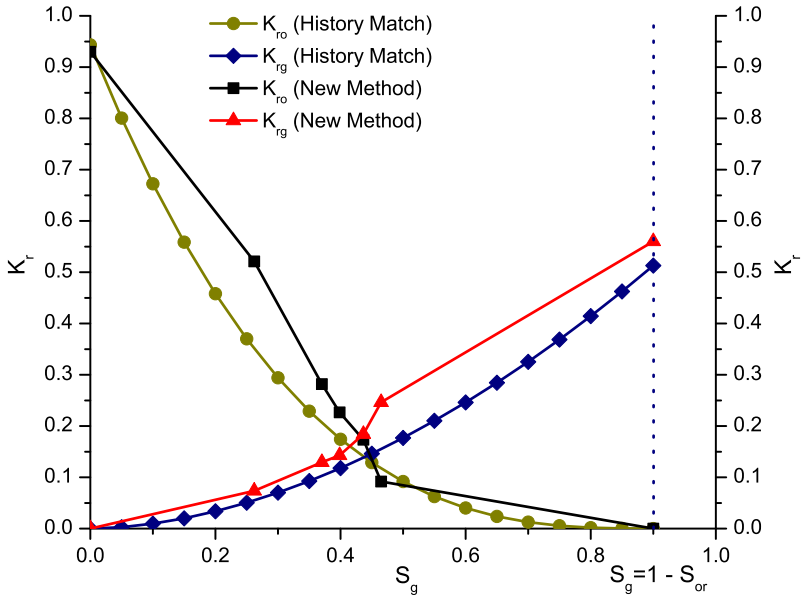

Figure 5.14: Comparison of relative permeability curves obtained by new interpretation method and history matching (Case study 5)

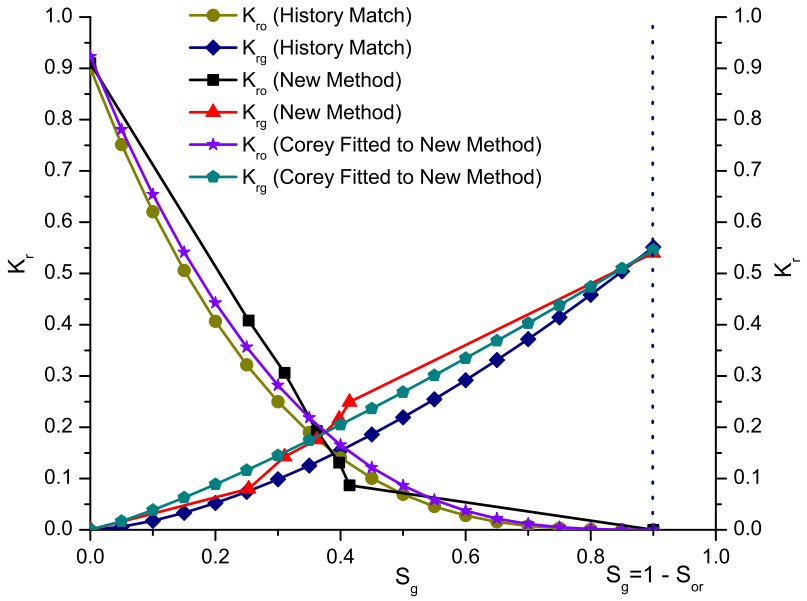

Figure 5.15: Corey model fitted to the relative permeability data obtained by new method (Case study 4)

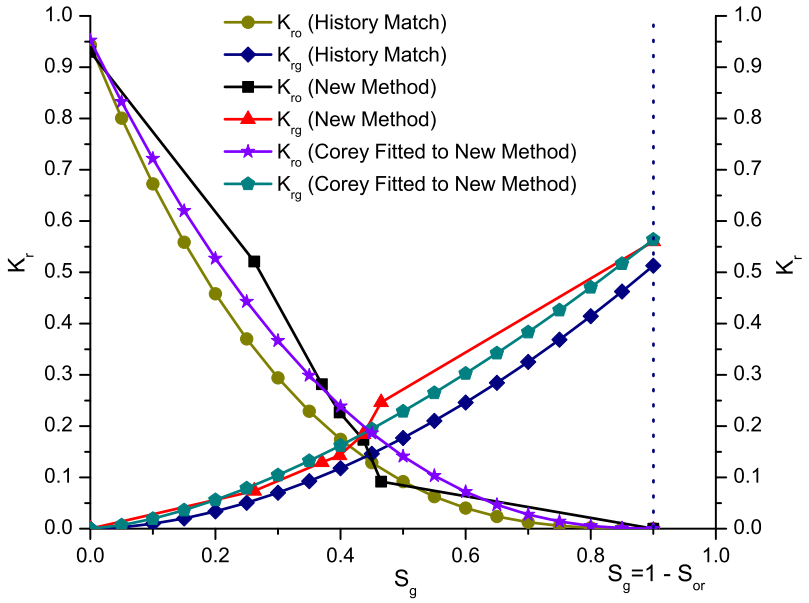

Figure 5.16: Corey model fitted to the relative permeability data obtained by new method (Case study 5)

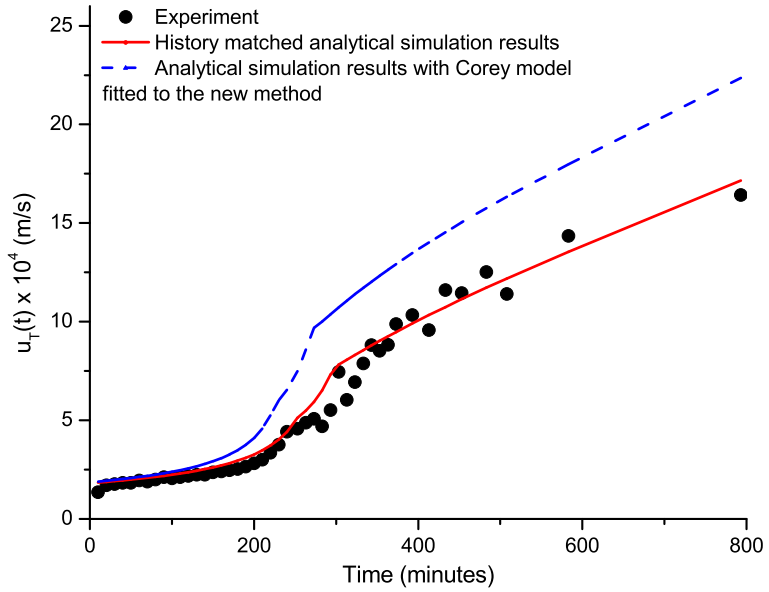

Figure 5.17: Total velocity profile with Corey model fitted to the relative permeability obtained by the new method (Case study 4)

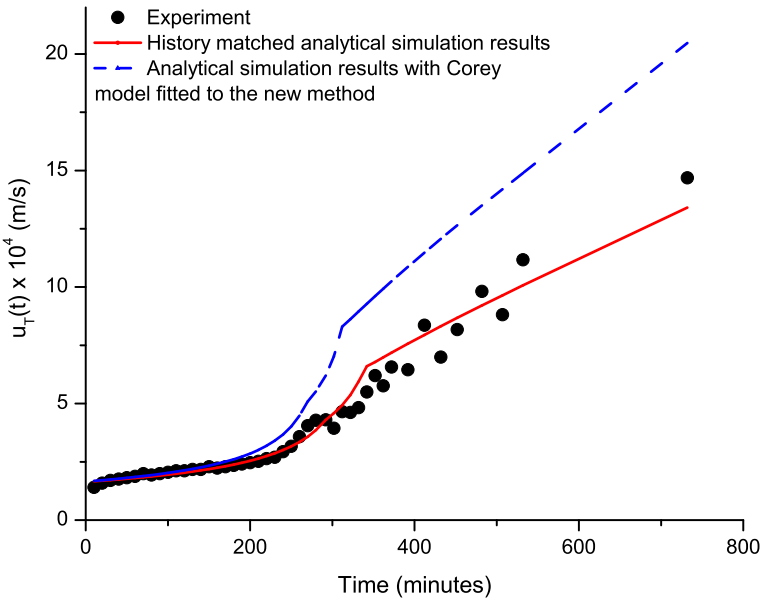

Figure 5.18: Total velocity profile with Corey model fitted to the relative permeability obtained by the new method (Case study 5)

5.4 Discussion

In Chapter 5, two practical gas/oil displacement Case studies were investigated under constant injection and production pressures. Satndard deviations of 0.3 and 0.4 psi, in Case studies 4 and 5, indicates that constant differential pressure is a fair assumption for the two experiments. Analytical solutions were calculated first and the corresponding experiments were then conducted in a slim tube set up. Comparison of the analytical and experimental results shows that the analytical solution agrees with the experimental results if reliable relative permeability data are used for the analytical simulation. While using basic Corey model, $a_g = 1$, $n_g = 2$, $a_o = 1$, and n_o leads to error of 11.9 % and 12.7 % in calculation of breakthrough time. Basic Corey parameters also overestimates the total velocity with average error of 45.0 % and 36.3

% in Case studies 4 and 5, respectively. The significant errors in calculation of gas breakthrough time and the total velocity arises from the fact that the basic Corey parameters used to model the relative permeability data do not correctly represent the gas/oil relative permeability data in the slim tube. History matching of analytical simulation results to experimental results by adjusting the Corey parameters shows the remarkable effect of relative permeability data on the analytical simulation results. Employing the history matched relative permeabilities results in 0.3 % and 0.2 % in calculation of gas breakthrough time, and average error of 5.0 % and 3.3 % in calculation of the total velocity. However, the history matched relative permeability data are then validated through a novel interpretation approach of experimental data. The acquired relative permeability curves from the new interpretation method overestimate the relative permeabilities obtained from history matching by a small degree. The newly interpreted relative permeability data lead to 10.6 % and 8.0 % error in calculation of gas breakthrough time, 17.4 % and 13.3 % error in calculation of total velocity. The errors are rise from the overestimation of gas and oil relative permeabilities. In fact, the errors reflect the deviation of experiment condition from the ideal condition assumed in the analytical simulations. Sometimes, during the experiments, a slug flow is created in the slim tube which violates the simultaneous flow of oil and gas, therefore, leading to wrong relative permeability data. The constant pressure boundary condition is also sometimes violated while it gets more severe after the gas breakthrough. It is also likely that, in the real world experiments, the flow is not strictly one-dimensional in the inlet region. This could also create some of the difference between the analytical solution and the experimental results.

Chapter 6

Summary and Conclusions

In this research, for the first time, gas/oil displacements with constant pressure boundaries are investigated mathematically and experimentally. Applying a new boundary condition, constant injection and production pressures, to the mathematical and experimental study of multi-component gas/oil displacements has never been performed in the literature. This is the the main contribution of the author throughout the research. Mathematically, a novel extension of the classic Buckley-Leverett theory is applied to solve multi-component gas/oil displacement problems with constant pressure boundaries in a one-dimensional, dispersion-free medium. Unlike previously done constant flux systems, in which total flux is constant both in space and time, the total flux is found to be a function of time in problems with constant pressure boundaries. Using the novel analytical technique, the breakthrough time of different waves are determined in a five-component gas/oil displacement and the total flux is obtained as a function of time, considering volume change upon mixing. Then, the MMP is calculated through an analytical method. Experimentally, a two-component gas mixture

and a three-component synthetic oil are used in slim tube experiments to validate the MMP calculation and confirm the new analytical model. Slim tube tests are first conducted to determine the Minimum Miscibility Pressure (MMP). Then, for the first time, constant pressure boundaries displacement of the oil by gas is performed in the same slim tube to capture a one-dimensional, dispersion-free displacement. The gas breakthrough time is recorded and effluent volume is evaluated to determine the total velocity as a function of time. In order to compare the analytical simulation results with the experimental results, correct input data must be entered into the simulator. The only uncertain data, in the simulation process, is the relative permeability of the oil and gas. History matching of the total flux and the breakthrough time, by adjusting the Corey parameters to the experimental data, is performed to determine reliable Corey-type relative permeability curves. Alternatively, in order to confirm the history matched relative permeabilities, a novel interpretation method is applied to determine the relative permeability curves from unsteady-state constant pressure boundary experiments. The results indicate that the analytical constant pressure boundaries' solution agrees with the experimental results if an appropriate relative permeability model is selected for the simultaneous flow of oil and gas in the slim tube. Differences between the analytical model and experimental results for the total velocity and gas breakthrough time are on the order of 10 - 15 %, when relative permeability data from the new interpretation method are used, and 0 - 5 %, when the relative permeability data from the history matching are used. Analytical simulation also indicates that ignoring the effect of volume change upon mixing, overestimates the gas breakthrough time by 30-40 % error. However, the results show that the assumptions made in the new analytical technique capture the rock/fluid and fluid/fluid

interactions in the practical cases. The results also indicate that the new constant pressure boundary extension of Buckley Leverett gives fast and acceptable solutions compared to expensive and time consuming experiments. Finally, comparison of the calculated MMP by Jessens's method with the experimentally measured MMP illustrated the robustness of this analytical method. Less than 1 % error indicates that Jessen's method effectively captures the gas/oil interaction in miscible displacements.

Future Work

In this research, theory of multi-component gas/oil displacements with constant pressure boundaries is examined using a two-component injection gas and a three-component synthetic oil. The fluids used in this research are far from real fluids in the oil reservoirs. A valuable future research could be using crude oil and multi-component hydrocarbon gas in the displacement process. Using real field samples enables us to examine the impact of grouping components on the results and, more importantly, correlate the modeling/lab data to the oil fields.

Finding the optimal gas richness to minimize the operational costs in the oil field, economical analysis, investigation of the effect of the MMP and its uncertainties on actual oil recovery and field decisions is also a practical research topic that links the universities to the industry.

Bibliography

[1] F. O. Alpak, L. W. Lake, S. M. Embid, et al. Validation of a modified carman-kozeny equation to model two-phase relative permeabilities. In *SPE Annual Technical Conference and Exhibition*. Society of Petroleum Engineers, 1999.

[2] C. BrooksRH. Hydraulic properties of porous media. *Colorado State University, Hydro Paper*, 3:27, 1964.

[3] D. Bryant, T. Monger, et al. Multiple-contact phase behavior measurement and application with mixtures of co2 and highly asphaltic crude. *SPE reservoir engineering*, 3(02):701–710, 1988.

[4] S. E. Buckley, M. Leverett, et al. Mechanism of fluid displacement in sands. *Transactions of the AIME*, 146(01):107–116, 1942.

[5] J. Cao, L. A. James, and T. E. Johansen. Determination of two phase relative permeability from core floods with constant pressure boundaries. In *Society of Core Analysis Symposium, Avignon, France*, 2014.

[6] G. L. Chierici et al. Novel relations for drainage and imbibition relative permeabilities. *Society of Petroleum Engineers Journal*, 24(03):275–276, 1984.

[7] R. Christiansen. Method of determining the minimum level of enrichment for a miscible gas flood, Sept. 9 1986. US Patent 4,610,160.

[8] A. T. Corey et al. The interrelation between gas and oil relative permeabilities. *Producers monthly*, 19(1):38–41, 1954.

[9] A. T. Corey, C. Rathjens, et al. Effect of stratification on relative permeability. *Journal of Petroleum Technology*, 8(12):69–71, 1956.

[10] A. Danesh. *PVT and phase behaviour of petroleum reservoir fluids*, volume 47. Elsevier, 1998.

[11] B. Dindoruk, R. Johns, and F. Orr. Analytical solution for four component gas displacements with volume change on mixing. In *ECMOR III-3rd European Conference on the Mathematics of Oil Recovery*, 1992.

[12] B. Eakin, F. Mitch, et al. Measurement and correlation of miscibility pressures of reservoir oils. In *SPE annual technical conference and exhibition*. Society of Petroleum Engineers, 1988.

[13] J. M. Ekundayo, S. G. Ghedan, et al. Minimum miscibility pressure measurement with slim tube apparatus-how unique is the value? In *SPE Reservoir Characterization and Simulation Conference and Exhibition*. Society of Petroleum Engineers, 2013.

[14] A. Elsharkawy, F. Poettmann, R. Christiansen, et al. Measuring minimum miscibility pressure: slim-tube or rising-bubble method? In *SPE/DOE Enhanced Oil Recovery Symposium*. Society of Petroleum Engineers, 1992.

[15] L. C. Evans. Partial differential equations and monge-kantorovich mass transfer. *Current developments in mathematics*, 1997(1):65–126, 1997.

[16] O. Glaso et al. Generalized minimum miscibility pressure correlation (includes associated papers 15845 and 16287). *Society of Petroleum Engineers Journal*, 25(06):927–934, 1985.

[17] M. A. Grella, J. Callard, et al. Interrelating production analysis with pore scale structure in the bakken reservoir. In *SPE Oklahoma City Oil and Gas Symposium*. Society of Petroleum Engineers, 2017.

[18] C. L. Hearn, C. H. Whitson, et al. Evaluating miscible and immiscible gas injection in the safah field, oman. In *SPE Reservoir Simulation Symposium*. Society of Petroleum Engineers, 1995.

[19] L. Høier. *Miscibility variations in compositionally grading petroleum reservoirs*. PhD thesis, PhD thesis, Norwegian U. of Science and Technology, Trondheim, Norway, 1997.

[20] L. Holm, V. Josendal, et al. Mechanisms of oil displacement by carbon dioxide. *Journal of petroleum Technology*, 26(12):1–427, 1974.

[21] M. K. Hubbert et al. Darcy's law and the field equations of the flow of underground fluids. 1956.

[22] J.-N. Jaubert, L. Arras, E. Neau, and L. Avaullee. Properly defining the classical vaporizing and condensing mechanisms when a gas is injected into a crude oil. *Industrial & engineering chemistry research*, 37(12):4860–4869, 1998.

[23] J.-N. Jaubert, L. Wolff, E. Neau, and L. Avaullee. A very simple multiple mixing cell calculation to compute the minimum miscibility pressure whatever the displacement mechanism. *Industrial & engineering chemistry research*, 37(12):4854–4859, 1998.

[24] F. Jensen and M. Michelsen. Calculation of first contract and multiple contact minimum miscibility pressures. *In Situ;(USA)*, 14(1), 1990.

[25] K. Jessen. Effective algorithms for the study of miscible gas injection processes. *PhD Diss., Technical University of Denmark, Lyngby, Denmark (March 2000)*, 2000.

[26] K. Jessen, M. L. Michelsen, and E. H. Stenby. Global approach for calculation of minimum miscibility pressure. *Fluid Phase Equilibria*, 153(2):251–263, 1998.

[27] K. Jessen, F. M. Orr, et al. On ift measurements to estimate minimum miscibility pressures. In *SPE Annual Technical Conference and Exhibition*. Society of Petroleum Engineers, 2007.

[28] T. Johansen, Y. Wang, F. M. Orr, and B. Dindoruk. Four-component gas/oil displacements in one dimension: part i: global triangular structure. *Transport in porous media*, 61(1):59–76, 2005.

[29] T. Johansen and R. Winther. The solution of the riemann problem for a hyperbolic system of conservation laws modeling polymer flooding. *SIAM journal on mathematical analysis*, 19(3):541–566, 1988.

[30] T. Johansen and R. Winther. The riemann problem for multicomponent polymer flooding. *SIAM Journal on Mathematical Analysis*, 20(4):908–929, 1989.

[31] T. Johansen and R. Winther. Mathematical and numerical analysis of a hyperbolic system modeling solvent flooding. In *ECMOR II-2nd European Conference on the Mathematics of Oil Recovery*, 1990.

[32] T. E. Johansen and L. A. James. Solution of multi-component, two-phase riemann problems with constant pressure boundaries. *Journal of Engineering Mathematics*, 96(1):23–35, 2016.

[33] J. P. Johnson, J. S. Pollin, et al. Measurement and correlation of co2 miscibility pressures. In *SPE/DOE enhanced oil recovery symposium*. Society of Petroleum Engineers, 1981.

[34] T. LaForce, K. Jessen, and F. Orr. Four-component gas/water/oil displacements in one dimension: Part i. structure of the conservation law. *Transport in Porous Media*, 71(2):199–216, 2008.

[35] T. LaForce and R. T. Johns. Analytical solutions for surfactant-enhanced remediation of nonaqueous phase liquids. *Water resources research*, 41(10), 2005.

[36] T. C. LaForce, Y. Cinar, R. T. Johns, F. M. Orr Jr, et al. Experimental confirmation for analytical composition routes in three-phase partially miscible flow. *SPE Journal*, 15(01):160–170, 2010.

[37] T. C. LaForce, R. T. Johns, et al. Composition routes for three-phase partially miscible flow in ternary systems. *SPE Journal*, 10(02):161–174, 2005.

[38] P. D. Lax. Hyperbolic systems of conservation laws ii. *Communications on pure and applied mathematics*, 10(4):537–566, 1957.

[39] R. Metcalfe, D. Fussell, J. Shelton, et al. A multicell equilibrium separation model for the study of multiple contact miscibility in rich-gas drives. *Society of Petroleum Engineers Journal*, 13(03):147–155, 1973.

[40] R. Metcalfe, L. Yarborough, et al. The effect of phase equilibria on the co2 displacement mechanism. *Society of Petroleum Engineers Journal*, 19(04):242–252, 1979.

[41] I. Mihcakan, F. Poettmann, and R. Christiansen. Apparatus and method for determining minimum miscibility pressure, Apr. 9 1996. US Patent 5,505,074.

[42] W. W. Monroe, M. K. Silva, L. Larson, F. M. Orr Jr, et al. Composition paths in four-component systems: effect of dissolved methane on 1d co2 flood performance. *SPE Reservoir Engineering*, 5(03):423–432, 1990.

[43] E. Neau, L. Avaullée, and J. Jaubert. A new algorithm for enhanced oil recovery calculations. *Fluid Phase Equilibria*, 117(1):265–272, 1996.

[44] A. Nouar and D. Flock. Parametric analysis on the determination of the minimum miscibility pressure in slim tube displacements. *Annual CIM Petroleum Society;()*, 83, 1983.

[45] F. M. Orr. *Theory of gas injection processes*. Tie-Line Publications, 2007.

[46] F. M. Orr and K. Jessen. An analysis of the vanishing interfacial tension technique for determination of minimum miscibility pressure. *Fluid phase equilibria*, 255(2):99–109, 2007.

[47] F. Orr Jr, M. Silva, C. Lien, M. Pelletier, et al. Laboratory experiments to evaluate field prospects for co2 flooding. *Journal of Petroleum Technology*, 34(04):888–898, 1982.

[48] K. Pederson, J. Fjellerup, P. Thomassen, A. Fredenslund, et al. Studies of gas injection into oil reservoirs by a cell-to-cell simulation model. In *SPE Annual Technical Conference and Exhibition*. Society of Petroleum Engineers, 1986.

[49] D.-Y. Peng and D. B. Robinson. A new two-constant equation of state. *Industrial & Engineering Chemistry Fundamentals*, 15(1):59–64, 1976.

[50] S. Pongpitak. *Interaction of phase behavior with multiphase flow in porous media*. PhD thesis, New Mexico Institute of Mining and Technology, 1980.

[51] K. A. Rahmataba. *Advances in Calculation of Minimum Miscibility Pressure*. PhD thesis, University of Texas, 2011.

[52] D. N. Rao. A new technique of vanishing interfacial tension for miscibility determination. *Fluid phase equilibria*, 139(1-2):311–324, 1997.

[53] B. Riemann. Sur les hypothèses qui servent de fondement à la géométrie. *Annali di Matematica Pura ed Applicata (1867-1897)*, 3(1):309–326, 1869.

[54] W. Rutherford et al. Miscibility relationships in the displacement of oil by light hydrocarbons. *Society of Petroleum Engineers Journal*, 2(04):340–346, 1962.

[55] H. Sebastian, D. Lawrence, et al. Nitrogen minimum miscibility pressures. In *SPE/DOE Enhanced Oil Recovery Symposium*. Society of Petroleum Engineers, 1992.

[56] H. Sebastian, R. Wenger, T. Renner, et al. Correlation of minimum miscibility pressure for impure co2 streams. *Journal of Petroleum Technology*, 37(11):2–076, 1985.

[57] W. A. Strauss. *Partial differential equations*. John Wiley & Sons New York, NY, USA, 1992.

[58] F. Thomas, X. Zhou, D. Bennion, D. Bennion, et al. A comparative study of rba, px, multicontact and slim tube results. *Journal of Canadian Petroleum Technology*, 33(02), 1994.

[59] C. Wachmann et al. A mathematical theory for the displacement of oil and water by alcohol. *Society of Petroleum Engineers Journal*, 4(03):250–266, 1964.

[60] Y. Wang, B. Dindoruk, T. Johansen, and F. M. Orr. Four-component gas/oil displacements in one dimension: part ii: analytical solutions for constant equilibrium ratios. *Transport in porous media*, 61(2):177–192, 2005.

[61] Y. Wang and F. M. Orr. Analytical calculation of minimum miscibility pressure. *Fluid Phase Equilibria*, 139(1):101–124, 1997.

[62] Y. Wang and F. M. Orr. Calculation of minimum miscibility pressure. *Journal of petroleum science and engineering*, 27(3):151–164, 2000.

[63] H. Welge, E. F. Johnson, S. Ewing Jr, F. Brinkman, et al. The linear displacement of oil from porous media by enriched gas. *Journal of Petroleum Technology*, 13(08):787–796, 1961.

[64] H. J. Welge et al. A simplified method for computing oil recovery by gas or water drive. *Journal of Petroleum Technology*, 4(04):91–98, 1952.

[65] R. Wu, J. Batycky, et al. Evaluation of miscibility from slim tube tests. *Journal of Canadian Petroleum Technology*, 29(06), 1990.

[66] W. Yellig, R. Metcalfe, et al. Determination and prediction of co2 minimum miscibility pressures (includes associated paper 8876). *Journal of Petroleum Technology*, 32(01):160–168, 1980.

[67] D. Zhou, F. M. Orr Jr, et al. An analysis of rising bubble experiments to determine minimum miscibility pressures. In *SPE Annual Technical Conference and Exhibition*, pages 883–892. Society of Petroleum Engineers, 1995.

[68] A. Zick et al. A combined condensing/vaporizing mechanism in the displacement of oil by enriched gases. In *SPE annual technical conference and exhibition*. Society of Petroleum Engineers, 1986.

Appendix A

Slim Tube Experimental Data

Table A.1: Slim tube data at $p = 1230\,psi$

#	**Time (min)**	$\mathbf{V_{injected}}$ **(PV)**	$\mathbf{V_{oil}}$ **SC (cc)**	$\mathbf{V_{oil}}$ **RC (cc)**	$\mathbf{V_{gas}}$ **SC (cc)**	**Temp (°C)**	$\mathbf{C_6}$ **(%)**	$\mathbf{C_{10}}$ **(%)**	$\mathbf{C_{16}}$ **(%)**
0	0	0.00	0	0.0000	0.0	97.88	0.00	0.00	0.00
1	25	0.05	7.9	8.4443	0.0	97.89	18.37	49.81	31.82
2	50	0.10	13.6	14.5370	0.0	97.91	18.52	49.67	31.81
3	75	0.15	19.8	21.1642	0.0	97.95	18.81	49.45	31.74
4	100	0.20	27.5	29.3948	0.0	97.96	18.75	49.32	31.93
5	125	0.25	34.9	37.3046	0.0	97.98	18.66	49.47	31.87
6	150	0.30	42.3	45.2145	0.0	98.01	18.69	49.53	31.78
7	175	0.35	49.1	52.4830	0.0	98.00	18.54	49.39	32.07
8	200	0.40	56.3	60.1791	0.0	98.02	18.89	49.92	31.19
9	225	0.45	64.1	68.5165	0.0	98.01	18.91	49.56	31.53
10	250	0.50	72.7	77.7090	0.0	97.99	18.88	49.64	31.48
11	275	0.55	80.3	85.8327	0.0	97.97	18.94	49.71	31.35
12	300	0.60	88.0	94.0632	0.0	97.96	18.79	49.59	31.62
BT	313	0.63	91.8	98.1250	0.0	97.94	18.47	49.55	31.98
13	325	0.65	95.7	102.2937	0.0	97.93	18.39	49.63	31.98
14	350	0.70	103.1	110.2036	0.0	97.91	18.46	49.48	32.06
15	375	0.75	111.1	118.7548	15.1	97.88	18.84	49.63	31.53
16	400	0.80	120.0	128.2680	105.4	97.85	18.93	49.57	31.50
17	425	0.85	132.7	141.8430	534.6	97.84	18.78	49.38	31.84
18	450	0.90	140.7	150.3942	737.9	97.82	18.69	49.82	31.49
19	475	0.95	146.0	156.0594	1234.1	97.84	18.76	49.95	31.29
20	500	1.00	151.5	161.9384	2002.9	97.87	17.72	50.77	31.51
21	525	1.05	157.6	168.4586	1882.5	97.87	16.79	51.48	31.73
22	550	1.10	163.4	174.6583	2650.4	97.91	16.51	52.12	31.37
23	575	1.15	164.9	176.2616	2522.6	97.92	14.39	53.94	31.67
24	600	1.20	165.9	177.3305	3606.8	97.94	10.08	56.23	33.69

Table A.2: Slim tube data at $p = 1800\,psi$

#	**Time (min)**	$\mathbf{V_{injected}}$ **(PV)**	$\mathbf{V_{oil}}$ **SC (cc)**	$\mathbf{V_{oil}}$ **RC (cc)**	$\mathbf{V_{gas}}$ **SC (cc)**	**Temp (°C)**	$\mathbf{C_6}$ **(%)**	$\mathbf{C_{10}}$ **(%)**	$\mathbf{C_{16}}$ **(%)**
0	0	0.00	0.0	0.0000	0.0	98.01	0.00	0.00	0.00
1	25	0.05	3.8	4.0436	0.0	97.78	18.35	49.79	31.87
2	50	0.10	9.1	9.6833	0.0	97.82	18.54	49.66	31.80
3	75	0.15	16.0	17.0256	0.0	97.85	18.83	49.54	31.73
4	100	0.20	23.6	25.1128	0.0	97.89	18.48	49.54	31.61
5	125	0.25	32.2	34.2640	0.0	97.91	18.63	49.58	31.80
6	150	0.30	41.3	43.9473	0.0	97.92	18.65	49.60	31.75
7	175	0.35	50.6	53.8435	0.0	97.93	18.85	49.54	31.61
8	200	0.40	59.6	63.4204	0.0	97.93	18.78	49.57	31.65
9	225	0.45	68.5	72.8909	0.0	97.94	18.71	18.56	31.73
10	250	0.50	78.1	83.1062	0.0	97.92	18.76	49.61	31.63
11	275	0.55	87.9	93.5344	0.0	97.91	18.83	49.59	31.58
12	300	0.60	97.4	103.6433	0.0	97.92	18.85	49.53	31.62
13	325	0.65	107.0	113.8587	0.0	97.92	18.93	49.55	31.53
BT	331	0.66	108.9	115.8805	0.0	97.93	18.92	49.50	31.59
14	350	0.70	116.4	123.8612	0.0	97.94	18.97	49.52	31.51
15	375	0.75	125.5	133.5445	11.5	97.95	18.91	49.57	31.52
16	400	0.80	142.8	151.9534	23.0	97.94	18.99	49.48	31.53
17	425	0.85	153.6	163.4457	218.8	97.92	18.74	49.61	31.65
18	450	0.90	167.2	177.9175	1105.6	97.93	18.37	49.86	31.78
19	475	0.95	177.0	188.3457	921.3	97.95	18.48	49.81	31.71
20	500	1.00	183.8	195.5815	1865.7	97.94	17.62	50.28	32.10
21	525	1.05	191.8	204.0943	2084.5	97.91	17.72	50.25	32.04
22	550	1.10	197.4	210.0533	3581.7	97.88	16.62	51.03	32.34
23	575	1.15	198.4	211.1174	4019.3	97.87	11.21	54.61	34.19
24	600	1.20	199.4	212.1815	5608.6	97.86	9.76	56.44	33.81

Table A.3: Slim tube data at $p = 2600\,psi$

#	**Time (min)**	$\mathbf{V_{injected}}$ **(PV)**	$\mathbf{V_{oil}}$ **SC (cc)**	$\mathbf{V_{oil}}$ **RC (cc)**	$\mathbf{V_{gas}}$ **SC (cc)**	**Temp (°C)**	$\mathbf{C_6}$ **(%)**	$\mathbf{C_{10}}$ **(%)**	$\mathbf{C_{16}}$ **(%)**
0	0	0.00	0.0	0.0000	0.0	98.04	0.00	0.00	0.00
1	25	0.05	4.4	4.6561	0.0	98.01	18.18	49.84	31.98
2	50	0.10	11.2	7.1958	0.0	98.02	18.65	49.60	31.75
3	75	0.15	20.0	9.3122	0.0	98.00	18.49	49.62	31.88
4	100	0.20	29.6	10.1587	0.0	97.99	18.58	49.59	31.82
5	125	0.25	39.9	10.8995	0.0	97.97	18.54	49.63	31.84
6	150	0.30	50.7	11.4286	0.0	97.96	18.63	49.58	31.79
7	175	0.35	61.2	11.1111	0.0	97.98	18.61	49.66	31.73
8	200	0.40	71.5	10.8995	0.0	97.95	18.89	49.53	31.58
9	225	0.45	81.8	10.8995	0.0	97.93	18.53	49.62	31.84
10	250	0.50	92.2	11.0053	0.0	97.94	18.85	49.55	31.60
11	275	0.55	102.6	11.0053	0.0	97.95	18.82	49.59	31.59
12	300	0.60	112.7	10.6878	0.0	97.95	18.87	49.55	31.59
13	325	0.65	123.0	10.8995	0.0	97.96	18.90	49.55	31.55
14	350	0.70	133.2	10.7936	0.0	97.97	18.94	49.49	31.57
BT	359	0.72	137.1	4.1270	0.0	97.97	19.01	49.50	31.49
15	375	0.75	143.3	6.5608	0.0	97.96	18.76	49.61	31.63
16	400	0.80	153.6	10.8995	0.0	97.95	18.97	49.49	31.54
17	425	0.85	164.2	11.2169	17.2	97.93	18.65	49.66	31.69
18	450	0.90	177.4	13.9682	378.1	97.91	18.48	49.81	31.71
19	475	0.95	190.4	13.7566	807.9	97.89	17.04	50.59	32.37
20	500	1.00	201.0	11.2169	2286.5	97.88	17.37	50.55	32.07
21	525	1.05	211.9	11.5344	1564.3	97.86	15.53	52.06	32.41
22	550	1.10	219.6	8.1481	4538.7	97.87	14.37	52.98	32.65
23	575	1.15	221.7	2.2222	5484.2	97.89	10.28	55.60	34.11
24	600	1.20	222.8	1.1640	9833.8	97.91	9.82	56.47	33.70

Table A.4: Slim tube data at $p = 3260\,psi$

#	**Time (min)**	$\mathbf{V_{injected}}$ **(PV)**	$\mathbf{V_{oil}}$ **SC (cc)**	$\mathbf{V_{oil}}$ **RC (cc)**	$\mathbf{V_{gas}}$ **SC (cc)**	**Temp (°C)**	$\mathbf{C_6}$ **(%)**	$\mathbf{C_{10}}$ **(%)**	$\mathbf{C_{16}}$ **(%)**
0	0	0.00	0.0	0.0000	0.0	98.01	0.00	0.00	0.00
1	25	0.05	5.2	5.4782	0.0	97.81	18.31	49.57	32.12
2	50	0.10	10.5	11.0618	0.0	97.82	18.49	49.62	31.89
3	75	0.15	17.2	18.1202	0.0	97.84	18.57	49.71	31.72
4	100	0.20	25.4	26.7589	0.0	97.85	18.48	49.63	31.89
5	125	0.25	34.2	36.0297	0.0	97.88	18.61	49.45	31.94
6	150	0.30	43.7	46.0380	0.0	97.90	18.62	49.38	32.00
7	175	0.35	53.7	56.5730	0.0	97.91	18.59	49.72	31.69
8	200	0.40	64.1	67.5294	0.0	97.93	18.46	49.65	31.89
9	225	0.45	74.4	78.3804	0.0	97.95	18.5	49.56	31.94
10	250	0.50	84.9	89.4422	0.0	97.96	18.47	49.55	31.98
11	275	0.55	95.8	100.9253	0.0	97.96	18.53	49.65	31.82
12	300	0.60	106.8	112.5138	0.0	97.97	18.54	49.61	31.85
13	325	0.65	118.0	124.3130	0.0	97.97	18.52	49.71	31.77
14	350	0.70	128.9	135.7962	0.0	97.98	18.64	49.45	31.91
15	375	0.75	139.8	147.2793	0.0	97.98	18.61	49.48	31.91
16	400	0.80	151.1	159.1839	0.0	97.96	18.75	49.62	31.63
17	425	0.85	162.2	170.8777	0.0	97.94	18.69	49.59	31.72
18	450	0.90	173.6	182.8876	0.0	97.93	18.67	49.61	31.72
BT	469	0.94	182.7	192.4745	0.0	97.91	18.71	49.50	31.79
19	475	0.95	185.1	195.0029	0.0	97.90	18.48	49.97	31.55
20	500	1.00	196.8	207.3288	0.0	97.89	18.49	49.51	32.00
21	525	1.05	208.2	219.3387	280.5	97.87	18.27	50.33	31.4
22	550	1.10	220.0	231.7700	2330.6	97.88	17.33	51.51	31.16
23	575	1.15	235.7	248.3100	8783.1	97.91	15.11	53.98	30.91
24	600	1.20	246.7	259.8985	15343.4	97.93	10.14	57.27	32.59

Table A.5: Slim tube data at $p = 3930\,psi$

#	**Time (min)**	$\mathbf{V_{injected}}$ **(PV)**	$\mathbf{V_{oil}}$ **SC (cc)**	$\mathbf{V_{oil}}$ **RC (cc)**	$\mathbf{V_{gas}}$ **SC (cc)**	**Temp (°C)**	$\mathbf{C_6}$ **(%)**	$\mathbf{C_{10}}$ **(%)**	$\mathbf{C_{16}}$ **(%)**
0	0	0.00	0.0	0.0000	0.0	98.02	0.00	0.00	0.00
1	25	0.05	3.8	3.9889	0.0	97.94	18.57	49.51	31.92
2	50	0.10	9.6	10.0771	0.0	97.94	18.82	49.70	31.49
3	75	0.15	16.7	17.5300	0.0	97.95	18.81	49.66	31.53
4	100	0.20	26.0	27.2922	0.0	97.96	18.61	49.63	31.77
5	125	0.25	36.8	38.6290	0.0	97.97	18.47	49.55	31.98
6	150	0.30	48.6	50.9629	0.0	97.98	18.60	49.70	31.69
7	175	0.35	61.0	64.0317	0.0	97.98	18.51	49.83	31.66
8	200	0.40	74.5	78.2027	0.0	97.99	18.81	49.60	31.59
9	225	0.45	88.0	92.3736	0.0	98.00	18.83	49.55	31.61
10	250	0.50	101.6	106.5970	0.0	98.00	18.62	49.68	31.70
11	275	0.55	115.1	120.8205	0.0	98.00	18.47	49.79	31.74
12	300	0.60	128.8	135.1489	0.0	98.01	18.53	49.66	31.81
13	325	0.65	142.3	149.3198	0.0	98.00	18.54	49.81	31.65
14	350	0.70	156.0	163.7532	0.0	97.99	18.41	49.79	31.80
15	375	0.75	169.7	178.1341	0.0	97.97	18.87	49.48	31.65
16	400	0.80	183.3	192.3575	0.0	97.96	18.64	49.69	31.67
17	425	0.85	196.8	206.5810	0.0	97.94	18.58	49.57	31.84
18	450	0.90	210.3	220.7519	0.0	97.93	18.82	49.51	31.67
19	475	0.95	223.9	235.0278	0.0	97.91	18.50	49.77	31.73
20	500	1.00	237.6	249.4087	0.0	97.90	18.64	49.37	32.00
21	525	1.05	251.4	263.8946	153.4	97.90	18.78	49.69	31.53
22	550	1.10	266.7	279.9025	1865.8	97.89	16.71	51.79	31.50
23	575	1.15	278.7	292.5514	4114.9	97.88	12.03	55.64	32.33
24	600	1.20	281.9	295.9104	14312.1	97.86	9.37	57.97	32.66

Table A.6: Slim tube data at $p = 4600\,psi$

#	**Time (min)**	$\mathbf{V_{injected}}$ **(PV)**	$\mathbf{V_{oil}}$ **SC (cc)**	$\mathbf{V_{oil}}$ **RC (cc)**	$\mathbf{V_{gas}}$ **SC (cc)**	**Temp (°C)**	$\mathbf{C_6}$ **(%)**	$\mathbf{C_{10}}$ **(%)**	$\mathbf{C_{16}}$ **(%)**
0	0	0.00	0.0	0.0000	0.0	98.03	0.00	0.00	0.00
1	25	0.05	2.7	2.7698	0.0	98.00	18.54	49.75	31.71
2	50	0.10	8.3	8.6752	0.0	98.01	18.56	49.44	31.99
3	75	0.15	16.8	17.5594	0.0	98.00	18.54	49.89	31.57
4	100	0.20	27.5	28.7430	0.0	98.00	18.75	49.74	31.51
5	125	0.25	38.8	40.5538	0.0	97.99	18.56	49.63	31.81
6	150	0.30	51.6	53.9323	0.0	97.99	18.58	49.57	31.85
7	175	0.35	64.8	67.7290	0.0	97.98	18.43	49.62	31.96
8	200	0.40	78.2	81.7346	0.0	97.98	18.48	49.69	31.83
9	225	0.45	91.8	95.9494	0.0	97.97	18.85	49.76	31.39
10	250	0.50	105.6	110.3731	0.0	97.96	18.76	49.81	31.43
11	275	0.55	118.9	124.2743	0.0	97.95	18.49	49.62	31.89
12	300	0.60	132.3	138.2800	0.0	97.94	18.70	49.59	31.71
13	325	0.65	145.7	152.2856	0.0	97.94	18.83	49.71	31.46
14	350	0.70	159.2	166.3958	0.0	97.95	18.68	49.42	31.90
15	375	0.75	172.6	180.4015	0.0	97.96	18.58	49.83	31.59
16	400	0.80	186.2	194.6162	0.0	97.97	18.54	49.84	31.62
17	425	0.85	199.8	208.8310	0.0	97.98	18.46	49.68	31.86
18	450	0.90	213.5	223.1502	0.0	97.98	18.69	49.51	31.81
19	475	0.95	227.2	237.4694	0.0	97.99	18.39	49.80	31.81
20	500	1.00	240.9	251.7887	0.0	97.99	18.46	49.77	31.77
21	525	1.05	254.9	266.4215	261.3	97.98	18.60	49.71	31.69
22	550	1.10	271.8	284.0331	2351.5	97.97	16.35	51.50	32.15
23	575	1.15	281.4	294.0670	8651.0	97.96	11.82	54.62	33.56
24	600	1.20	288.5	301.4879	10509.7	97.94	9.37	56.78	33.85

Appendix B

Constant Pressure Boundaries Experiments

B.1 Case Study 4

Sample calculation of total velocity between at 400 minutes: first, the gas volume at reservoir condition is calculated using real gas law, i.e.

$$P_R V_{g,R} = Z_R R T_R, \quad P_{SC} V_{g,SC} = R T_{SC} \Rightarrow V_{g,R} = \frac{Z_R T_R}{T_{SC}} \frac{P_{SC} V_{g,SC}}{P_R} = 17.0795\, cc \tag{B.1}$$

The the gas velocity is calculated as,

$$u_g = \frac{q_{g,R}}{A} = \frac{V_{g,R}}{At} = 9.3576 \times 10^{-4} m/s \tag{B.2}$$

Oil volume is then calculated at the reservoir condition,

$$V_{o,R} = V_{o,SC} \times 1.0755 = 0.9 \times 10^{-4} m^3 \times 1.0755 = 0.9680\, m^3 \tag{B.3}$$

The oil velocity is

$$u_o = \frac{V_{o,R}}{At} = 0.5303 \times 10^{-4} \frac{m}{s} \tag{B.4}$$

Finally, the total velocity is calculated as,

$$u_t = u_g + u_o = 9.8879 \times 10^{-4} \frac{m}{s} \tag{B.5}$$

Table B.1: Constant pressure boundary experimental data at $\mathbf{p = 531.9\,psi}$

#	**Time (min)**	$\mathbf{V_{oil}}$ **SC (cc)**	$\mathbf{V_{gas}}$ **SC (cc)**	**DMA** ($\mathbf{Kg/m^3}$)	**Temp** (^oC)	$\mathbf{C_6}$ (%)	$\mathbf{C_{10}}$ (%)	$\mathbf{C_{16}}$ (%)
0	0	0.0	0.0	1323.41	98.04	0.00	0.00	0.00
1	10	2.3	0.0	1323.41	98.01	18.52	49.51	31.97
2	20	2.9	0.0	1323.41	97.99	18.85	49.72	31.43
3	30	3.0	0.0	1323.41	97.99	18.82	49.88	31.30
4	40	3.1	0.0	1323.41	98.00	18.79	49.45	31.76
5	50	3.1	0.0	1323.41	98.00	18.56	49.49	31.95
6	60	3.3	0.0	1323.41	98.00	18.63	49.55	31.82
7	70	3.2	0.0	1323.41	98.01	18.66	49.64	31.69
8	80	3.4	0.0	1323.41	98.01	18.80	49.78	31.42
9	90	3.6	0.0	1323.42	98.01	18.85	49.77	31.38
10	100	3.5	0.0	1323.42	98.02	18.82	49.61	31.57
11	110	3.6	0.0	1323.42	98.02	18.36	49.51	32.13
12	120	3.7	0.0	1323.43	98.02	18.44	49.86	31.70
13	130	3.8	0.0	1323.44	98.03	18.64	49.47	31.89
14	140	3.8	0.0	1323.44	98.03	18.59	49.56	31.85
15	150	4.0	0.0	1323.46	98.03	18.61	49.74	31.64
16	160	4.1	0.0	1323.47	98.04	18.72	49.69	31.59
17	170	4.2	0.0	1323.5	98.04	18.67	49.80	31.53
18	180	4.3	0.0	1323.55	98.04	18.70	49.40	31.90
19	190	4.5	0.0	1323.61	98.03	18.62	49.55	31.83
20	200	4.8	0.0	1323.67	98.02	18.78	49.84	31.38
21	210	5.1	0.0	1323.78	98.01	18.83	49.90	31.27
22	220	5.7	0.0	1323.89	98.00	18.64	49.78	31.57
23	230	6.4	0.0	1323.96	97.99	18.51	49.46	32.03
24	240	7.5	0.0	1324.06	97.97	18.79	49.74	31.47

Table B.2: Constant pressure boundary experimental data at $\mathbf{p = 531.9\,psi}$ (Continued from Table B.1

#	Time (min)	V_{oil} SC (cc)	V_{gas} SC (cc)	DMA (Kg/m^3)	Temp (°C)	C_6 (%)	C_{10} (%)	C_{16} (%)
BT	253	10.1	0	1324.19	97.96	18.56	49.42	32.02
26	260	5.8	0	1324.31	97.94	18.83	49.82	31.34
27	270	7.9	0	1324.42	97.95	18.85	49.87	31.28
28	280	8.2	0	1324.5	97.95	18.56	49.55	31.89
29	290	2.3	196.7	1031.24	97.94	18.55	49.62	31.82
30	300	1.8	224.5	954.03	97.93	18.60	49.75	31.66
31	310	1.5	213.1	922.35	97.91	18.81	49.48	31.72
32	320	1.4	262.3	911.46	97.89	18.70	49.82	31.48
33	330	1.3	374.1	976.84	97.88	18.45	49.80	31.75
34	340	1.1	301.2	990.64	97.86	18.57	49.40	32.03
35	350	0.8	361.3	954.37	97.83	18.73	49.74	31.53
36	360	1.1	404.7	978.14	97.81	18.64	49.83	31.53
37	370	1.4	446.8	946.89	97.8	18.37	49.62	32.02
38	380	1.4	430.2	954.71	97.81	18.45	49.50	32.05
39	390	1.3	451.2	933.81	97.81	18.35	49.81	31.84
40	400	0.9	523.3	899.47	97.82	18.36	49.80	31.84
41	420	2.1	1086.7	869.13	97.83	17.83	50.64	31.53
42	440	1.9	1007.8	895.71	97.83	17.56	50.39	32.05
43	460	1.6	1245.8	801.87	97.84	17.05	50.88	32.07
44	480	1.5	1231.4	809.62	97.85	16.97	50.67	32.36
45	510	1.8	2041.9	787.12	97.84	16.51	51.84	31.65
46	535	1.7	1537.9	794.55	97.84	16.73	51.93	31.34
47	610	3.4	5904.3	755.67	97.84	13.62	54.68	31.70
48	820	6.3	19083	769.18	97.83	8.46	57.48	34.06

B.2 Case Study 5

Table B.3: Constant pressure boundary experimental data at $\mathbf{p = 934.5\,psi}$

#	Time (min)	V_{oil} SC (cc)	V_{gas} SC(cc)	DMA (Kg/m^3)	Temp (°C)	C_6 (%)	C_{10} (%)	C_{16} (%)
0	0	0.0	0.0	1325.01	98.05	0.00	0.00	0.00
1	10	2.4	0.0	1325.01	98.03	18.82	49.67	31.50
2	20	2.7	0.0	1325.01	98.03	18.37	49.55	32.08
3	30	2.9	0.0	1325.01	98.03	18.62	49.69	31.69
4	40	3.0	0.0	1325.00	98.04	18.38	49.52	32.10
5	50	3.1	0.0	1325.01	98.04	18.49	49.48	32.03
6	60	3.2	0.0	1325.01	98.03	18.38	49.66	31.97
7	70	3.4	0.0	1325.02	98.03	18.77	49.46	31.77
8	80	3.3	0.0	1325.02	98.02	18.66	49.67	31.67
9	90	3.4	0.0	1325.02	98.01	18.43	49.55	32.02
10	100	3.5	0.0	1325.03	98.01	18.77	49.59	31.64
11	110	3.6	0.0	1325.03	98.01	18.62	49.42	31.96
12	120	3.6	0.0	1325.03	98.00	18.54	49.49	31.96
13	130	3.7	0.0	1325.03	98.00	18.76	49.80	31.44
14	140	3.7	0.0	1325.03	97.99	18.40	49.69	31.91
15	150	3.9	0.0	1325.03	97.99	18.51	49.46	32.03
16	160	3.8	0.0	1325.04	97.98	18.48	49.48	32.05
17	170	3.9	0.0	1325.04	97.98	18.40	49.74	31.86
18	180	4.0	0.0	1325.05	97.97	18.46	49.70	31.83
19	190	4.1	0.0	1325.06	97.96	18.39	49.84	31.77
20	200	4.2	0.0	1325.08	97.96	18.62	49.86	31.52
21	210	4.3	0.0	1325.09	97.95	18.67	49.88	31.45
22	220	4.5	0.0	1325.10	97.94	18.53	49.80	31.66
23	230	4.6	0.0	1325.13	97.92	18.76	49.73	31.51
24	240	5.0	0.0	1325.15	97.91	18.56	49.60	31.84

Table B.4: Constant pressure boundary experimental data at $\mathbf{p = 934.5\,psi}$ (Continued from Table B.3

#	**Time (min)**	$\mathbf{V_{oil}}$ **SC (cc)**	$\mathbf{V_{gas}}$ **SC(cc)**	**DMA** ($\mathbf{Kg/m^3}$)	**Temp** (^oC)	$\mathbf{C_6}$ (%)	$\mathbf{C_{10}}$ (%)	$\mathbf{C_{16}}$ (%)
25	250	5.4	0.0	1325.19	97.89	18.38	49.73	31.89
26	260	6.1	0.0	1325.23	97.89	18.62	49.57	31.81
27	270	6.9	0.0	1325.29	97.88	18.55	49.84	31.61
28	280	7.3	0.0	1325.34	97.88	18.40	49.85	31.75
BT	292	8.8	0.0	1325.40	97.88	18.80	49.50	31.70
30	300	6.2	0.0	1325.49	97.88	18.36	49.44	32.20
31	310	7.9	0.0	1325.61	97.88	18.70	49.64	31.66
32	320	8.0	0.0	1325.67	97.87	18.49	49.49	32.02
33	330	1.9	290.6	1101.35	97.87	18.71	49.46	31.83
34	340	1.6	381.2	1067.12	97.87	18.63	49.61	31.76
35	350	1.7	372.2	987.84	97.86	18.62	49.44	31.94
36	360	1.5	405.4	941.05	97.86	18.38	49.73	31.89
37	370	1.6	467.9	966.68	97.86	18.75	49.48	31.77
38	380	1.4	552.3	948.71	97.87	18.62	49.46	31.92
39	390	1.5	501.0	931.46	97.87	18.59	49.75	31.67
40	400	1.3	596.0	900.24	97.88	18.80	49.80	31.40
41	420	2.1	1199.1	932.17	97.88	17.75	50.46	31.79
42	440	2.9	1543.2	957.79	97.88	17.41	50.87	31.72
43	460	1.2	1364.0	922.09	97.88	17.23	50.93	31.84
44	480	1.2	1606.1	898.63	97.89	17.06	50.49	32.45
45	510	1.9	2908.9	862.15	97.89	16.42	51.49	32.09
46	535	1.7	2160.8	837.18	97.90	16.65	52.13	31.22
47	560	1.3	2789.3	805.51	97.91	15.11	55.06	29.83
48	760	5.5	29827.5	802.13	97.91	7.88	58.79	33.33